RSC Advances

REVIEW

View Article Online
View Journal | View Issue

Cite this: *RSC Adv.*, 2026, **16**, 28048

Synthesis and advanced applications of MXene nanosheets in energy storage, EMI shielding, and biomedicine: a review

Mohamed Mohamady Ghobashy, *[a] Muneer Baata,[b] Mohammed S. Almoiqli,[b] Mohamed Azlzul Haque,[c] Faisal K. Algethami, *[d] Ahmed Siddiq[e] and Mohamed S. Attia[d]

MXenes, a rapidly expanding family of two-dimensional (2D) transition-metal carbides, nitrides, and carbonitrides, have attracted significant attention for their unique properties, including metallic conductivity, hydrophilicity, and tunable surface chemistry. This review comprehensively examines the synthesis methods of MXenes, focusing on selective etching techniques, such as hydrofluoric acid (HF) etching, and safer alternatives, including *in situ* HF generation and molten salt etching. The structure–property relationships of MXenes are explored, highlighting their exceptional electrical conductivity, mechanical strength, and surface chemistry, all of which are pivotal to their performance in various applications. Key applications discussed include energy storage (supercapacitors and batteries), where MXenes exhibit high capacitance and efficient ion intercalation; electromagnetic interference (EMI) shielding, leveraging their conductivity and layered structure for superior attenuation; and biomedical uses, such as drug delivery and biosensing, enabled by their biocompatibility and functionalization potential. Despite their promise, challenges such as environmental stability and scalable synthesis persist, necessitating further research to fully realize their potential in next-generation technologies. This review consolidates current knowledge, identifies critical challenges, and outlines future directions for MXene research and applications.

Received 26th March 2026
Accepted 8th May 2026

DOI: 10.1039/d6ra02525k

rsc.li/rsc-advances

1. Introduction

MXenes are a rapidly emerging family of two-dimensional (2D) materials composed of transition-metal carbides, nitrides, or carbonitrides, generally described by the formula $M_{n+1}X_nT_x$. The term "MXene" is derived from the combination of M, denoting an early transition metal, X, representing carbon and/or nitrogen, and the suffix "-ene," highlighting their graphene-like layered morphology. This formulation provides a concise framework for understanding the composition and structural diversity of MXenes.[1–3]

In this general formula, M corresponds to transition metals such as Ti, V, Cr, Mo, Nb, or Ta. At the same time, X denotes carbon or nitrogen atoms occupying interstitial sites within the metal layers. The parameter n (typically 1–4) determines the number of layers sandwiched between the metal layers and, consequently, the thickness and structural configuration of the MXene sheets. Variations in n lead to distinct stacking arrangements inherited from their parent MAX phases, giving rise to well-defined layered architectures.[4,5]

A defining feature of MXenes is the presence of surface terminations, represented by T_x, which are introduced during the selective etching of the precursor MAX phases. These terminal groups commonly include –O, –OH, –F, and –Cl, and are bonded to the outermost transition-metal layers. Although often unavoidable, these surface terminations play a central role in governing MXene properties by modulating surface chemistry, hydrophilicity, electronic structure, interlayer spacing, and mechanical behavior.[3,6]

Structurally, MXenes consist of close-packed transition-metal layers interleaved with carbon or nitrogen atoms, forming a lamellar, sandwich-like configuration. The compositional flexibility at the M site, combined with tunable surface terminations, enables precise tailoring of MXene properties, making them highly versatile materials for applications spanning energy storage, catalysis, sensing, environmental remediation, and advanced composites.[3,4,7]

Fig. 1a illustrates the chemical composition of MAX phases and the fundamental processes involved in the synthesis of

[a]*Radiation Research of Polymer Department, National Center for Radiation Research and Technology (NCRRT), Atomic Energy Authority, P.O. Box. 29, Nasr City, Cairo, Egypt. E-mail: ghobashy_ghobashy@yahoo.com; Mohamed.ghobashy@eaea.org.eg*

[b]*Desalination Technologies Institute (DTI), King Abdulaziz City for Science and Technology, Riyadh, 11442, Saudi Arabia*

[c]*Biotechnology Department, University of Yeungnam, Gyoengbuk, Republic of Korea*

[d]*Chemistry Department, College of Science, Imam Mohammad Ibn Saud Islamic University (IMSIU), Riyadh 11623, Saudi Arabia. E-mail: falgethami@imamu.edu.sa*

[e]*Department of Chemistry, Faculty of Science, Al-Azhar University, Assiut, 71524, Egypt*

MXenes. The figure presents a periodic table arrangement showing the elemental components that form MAX phases, where M represents early transition metals (such as Ti, V, Cr, Nb, Ta, W, *etc.*), A represents A-group elements (primarily Al, but also Si, Ge, As, P, S, Sn, In, Ga, *etc.*), and X represents carbon or nitrogen. The visual representation illustrates how these elements combine to form precursor MAX phases, which are subsequently etched to remove the A-layer atoms, thereby forming multilayer MXenes. The peeling process further transforms these multilayer structures into monolayer MXenes, creating 2D materials with unique properties and surface terminations (T_x, where T represents –O, –F, and –OH functional groups).

Fig. 1b illustrates the steps involved in treating the MAX phase with hydrofluoric acid (HF). This process, known as selective etching, involves chemically removing the A-layers (typically aluminum). The figure illustrates this by showing the initial compact stacked layers being separated by the introduction of spherical atoms representing the A-layer, which are then removed by the HF treatment. The reaction between HF and the A-layer forms soluble fluoride salts (*e.g.*, AlF_3), which are washed away, leaving behind layers of transition-metal carbides (MXenes) terminated with surface groups such as –OH, –O, and –F. These surface terminations are crucial for tuning the physical and chemical properties of the resulting MXenes.

Following etching, the remaining structure consists of loosely stacked MXene sheets, held together primarily by van der Waals forces. To achieve delamination into individual 2D sheets, sonication is applied. Sonication uses high-frequency ultrasonic energy to physically separate stacked layers. This step effectively transforms the loosely packed structure into discrete, thin, flexible MXene nanosheets, as depicted by the wavy, separated sheets in the figure. These nanosheets possess high surface area, excellent electrical conductivity, and hydrophilic properties due to their surface terminations. Fig. 1c presents a scanning electron microscopy (SEM) image of $Ti_3C_2T_x$ MXene synthesized *via* HF etching, showing the characteristic accordion-like morphology resulting from the selective removal of aluminum layers from the Ti_3AlC_2 MAX phase precursor. The image reveals the layered structure, accompanied by a 5 μm scale bar, demonstrating the successful exfoliation process in which the original compact MAX phase structure has been transformed into expanded, sheet-like layers. The characteristic accordion-like morphology arises from the fluorine-based etching process. During this reaction,

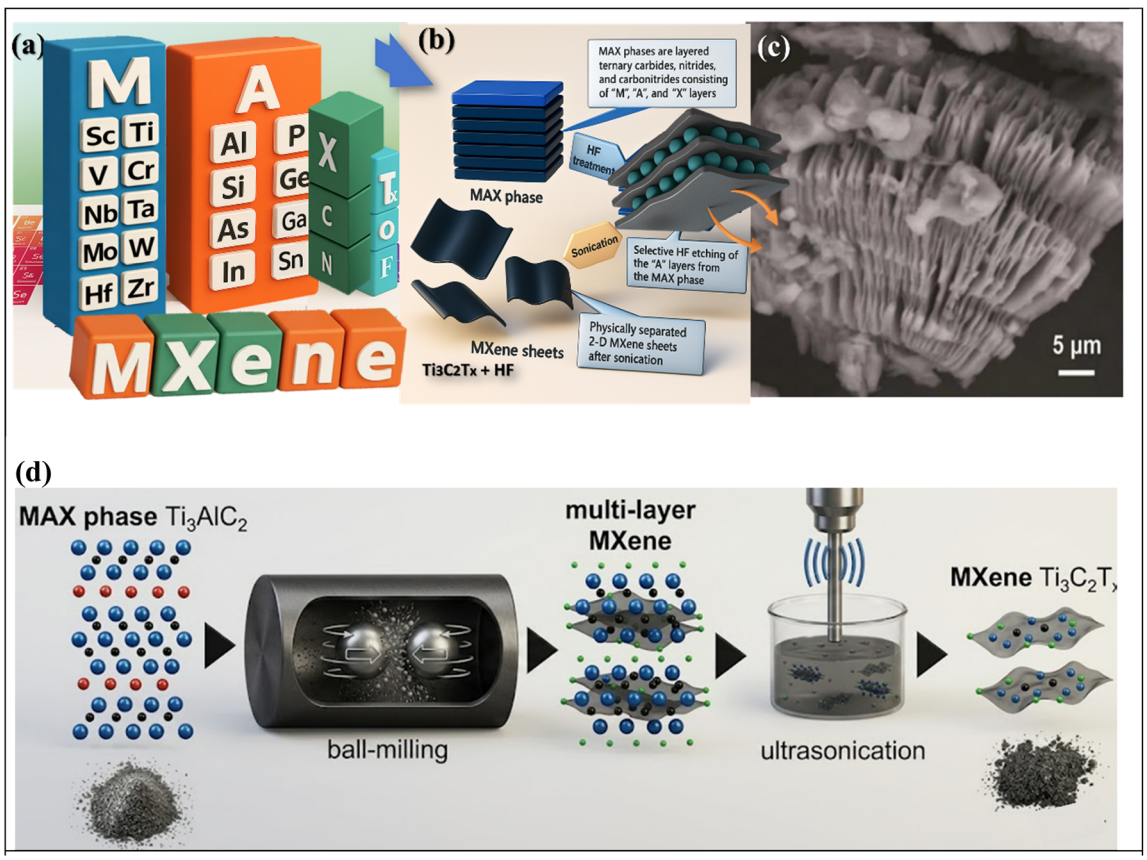

Fig. 1 MXene synthesis from MAX phases: (a) chemical composition showing M, A, and X elements and transformation pathway from MAX phases to monolayer MXenes, (b) HF etching process with selective A-layer removal and sonication-induced delamination, and (c) SEM image of $Ti_3C_2T_x$ MXene displaying characteristic accordion-like morphology after HF etching (scale bar: 5 μm), this figure has been reproduced from ref. 8 with permission from Taylor and Francis, copyright 2023. (d) Physically assisted synthesis of MXenes, which combines mechanical and ultrasonic methods to produce few-layered or delaminated MXene nanosheets. This figure has been reproduced from ref. 9 with permission from Taylor and Francis, copyright 2023.

fluorine species bond to the A-layer atoms, aluminum in this case, facilitating their removal. Simultaneously, hydrogen gas is generated, promoting expansion and delamination of the remaining Ti_3C_2 layers. Since the earliest room-temperature fluoride etching protocols, MXene synthesis has advanced considerably. Although direct acid etching remains the most practical and widely adopted method for producing MXenes, concerns regarding safety and environmental impact have driven the development of alternative strategies. These include *in situ* generation of fluoride species *via* reactions between HCl and LiF, alkali-based treatments, electrochemical approaches, molten-salt etching, and mechanochemical ball-milling. The development of these green synthesis methods represents a crucial advancement in making MXene synthesis more accessible and environmentally sustainable for large-scale applications.

Fig. 1d illustrates the physically assisted synthesis of MXenes, which combines mechanical and ultrasonic methods to produce few-layered or delaminated MXene nanosheets. In this approach, the MAX phase precursor (*e.g.*, Ti_3AlC_2) is first subjected to mechanical ball milling, which applies strong shear and compressive forces to reduce particle size, induce defects, and weaken interlayer bonds. This facilitates subsequent exfoliation of the layered structure. Following milling, the partially delaminated material undergoes ultrasonic treatment in a suitable solvent (*e.g.*, acetone, ethanol, or HCl solution), where ultrasonic waves generate cavitation and high-energy microjets that further separate individual MXene layers. This method enables the production of MXenes with increased surface area, tunable interlayer spacing, and functional terminations (–OH, –O, –F depending on treatment), while avoiding toxic chemicals commonly used in conventional etching. Compared to purely chemical methods, this physically assisted synthesis produces high-quality MXenes for diverse applications.

The quality of MXene materials depends critically on several process parameters, including the concentration of the etching agent, reaction time, and temperature. For MAX phases with large "*n*" values, higher concentrations of hydrofluoric acid are typically required for effective etching. In comparison, MAX phases with lower "*n*" values require lower HF concentrations to prevent over-etching and dissolution of the generated MXene. The correlation between etching conditions and the resulting MXene structure has been studied extensively, revealing that while HF interacts with the MAX phase, aluminum atoms at the edges of the middle layers do not participate in the etching process, leading to selective removal mechanisms that preserve the integrity of the remaining carbide layers. The future development of MXene synthesis is increasingly focused on safer, more efficient preparation methods that eliminate the use of hazardous chemicals while maintaining the quality and properties of the resulting materials. The transition from traditional HF-based methods to fluorine-free approaches represents a significant shift in the field, driven by both safety considerations and the need for scalable production methods. These developments in synthesis methodology are expected to facilitate broader applications of MXene-based materials in catalysis, energy storage, and other advanced technological applications.

This review is more original because it focuses on MXene-hydrogel hybrids and uses that lens to connect materials design, mechanical flexibility, and signal transduction for biosensing and environmental surveillance, rather than offering another broad overview of MXenes as a whole. Framed this way, the manuscript complements the existing review literature by filling a narrower but practically useful gap in application-specific hybrid design.

The scope of this review extends beyond mere synthesis and characterization to encompass the structure–property relationships that govern MXene behavior, their integration into composite materials, and their performance in various applications. Special attention is given to the most promising applications of MXenes, including energy storage devices, electromagnetic interference (EMI) shielding, water purification, and biomedical applications. It also addresses the critical challenges facing the field, such as oxidation stability, scalability of synthesis methods, and environmental considerations.

Furthermore, it provides a forward-looking perspective on the future of MXene research, identifying emerging trends and potential breakthrough applications. The multidisciplinary nature of MXene research, which spans materials science, chemistry, physics, and engineering, necessitates a comprehensive approach that bridges these disciplines. By synthesizing current knowledge and identifying research gaps, this review aims to inspire future investigations and accelerate the translation of MXene research from laboratory discoveries to real-world applications.

2. Synthesis methods and processing techniques of MXene nanosheets

The synthesis of MXene nanosheets is a crucial step in advancing and applying these extraordinary 2D materials. The transformation from MAX phases to MXenes involves removing the A-layer *via* selective etching, followed by a series of post-processing steps to produce delaminated or few-layer nanosheets. This synthesis process determines the structural, chemical, and electrochemical properties of the final MXene material, directly influencing its performance in applications ranging from energy storage and water purification to biosensing and EMI shielding.

The first and most fundamental step in synthesizing MXene nanosheets is the selective etching of the A-element from the MAX phase. This step relies on the differential reactivity of the A-layer, which is more chemically active than the M-X bonds. The most commonly used etchant is HF, which selectively reacts with elements such as aluminum to produce multilayered MXene structures, such as $Ti_3C_2T_x$, where T_x denotes surface terminations like –OH, –F, and –O.[10]

- *In situ* HF generation: a safer alternative where fluoride salts like LiF or NaF are mixed with HCl to generate HF *in situ.* This method reduces the direct handling of HF and improves the control over the etching reaction. It is widely adopted in lab-scale synthesis, enabling better preservation of MXene layer structural integrity.

• Molten salt etching: in this approach, Lewis-acidic molten salts, such as $ZnCl_2$, are used to extract the A-layer. This method can produce MXenes with different surface terminations, such as Cl, and has the potential to avoid the –F termination entirely. It also enables etching of more resistant MAX phases that are difficult to treat using aqueous etchants.

• Electrochemical etching: a relatively recent, green alternative, it uses an electrochemical cell in which MAX serves as the anode in a fluoride-containing electrolyte. The etching process uses anodic oxidation, providing precise control and often yielding MXenes with fewer defects and a high degree of delamination.

Each of these etching methods yields multilayered MXenes with characteristic accordion-like morphologies. The degree of etching and the resulting surface chemistry are strongly dependent on factors such as reaction time, temperature, acid concentration, and the type of MAX phase used.

Following the etching step, the resultant multilayered MXene powders must undergo delamination or exfoliation to produce single- or few-layer nanosheets. This step is crucial because many of the desirable properties of MXenes such as their high surface area, tunable surface chemistry, and superior charge transport are most pronounced in the delaminated state. Delamination is typically achieved by intercalating organic molecules or cations between the layers to weaken the van der Waals forces holding them together. Common intercalants include:

• Organic intercalants such as dimethyl sulfoxide (DMSO), isopropanol, or tetrabutylammonium hydroxide (TBAOH) can penetrate the interlayer space and facilitate exfoliation upon mild agitation or sonication.

• Cationic intercalation with metal ions (*e.g.*, Li^+, K^+, Na^+) also allows for delamination, particularly when followed by gentle sonication or mechanical stirring in aqueous or organic media.

• Mechanical delamination techniques, such as high-speed shearing, microfluidic exfoliation, and ball milling, have also been explored to produce larger quantities of delaminated MXenes; however, these methods may introduce structural defects if not properly controlled.

Once exfoliated, MXene nanosheets are typically collected as stable colloidal suspensions in polar solvents, such as water. These suspensions can be easily processed into films, coatings, or inks for various applications. The stability and concentration of MXene colloids depend on parameters like pH, surface charge (zeta potential), and ionic strength of the medium.

The synthesis route chosen for MXene fabrication significantly impacts the final material properties. Surface terminations, as mentioned earlier, are directly influenced by the chemical environment during etching. For example, HF-based etching typically yields –F- and –OH-terminated MXenes, whereas molten-salt methods can yield Cl-terminated surfaces.

Moreover, synthesis parameters such as etching time and temperature affect the crystallinity and lateral size of the nanosheets. Excessive etching can lead to layer degradation and defect formation, while insufficient etching can result in incomplete removal of the A-layer, producing impure MXene products. The choice of intercalants and exfoliation techniques also plays a vital role. Aggressive sonication may reduce flake size and introduce oxygen-containing defects, while milder methods may preserve large flake areas but yield lower exfoliation degrees. Therefore, a careful balance must be struck to optimize MXene quality for specific applications. Recent research has focused on extending MXene synthesis beyond traditional Ti-based systems to include a wide array of M elements, including Nb, Mo, V, Cr, and Ta. However, not all MAX phases can be readily converted into MXenes due to factors such as insufficient chemical reactivity or structural instability. Efforts are also underway to develop fluorine-free and environmentally benign etching processes. For example, alkali treatment and molten hydroxide methods are being explored to eliminate the need for fluoride-containing reagents. Additionally, scalable, cost-effective synthesis methods remain a central objective for enabling future industrial-scale MXene production. Continuous flow synthesis, roll-to-roll exfoliation, and spray-assisted exfoliation are among the promising strategies being developed for commercial applications.

3. Selective etching approaches HF

Selective etching is the most widely used approach for MXene synthesis, involving the removal of A-layer atoms from MAX phases using various chemical etchants. The etching process is based on the principle that the M–A bonds in MAX phases are weaker than the M–X bonds, allowing for selective removal of the A-layer while preserving the MXene structure.[11,12] The choice of etching agent and conditions significantly impacts the resulting MXene properties, including surface terminations, morphology, and defect density.

The original and most widely adopted etching method uses concentrated HF as the etchant.[13] This method was first reported by Naguib *et al.*[11] for the synthesis of $Ti_3C_2T_x$ from Ti_3AlC_2 MAX phase. The HF etching process typically involves immersing the MAX phase powder in concentrated HF solution (typically 40–50 wt%) at room temperature for 24–72 hours.[3] The HF etching method produces MXenes with characteristic accordion-like morphology and mixed surface terminations of –OH, –O, and –F.[14] The technique is highly effective for producing high-quality MXenes with good crystallinity and minimal defects.

In contrast, HF etching gives different MXene surface terminations because the chemistry at the etching interface is very sensitive to proton activity, fluoride speciation, and the availability of oxygen/water and metal sites. In practice, these factors control the relative formation of –F, –OH, and –O groups on the exposed M (*e.g.*, Ti, Nb) surface, as outlined below.

3.1. Role of pH

At very low pH, the solution is strongly acidic, with high HF/H^+ activity and significant free F–; this favors strong M–F bonding, so more –F terminations form on the MXene surface.[15]

As pH increases (still acidic but less extreme), HF is partially dissociated, hydrolysis of surface M–F is easier, and water

competes more effectively, leading to more –OH and –O terminations *via* substitution of F^- by OH^-/O.[2–16]

Very low pH also suppresses deprotonation of surface –OH to $–O^-$, while mildly acidic/near-neutral post-treatments can convert –OH to –O, further shifting the termination distribution.[17,18]

3.2. Role of water content[19]

Water plays a critical role in determining the surface chemistry and etching dynamics of MXenes. As the primary oxygen source, it facilitates the formation of –OH and –O terminations: higher water content promotes hydrolysis of surface M–F bonds, leading to increased coverage by hydroxyl and oxide groups.[20,21] In contrast, in more concentrated or less aqueous fluoride environments (*e.g.*, high HF with added organic co-solvents), hydrolysis is suppressed. Under these conditions, –F terminations dominate, while oxo/hydroxo groups are less prevalent.[21]

Water content also affects the dissolution rate of A-layer elements (*e.g.*, Al). Faster etching, driven by higher water availability, can generate additional defects and reactive sites. These sites are rapidly passivated by the most abundant species in the system, often fluoride ions in concentrated etchants, thereby influencing the final surface termination pattern.[20,22]

Interestingly, these water-dependent processes share conceptual similarities with sol–gel methodologies, which rely on hydrolysis and condensation reactions to form gels or hydrogels.[20–22] In both cases, water mediates the conversion of precursor bonds (M–F in MXenes, metal alkoxides in sol-gels) into oxygen-containing species (–OH/–O terminations or hydroxylated networks). A key difference is that sol–gel processes are typically controlled to promote network formation and gelation. In contrast, MXene etching involves the selective dissolution of the A-layer, generating 2D layers rather than a bulk gel. Despite these differences, considering the hydrolysis-driven transformations highlights parallels in how water governs the chemical evolution of both systems.

In addition, further parameters controlled the MXene surface terminations, such as Variations in precursor stoichiometry and MAX-phase chemistry play a decisive role in determining MXene surface terminations because the exact M/A/X ratio such as stoichiometric Ti_3AlC_2 *versus* non-stoichiometric or doped MAX phases, modifies local bonding strength and the ease with which the A layer is removed, thereby altering the kinetics of surface exposure and termination formation. Non-stoichiometric or doped MAX structures can release different amounts of metal cations and Al^{3+} during etching, shifting local pH and influencing fluoride complexation (*e.g.*, the formation of $[AlF_6]^{3-}$), which, in turn, changes the balance between direct F termination and hydrolysis-driven formation of –OH/–O groups. Furthermore, the identity of the transition metal (Ti, Nb, V, Mo) strongly affects termination chemistry because each metal exhibits different relative affinities for F^- *versus* O^{2-}/OH^-, meaning that even under identical macroscopic HF conditions, the preferred termination distribution depends on the precursor composition. Fluoride speciation further modulates termination outcomes: in concentrated HF, most fluoride exists as HF and polyfluoride species (*e.g.*, HF_2^-) that strongly coordinate to metal sites and stabilize –F terminations, whereas in dilute HF or *in situ* HF systems generated from fluoride salts and weak acids, the effective free F^- concentration is lower and more Al–F complexes form in solution, leaving water and oxygen to dominate passivation and thereby increasing –OH/–O surface coverage. Additionally, the complexation of dissolved metal ions by fluoride and changes in ionic strength influence the local electrochemical environment, thereby shifting the thermodynamic preference for specific surface terminations.

However, the use of concentrated HF poses significant safety hazards due to its highly corrosive and toxic nature, limiting its widespread adoption in research laboratories.[23] Despite these safety concerns, HF etching remains a benchmark method for fundamental studies and for characterizing MXene properties.

To address the safety concerns associated with HF etching, the MILD method was developed by Ghidiu *et al.*[24] This approach involves *in situ* formation of HF by reacting lithium fluoride (LiF) with HCl, thereby eliminating the need to handle concentrated HF. The MILD method typically uses a mixture of LiF and HCl (typically 6–12 M) at elevated temperatures (35–60 °C) for 6–48 hours.[25] The reaction mechanism involves the following steps:

$$LiF + HCl \rightarrow HF + LiCl$$

$$Ti_3AlC_2 + 3HF \rightarrow Ti_3C_2F_x + AlF_3 + 1.5H_2$$

Compared with direct HF etching, the MILD (LiF/HCl) method reduces operator exposure to concentrated HF by generating fluoride species.[26] The method also yields improved delamination efficiency, with many MXene flakes spontaneously delaminating during the washing process.[27] Recent studies have shown that the LiF molarity significantly affects the synthesis efficiency and the quality of the resulting MXenes. LiF/HCl-etched MXenes show larger interlayer spacing yet higher conductivity because they form fewer F-rich terminations and defects, whereas HF etching produces smaller spacing but lower conductivity due to termination chemistry, defects, and poor interflake contact; however, with optimized conditions, it can lead to high-quality free-standing films.[28]

Several alternative fluoride-based etching methods have been developed to improve the synthesis process further and mitigate safety concerns. These include the use of ammonium hydrogen fluoride (NH_4HF_2), sodium fluoride (NaF) combined with HCl, and iron fluoride (FeF_3) systems.[29,30] The FeF_3/HCl system, in particular, has shown promise for producing MXenes with unique surface functionalization and iron intercalation between the layers.[31] These alternative methods offer distinct advantages in safety, cost-effectiveness, and the ability to tune MXene properties through controlled surface terminations.

A fluoride-free approach to MXene synthesis involves using molten salts at elevated temperatures. This method typically employs a mixture of KF and LiF at temperatures ranging from 550 to 650 °C for several hours.[32] The molten salt method offers several advantages, including the elimination of aqueous processing steps, reduced formation of oxide impurities, and the

ability to produce MXenes with different surface terminations.[33] However, the high-temperature processing and the need for specialized equipment limit its widespread adoption.

Recent developments in MXene synthesis have focused on Lewis acidic etching routes, which offer milder reaction conditions and better control over surface terminations.[34] These methods typically involve using Lewis acids, such as $AlCl_3$, $FeCl_3$, or $ZnCl_2$, in combination with various solvents. The Lewis-acidic etching approach offers opportunities for large-scale manufacturing and the production of MXenes with tailored properties.[35]

Fig. 2 outlines various etching methods and conditions used in the synthesis of MXenes, with particular focus on Ti_3AlC_2 and its derivatives. Etching is a critical step in MXene production, as it removes the "A" layer (*e.g.*, aluminum) from the MAX phase precursor to yield layered MXene sheets. The methods are categorized into HF-based etching and alternative chemical etching techniques, each with specific terminators and conditions. HF etching is a traditional and widely used method for MXene synthesis. The figure highlights three subtypes: *in situ* HF etching, Alkaline etching, and electrochemical etching. *In situ* HF etching involves generating HF indirectly within the reaction mixture, often using bifluorides such as HCl + LiF. Alkaline etching employs bases such as NaOH or macromolecular organic bases, while electrochemical etching uses an applied potential to facilitate the removal of the A layer. These methods are versatile but require careful handling due to HF's hazardous nature. For the precursor Ti_3AlC_2, the figure lists several alternative etchants, including bifluorides (HCl + LiF), NaOH, Ni_4Cl & TMA-OH, as well as Lewis acidic molten salts. These alternatives aim to mitigate the risks associated with HF while achieving efficient etching. Notably, bifluorides offer a safer route by releasing HF *in situ*, whereas Lewis acidic molten salts provide a high-temperature etching environment suitable for specific MXene derivatives. The choice of etchant influences the surface terminations and properties of the resulting MXene. The figure highlights the significance of surface terminations, which are functional groups such as –O, –OH, –F, and –Cl that stabilize MXene layers. The etching conditions, including room-temperature processes, influence these terminations. For instance, room temperature etching with bifluorides or NaOH can yield MXenes with varying ratios of –O, –OH, and –F groups, which are critical for applications in energy storage, catalysis, and composites.

4. Delamination and exfoliation strategies of MXenes

Following the etching process, the resulting multilayered MXenes must be delaminated and exfoliated to obtain single or few-layer nanosheets. The delamination process is crucial for realizing the full potential of MXenes, as many of their unique properties are maximized in the delaminated state.[7,37] Several

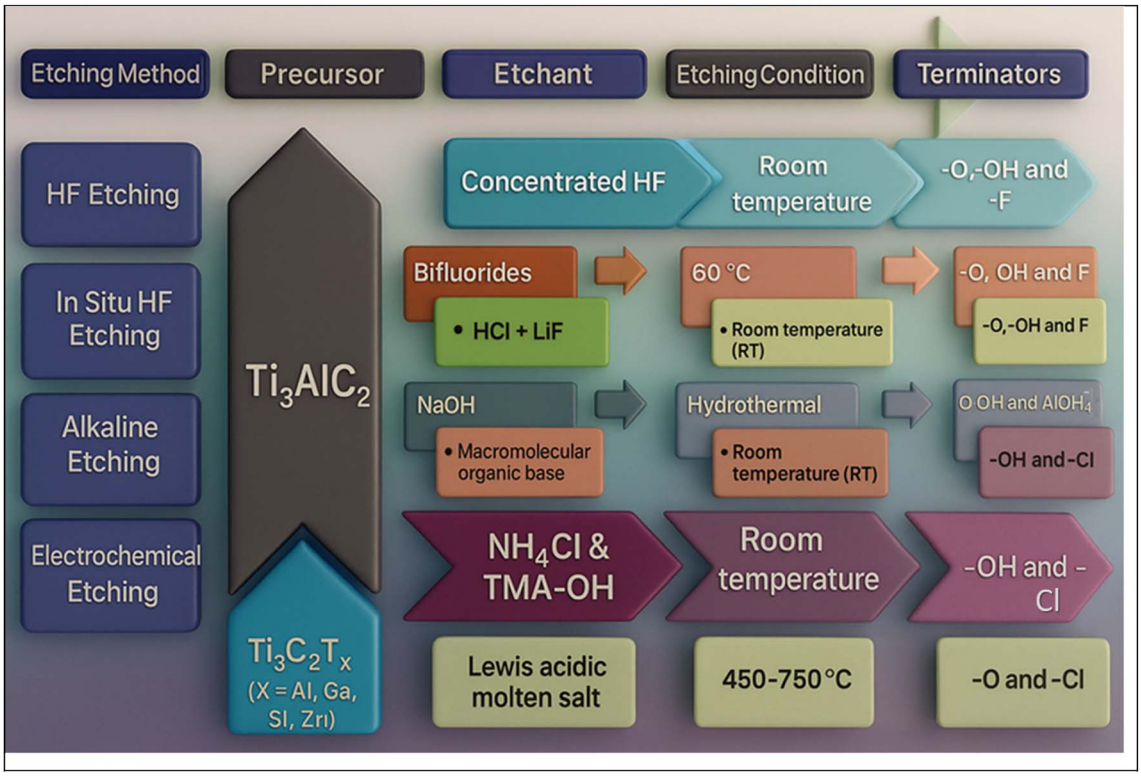

Fig. 2 Overview of etching methods for MXene synthesis, including HF-based techniques (*in situ* HF, alkaline, and electrochemical etching) and alternative etchants (bifluorides, NaOH, and Lewis acidic molten salts) for Ti_3AlC_2. Surface terminations (–O, –OH, –F, –Cl) and room-temperature conditions are highlighted, illustrating the diverse approaches to MXene production, this figure has been reproduced from ref. 36 with permission from American Chemical Society, copyright 2024.

strategies have been developed to achieve efficient delamination and exfoliation of MXenes.

The most common approach for MXene delamination involves intercalating organic molecules between the MXene layers, followed by sonication to separate the layers.[26] Various intercalating agents have been successfully employed, including DMSO, TBAOH, urea, and hydrazine.[38,39] The intercalation process typically involves immersing the multilayered MXene in the intercalating agent for several hours, allowing the molecules to penetrate between the layers and increase the interlayer spacing.[40]

DMSO has been widely used as an intercalating agent due to its ability to form stable intercalation compounds with MXenes. The process involves mixing the multilayered MXene with DMSO at room temperature for 6–24 hours, followed by washing with water and sonication to achieve delamination. The DMSO intercalation method can yield colloidal solutions of delaminated MXenes. However, colloidal concentration, flake size, and shelf-life vary considerably with sonication energy, washing cycles, and oxygen exposure during processing.[26,41]

TBAOH is another effective intercalating agent, particularly for MXenes synthesized *via* molten salt etching.[42] The TBAOH intercalation method involves treating the multilayered MXene with TBAOH solution, followed by sonication to separate the layers.[43] This method is effective for tuning the wetting behavior and surface properties of MXenes through controlled treatment times.[44]

Ultrasonication plays a crucial role in the delamination and exfoliation of MXenes, serving as the primary tool for separating the layers after intercalation.[45] The sonication process involves applying ultrasonic waves to the MXene suspension, creating cavitation bubbles that generate mechanical forces to separate the layers.[46] The sonication parameters, including power, frequency, and duration, significantly affect the delamination efficiency and the quality of the resulting nanosheets.[47]

Recent studies have demonstrated that ultrasonication can significantly accelerate the delamination process and yield a higher fraction of high-quality 2D sheets.[48] The sonication conditions must be carefully optimized to achieve efficient delamination while minimizing damage to the MXene sheets. Typically, mild sonication (40–60 W) is employed for 1–4 hours to achieve optimal delamination without causing significant structural damage.[49]

Mechanical exfoliation represents an alternative approach for MXene delamination that does not require chemical intercalation.[50] This method involves the direct mechanical separation of MXene layers through various techniques, including ball milling, shear mixing, and freeze–thaw cycles.[51] Mechanical exfoliation offers several advantages, including the elimination of chemical intercalants, reduced processing time, and the ability to produce large quantities of delaminated MXenes.[52]

Recent developments in mechanical exfoliation have focused on optimizing the processing conditions to achieve efficient delamination while maintaining the structural integrity of the MXene sheets.[53] The mechanical exfoliation approach has shown promise for industrial-scale production of delaminated MXenes, offering a more environmentally friendly and cost-effective alternative to chemical intercalation methods.[54]

Several alternative delamination methods have been explored to improve the efficiency and sustainability of MXene exfoliation. These include the use of biological molecules such as bovine serum albumin (BSA) as intercalating agents, which offer biocompatible and environmentally friendly alternatives to traditional chemical intercalants.[55] The use of ionic liquids and deep eutectic solvents has also been investigated as potential intercalating agents for MXene delamination.[56]

5. Surface functionalization methods

Surface functionalization is a crucial aspect of MXene synthesis and processing, as the surface terminations significantly influence the material's properties and performance in various applications.[4,57] The surface of MXenes can be modified through multiple approaches, including during synthesis (*in situ* functionalization) or post-synthesis treatments (*ex situ* functionalization). The ability to control and tune the surface chemistry of MXenes enables the tailoring of their properties for specific applications.

The surface terminations of MXenes are primarily determined by the etching conditions and the nature of the etching agent used during synthesis.[58] The most common surface terminations include –OH, –O, and –F groups, which are formed during the etching process.[59] The distribution and concentration of these terminations can be controlled by adjusting the etching conditions, such as the concentration of the etching agent, temperature, and reaction time.[60]

The choice of etching agent significantly influences the surface terminations of the resulting MXenes. For example, HF etching typically produces MXenes with mixed terminations of –OH, –O, and –F, whereas alternative etching methods can result in different termination patterns. The FeF_3/HCl etching system has been shown to produce MXenes with unique surface functionalization, including the incorporation of iron species between the layers.[61] Recent studies have focused on developing controlled functionalization strategies during the synthesis process to produce MXenes with specific surface terminations.[62] These approaches utilize various etching agents, additives, and processing conditions to achieve targeted surface functionalization.[63] The ability to control the surface terminations during synthesis offers advantages in terms of processing efficiency and the production of MXenes with tailored properties. Post-synthesis surface modification involves treating already synthesized MXenes to introduce new functional groups or modify existing ones.[64] This approach offers greater flexibility in tailoring MXene surface properties for specific applications. Various post-synthesis modification methods have been developed, including thermal treatment, chemical functionalization, and plasma treatment.[65] Heat treatment at different temperatures and atmospheres can lead to the removal of specific functional groups, the formation of new terminations, or the rearrangement of existing ones.[66] For instance, vacuum annealing has been reported to decrease surface oxygen content and concomitantly enhance the electrical conductivity of

Table 1 Outlines the MXene synthesis, delamination, and surface functionalization methods[a]

Processing stage	Method/agent	Type	Conditions	Duration	Surface terminations/ groups	Effectiveness	Key advantages	Limitations
Etching (synthesis)	Direct HF etching	Chemical	HF (40–50 wt%), ~25 °C	24–72 h	–F, –OH, –O	High	High yield, high crystallinity	Toxic, hazardous
	MILD method	Chemical	LiF + HCl, 35–60 °C	6–48 h	–F, –OH	High	Safer, spontaneous delamination	Sensitive to reagent ratio
	FeF_3/HCl etching	Chemical	FeF_3 + HCl, ~25 °C	24–48 h	–F, Fe intercalation	Moderate-high	Unique functionality, moderate risk	Limited scalability
	Molten salt etching	Thermal	$ZnCl_2$, KF, LiF (molten), 550–650 °C	2–6 h	–Cl, –O	High	Fluoride-free, high control	High temp., requires special setup
	Electrochemical etching	Electrochemical	Fluoride electrolyte, RT-60 °C	2–6 h	–O, –OH	Moderate-high	Precise control, eco-friendly	Complex setup
Delamination (intercalation)	DMSO	Organic solvent	Room temperature	6–24 h	N/A (preserves existing)	High	Good stability and flake size	Organic solvent use
	TBAOH	Organic base	Room temperature	2–6 h	N/A (preserves existing)	Very high	Promotes spontaneous delamination	Cost, handling requirements
	Li^+/Na^+ ions	Metal cation	Aqueous solution	2–4 h	N/A (preserves existing)	Moderate	Electrostatic mechanism	Limited effectiveness
	Urea	Organic	Room temperature	6–12 h	N/A (preserves existing)	Moderate	Biocompatible alternative	Slower process
	BSA	Biological	Room temperature	~12 h	N/A (preserves existing)	Emerging	Environmentally friendly	Still under development
Surface functionalization	HF/MILD etching	*In situ* chemical	During synthesis	Same as etching	–F, –OH, –O	High	Baseline terminations for MXenes	Limited functional diversity
	FeF_3-based etching	*In situ* chemical	During synthesis	Same as etching	Fe-containing, –F, –OH	High	Enhanced catalytic/ magnetic effects	Specific applications only
	Thermal treatment	*Ex situ* thermal	Controlled atmosphere, 200–600 °C	1–4 h	Controlled reduction	Moderate-high	Modifies conductivity & composition	Can damage the structure
	Chemical grafting	*Ex situ* chemical	Various reagents, RT-100 °C	2–24 h	–COOH, $–NH_2$, aromatic groups	Variable	Enables composite/ hybrid formation	Multi-step process
	Plasma treatment	*Ex situ* physical	Various plasmas, RT	Minutes-hours	–O, –OH (enhanced)	Moderate	Surface activation for sensing	Equipment intensive

[a] Notes: RT = room temperature, N/A = not applicable (method doesn't change surface terminations), effectiveness ratings: low, moderate, high, very high, surface terminations: –F (fluoride), –OH (hydroxyl), –O (oxide), –Cl (chloride).

MXenes by suppressing surface oxidation and improving interflake charge transport.[67] At relatively low annealing temperatures (typically below ~200 °C), thermal energy is generally insufficient to drive substantial termination rearrangement, defect healing, or interlayer structural relaxation, resulting in only minor changes to the electrical and structural properties. In contrast, annealing at elevated temperatures exceedingly approximately 400 °C, even under nominally inert or low-oxygen conditions, can promote irreversible oxidation of $Ti_3C_2T_x$ to TiO_2. This transformation leads to pronounced degradation of the layered structure and a severe reduction in electrical conductivity, thereby limiting the thermal processing window for MXene-based materials.

Chemical functionalization involves reacting MXenes with various chemical agents to introduce new functional groups on the surface.[68] This approach has been used to attach organic molecules, polymers, and nanoparticles to MXene surfaces, creating hybrid materials with enhanced properties.[69] The chemical functionalization of MXenes can be achieved through various mechanisms, including covalent bonding, electrostatic interactions, and π–π stacking.[70] The characterization of surface terminations in MXenes is crucial for understanding their properties and optimizing their performance in applications.[71] Various analytical techniques have been employed to study the surface chemistry of MXenes, including X-ray photoelectron spectroscopy (XPS), Fourier-transform infrared spectroscopy (FTIR), and nuclear magnetic resonance (NMR) spectroscopy.[72] These techniques provide information about the nature, concentration, and distribution of surface functional groups on MXenes.[73] The surface terminations of MXenes are often non-uniform and can vary across different regions of the material.[74] This heterogeneity in surface terminations can affect the overall properties of MXenes and must be considered when designing applications.[75] Recent advances in characterization techniques have enabled more detailed analysis of the surface chemistry of MXenes, providing insights into the structure–property relationships.[76]

The development of standardized characterization protocols for MXene surface terminations is crucial for ensuring reproducibility and comparability of results across different research groups.[71] The establishment of these protocols will facilitate the advancement of MXene research and accelerate the development of practical applications.[77] Table 1 provides a comprehensive comparison of MXene etching methods, highlighting critical parameters, including etchant systems, temperature, processing time, yield percentages, and key advantages and limitations for each approach. The table systematically compares conventional HF etching with alternative methods, including the MILD (LiF + HCl) technique, molten-salt etching, and electrochemical etching, enabling researchers to select

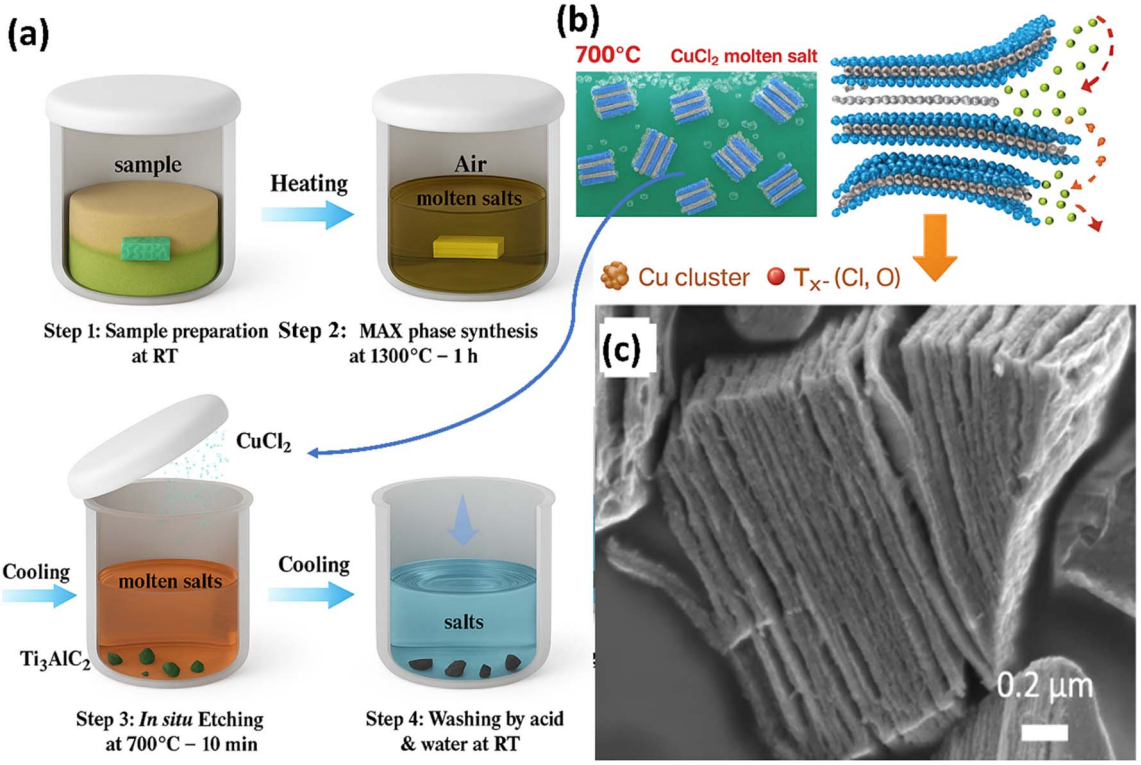

Fig. 3 (a) Schematic illustration of the one-pot synthesis of $Ti_3C_2T_x$ MXene in an air atmosphere. Elemental Ti, Al_2O_3, and graphite powders are mixed with NaCl and KCl salts in a specific mole ratio, pressed into pellets, and heated in a muffle furnace. Molten salts at 660 °C protect the reactants from oxidation, enabling the formation of the Ti_3AlC_2 MAX phase at 1300 °C for 1 hour. (b) Etching of the Ti_3AlC_2 MAX phase in molten $CuCl_2$ salt at 700 °C to produce $Ti_3C_2T_x$ MXene through aluminum removal and surface termination by Cl and O groups. (c) SEM image of $Ti_3C_2T_x$ MXene, showing characteristic layered morphology with an interlayer spacing conducive to ion diffusion; scale bar represents 0.2 μm, this figure has been reproduced from ref. 78 with permission from nature, copyright 2021.

optimal synthesis conditions based on safety, scalability, and the desired MXene properties.

Fig. 3a illustrates a schematic of the one-pot synthesis process for $Ti_3C_2T_x$ MXene conducted under an air atmosphere. In this process, stoichiometric amounts of elemental titanium (Ti), aluminum oxide (Al_2O_3, representing alumina), and graphite (C) powders are intimately mixed with a chloride salt mixture of sodium chloride (NaCl) and potassium chloride (KCl). The mixture is pressed into a pellet using a steel die to ensure compactness and uniformity. The prepared pellet is placed inside a crucible and fully covered with additional NaCl/KCl salt mixture, forming a protective salt bed. The crucible is then heated in a muffle furnace under ambient air. At around 660 °C, NaCl and KCl melt, creating a molten-salt medium. This molten medium plays a crucial role: it prevents the oxidation of reactants at elevated temperatures by physically isolating them from direct exposure to air. The MAX phase (Ti_3AlC_2) synthesis is achieved by maintaining the temperature at 1300 °C for 1 hour. This process successfully produces the MAX phase, as confirmed by X-ray diffraction (XRD) analysis. The final Ti_3AlC_2 is recovered *via* vacuum filtration and dried at 80 °C for 12 hours. A similar method is used to synthesize Ti_2CT_x MXene; further details are provided in the experimental techniques section.

Fig. 3b represents the subsequent etching step for MAX phase conversion. The synthesized MAX phase (Ti_3AlC_2) is immersed in a molten Lewis salt of $CuCl_2$ at 700 °C. This molten salt serves as both a medium and an active agent for etching the aluminum (Al) layers from the Ti_3AlC_2 structure. Through this *in situ* etching, copper ions facilitate the removal of Al while simultaneously promoting the surface termination of the resultant $Ti_3C_2T_x$ layers with Cl- and O-functional groups. This etching environment enables the breakdown of the layered MAX phase into 2D $Ti_3C_2T_x$ MXene sheets, which are rich in surface terminations crucial for their electronic and electrochemical properties.

Fig. 3c presents a SEM image of the synthesized $Ti_3C_2T_x$ MXene. The image reveals the layered, accordion-like morphology typical of MXene materials, confirming successful exfoliation and etching of the MAX phase. The distinct layered structure shown is critical for applications that rely on MXenes' high surface area, electrical conductivity, and accessible interlayer spacing. The scale bar indicates 0.2 μm, emphasizing the nanostructured nature and the well-defined lamellar architecture of the obtained $Ti_3C_2T_x$ sheets.

6. Structure–property relationships of MXene nanosheets

MXenes inherit their basic layered structure from their parent MAX phases, in which layers of transition metal carbides or nitrides are interleaved with layers of A-group elements. Upon selective etching of the A element (*e.g.*, Al), the remaining M–X layers are freed, forming stacks of $M_{n+1}X_n$ nanosheets terminated with functional groups. This 2D morphology confers a high aspect ratio, large surface area, and unique electronic characteristics. The transition metal layers contribute d-orbitals that significantly influence the electronic properties of MXenes. Density functional theory (DFT) calculations have revealed that many MXenes are metallic or exhibit high electrical conductivity due to their partially filled d-band states.[2] However, the exact electronic behavior depends on both the metal composition (*e.g.*, Ti, Nb, Mo) and surface functionalization. For instance, pristine Ti_3C_2 is metallic; however, when functionalized with –OH or –O groups, it can exhibit semiconducting behavior due to the opening of its band gap.

Moreover, the ability to tune the electronic structure *via* substitutional doping or alloying further expands MXene functionality. Ternary or quaternary MXenes (*e.g.*, Mo_2TiC_2, TiVNbC) exhibit tailored band structures, magnetic properties, and charge-transport characteristics, enabling their integration into advanced electronic and spintronic systems.

One of the most distinctive features of MXenes is their tunable surface chemistry. During etching and post-treatment, the basal planes and edges of MXene sheets are typically terminated with various functional groups, including hydroxyl (–OH), oxygen (–O), fluorine (–F), and chlorine (–Cl), depending on the synthesis route.[71]

These surface terminations have a profound impact on hydrophilicity, electrochemical activity, and interaction with guest species. For instance, –OH and –O groups enhance hydrophilicity and hydrogen bonding capacity, making MXenes excellent candidates for aqueous dispersions and interfacial interactions in composite systems. In electrochemical applications, surface terminations can contribute pseudocapacitance *via* redox-active sites, improving charge storage capabilities.

Furthermore, surface functional groups influence ion intercalation behavior in battery systems. Studies have shown that oxygen-terminated MXenes exhibit improved capacity and cycling stability due to stronger electrostatic interactions with Li^+, Na^+, or K^+ ions.[79] On the contrary, fluorinated surfaces may exhibit higher resistance to ion transport due to weaker binding and steric hindrance. Therefore, controlling surface terminations provides a pathway to optimizing MXene nanosheets for targeted applications.

As ultrathin 2D materials, MXene nanosheets exhibit unique behaviors associated with dimensional confinement. When exfoliated to monolayer or few-layer thicknesses, the confinement of charge carriers and phonons alters the optical, electrical, and mechanical properties compared to their bulk counterparts.

Thin MXene flakes show enhanced electrical conductivity due to reduced interlayer resistance and more effective charge delocalization across the sheet. This makes delaminated MXenes highly suitable for applications such as transparent conductive films, antennas, and supercapacitor electrodes.[80] At the same time, their thin nature provides mechanical flexibility and stretchability, which are useful for wearable electronics and soft sensors.

Moreover, the thickness-dependent properties extend to intercalation behavior. Thinner MXene sheets offer shorter diffusion paths and larger accessible surface area for ions, improving their rate capability and specific capacity in electrochemical devices. However, excessive thinning can lead to

restacking and aggregation, which must be mitigated using interlayer spacers or surfactants.

Defects, including vacancies, grain boundaries, and edge dislocations, are intrinsic to most MXene nanosheets due to the chemical processing involved in their synthesis. While defects can act as charge traps or structural weak points, they may also serve as active sites for catalysis or sensing.

For example, vacancies on the M or X sites can enhance electrocatalytic activity by providing under-coordinated atoms that facilitate reaction kinetics. Similarly, edge defects can improve sensitivity in chemical sensing applications by increasing surface reactivity toward analytes. However, excessive defect density can negatively impact conductivity, mechanical strength, and long-term stability. Therefore, post-synthesis treatments, such as annealing, chemical healing, or controlled doping, are used to tailor defect levels in MXene structures.

Crystallinity is another structural aspect that influences properties. Highly crystalline MXene flakes exhibit more uniform electronic transport and fewer scattering centers, beneficial for field-effect transistors or electromagnetic shielding.[81] Conversely, amorphous or partially disordered MXenes may offer more reactive sites, advantageous for catalysis or adsorption-based applications.

In multilayered MXene stacks, interlayer interactions governed by van der Waals forces and electrostatic attraction can influence overall performance. While these stacks are structurally stable, they tend to restack due to attractive forces between adjacent layers, particularly during drying or film formation. Restacking reduces the accessible surface area, blocks active sites, and hinders ion diffusion, thereby compromising performance in applications such as batteries or supercapacitors. To address this, researchers have developed various strategies to control interlayer spacing:

- Intercalation of organic molecules, ions, or polymers to maintain expanded interlayer spacing.
- Hydrogel or composite formation to prevent the collapse of exfoliated layers.
- Pillaring techniques using spacers such as carbon nanotubes, graphene oxide, or silica nanoparticles.

By engineering the interlayer distance, it is possible to maximize ionic accessibility, maintain structural integrity, and improve the overall electrochemical or adsorption performance of MXenes.

Due to their 2D structure, MXene nanosheets exhibit strong anisotropy in their mechanical, thermal, and electrical properties. In-plane conductivity is typically several orders of magnitude higher than out-of-plane conductivity, owing to the extended conjugated network of metal-carbide/nitride bonds within each layer. This makes MXenes ideal for applications where directional conduction is desired, such as in planar supercapacitors or interconnects.[82]

Mechanical anisotropy is also observed, with high Young's modulus and tensile strength in-plane, and relatively weak interlayer cohesion. This property is advantageous for processes such as layer exfoliation and mechanical deformation, but poses challenges for the long-term mechanical stability of composites or freestanding films.

The surface chemistry of MXene nanosheets is a defining feature that governs many of their unique physicochemical properties and directly impacts their applications across various fields, including energy storage, catalysis, sensing, and environmental remediation. MXenes possess a rich, tunable surface chemistry arising from the presence of functional groups, commonly denoted as Tx, attached to their surfaces during synthesis.[71] These surface terminations typically include hydroxyl (–OH), oxygen (–O), fluorine (–F), and, less commonly, chlorine (–Cl) groups, which are primarily formed by selective etching of their parent MAX phases with fluorine-containing acids or other chemical agents. The nature, density, and distribution of these surface functional groups critically influence MXene properties, including hydrophilicity, colloidal stability, electrochemical activity, and interfacial interactions. Among these, hydrophilicity is especially important, as it enables MXenes to disperse well in aqueous media, facilitating solution processing and their use in aqueous-based composites, inks, and films. Unlike many other 2D materials such as graphene or transition metal dichalcogenides, which are generally hydrophobic or require surface modification for dispersion in water, MXenes exhibit intrinsic hydrophilicity due to their abundant surface –OH and –O terminations.[68] This hydrophilicity promotes strong hydrogen bonding with water molecules, yielding stable colloidal suspensions that do not require surfactants or additional functionalization.

Surface terminations also modify the electronic structure and chemical reactivity of MXenes. For example, oxygen- and hydroxyl-terminated surfaces typically enhance electrochemical performance by providing redox-active sites and facilitating charge transfer processes, which are crucial for supercapacitor electrodes, batteries, and electrocatalysts. The presence of –OH groups can also enhance biocompatibility and promote the adsorption of biomolecules, enabling MXenes to serve as effective biosensing platforms or drug-delivery carriers.

Fig. 4a illustrates the bending durability of the M-NCY-30 fiber supercapacitor. The mechanical flexibility of MXene-based fibers is critical for wearable applications, and the data presented highlight the supercapacitor's structural integrity and electrochemical stability under repeated bending cycles. This durability ensures reliable performance during dynamic movements in smart textiles and wearable devices.

Fig. 4b shows a real-world application of the M-NCY-30 supercapacitor, demonstrating its ability to serve as a flexible energy storage unit integrated into textiles. This practical deployment confirms its potential for powering compact and wearable electronic systems, offering a balance between flexibility, mechanical strength, and stable energy output.

Fig. 4c presents an optical image of MXene/graphene oxide (GO) fibers co-knitted with nylon yarn into a textile prototype. The co-knitting of conductive MXene/GO fibers with conventional yarns exemplifies a scalable fabrication. The hybrid structure leverages the mechanical robustness of nylon and the high conductivity of MXene/GO to deliver intelligent functionality without compromising wearability.

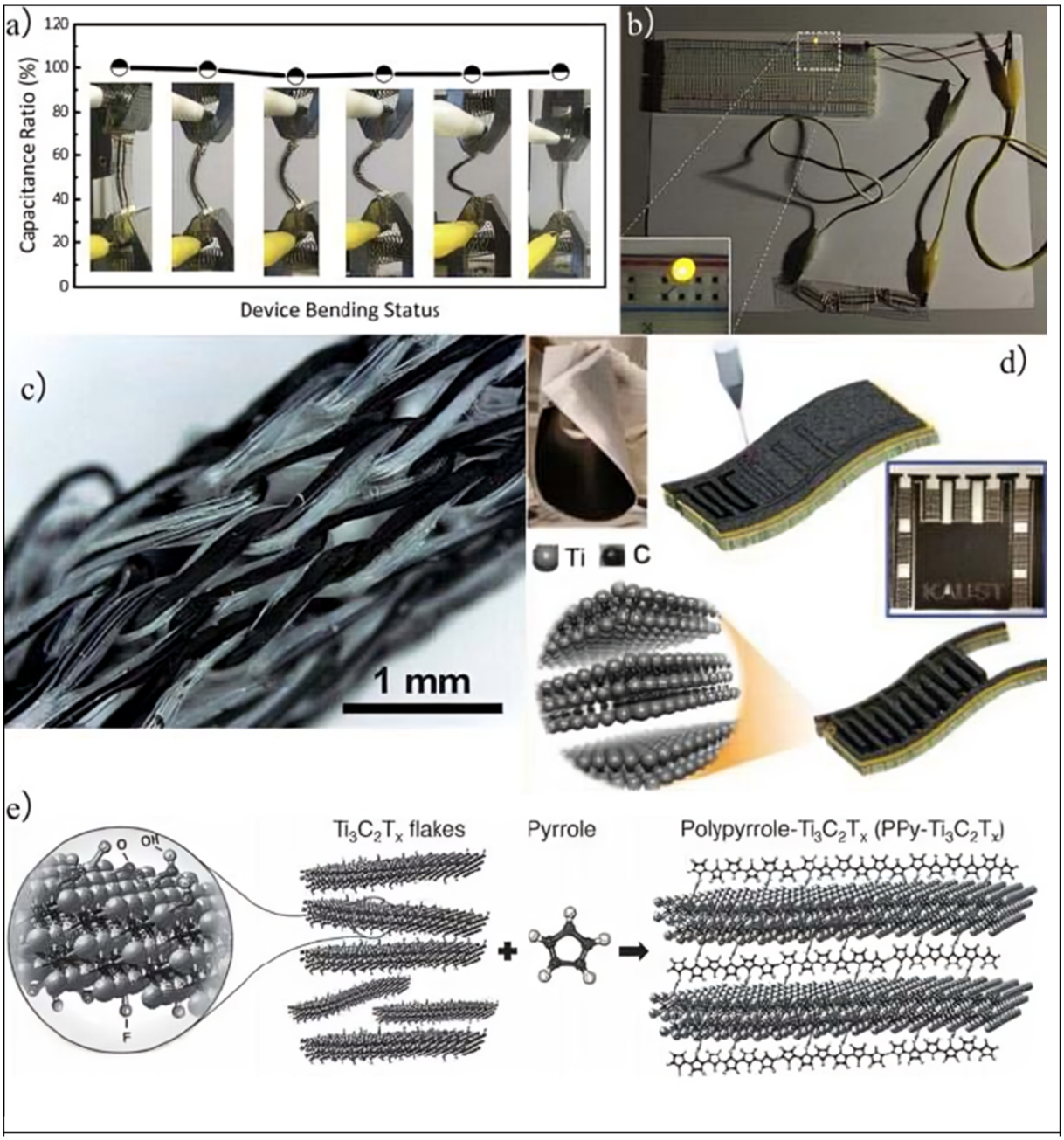

Fig. 4 (a) Bending durability and (b) real-time application of the M-NCY-30 fiber supercapacitor. (a and b) Figures has been reproduced from ref. 83 with permission from Elsevier, copyright 2018. (c) Optical image of MXene/graphene oxide (GO) fiber co-knitted with nylon yarn into a textile prototype, this figure has been adapted from ref. 84 with permission from Royal Society of Chemistry, copyright 2017. (d) Flexible micro-supercapacitors fabricated by laser patterning on MXene-coated paper, this figure has been adapted from ref. 85 with permission from IOPscience, copyright 2021. (e) Schematic representation of pyrrole polymerization between MXene nanosheet layers for enhanced pseudocapacitance and mechanical robustness. These composite structures demonstrate the high electrical conductivity and flexibility of MXene-based materials, as well as their potential for integration into next-generation wearable energy storage systems, this figure has been reproduced from ref. 86 with permission from WILEY, copyright 2016.

Fig. 4d depicts a flexible micro-supercapacitor (micro-SC) fabricated *via* laser patterning on MXene-coated paper. This method provides a low-cost, scalable approach to designing flexible, integratable microscale energy storage devices. The high surface area and conductivity of MXene, combined with precise laser patterning, enhance electrochemical performance, including rapid charge/discharge rates and long cycle stability.

Fig. 4e presents a schematic illustration of the pyrrole polymerization process between MXene layers. This interlayer polymerization creates pseudocapacitive networks that boost charge storage performance by enhancing redox reactions within the layered MXene structure. The hybrid design maintains the structural benefits of MXene while increasing

capacitance and energy density through the pseudocapacitive contribution of polypyrrole.

Controlling the surface chemistry through synthesis conditions or post-synthesis treatments provides a versatile means to tailor MXene properties. For instance, varying the etching environment, reaction time, temperature, or post-etching washing protocols can influence the relative abundance of –F, –OH, and –O groups on the MXene surface.[87] Thermal annealing and chemical treatments have been shown to selectively reduce fluorine terminations and increase oxygen or hydroxyl coverage, thereby enhancing conductivity and chemical stability.

Moreover, the tunable hydrophilicity affects MXene's interactions with polymers and other composite components, impacting mechanical strength, electrical conductivity, and processability in hybrid materials. Hydrophilic MXenes can form strong interfacial bonds with hydrophilic polymers *via* hydrogen bonding or electrostatic interactions, yielding composites with improved mechanical reinforcement and enhanced charge-transport pathways.

Despite their inherent hydrophilicity, MXenes can also be chemically modified to adjust their wettability for specific applications. For example, surface functionalization with alkyl silanes or polymer grafting can impart hydrophobic characteristics, enabling MXenes to be used in oil/water separation membranes or hydrophobic coatings.[88]

The surface chemistry of MXenes is characterized primarily by functional groups such as oxygen (–O), hydroxyl (–OH), and fluorine (–F), introduced during the selective etching of their parent MAX phases and subsequent processing steps. These surface terminations play a crucial role in determining the physical, chemical, and electronic properties of MXenes, ultimately affecting their performance across a broad range of applications, including energy storage, catalysis, sensing, and environmental remediation. The types, distribution, and density of these surface functional groups can be precisely modulated by varying key synthesis parameters such as etching duration, temperature, and post-etching treatments, allowing for tunable surface chemistry tailored to specific needs.[89]

Advanced spectroscopic techniques, particularly X-ray photoelectron spectroscopy (XPS) and nuclear magnetic resonance (NMR) spectroscopy, have played a crucial role in elucidating the composition and chemical environment of MXene surface terminations. These analyses have revealed that the surface termination chemistry is highly sensitive to the conditions employed during synthesis. For example, titanium carbide MXene ($Ti_3C_2T_x$) synthesized *via* HF etching typically exhibits a complex surface composed of a mixture of –O, –OH, and –F groups.[90] The relative abundance of these terminations varies significantly depending on parameters such as HF concentration, etching time, temperature, and subsequent washing or annealing protocols.

In contrast, milder etching conditions and post-etching treatments favor hydroxyl and oxygen terminations. The presence of –OH and –O groups is generally preferred to enhance MXene hydrophilicity and improve electrochemical activity, whereas excessive fluorination can detrimentally affect electrical conductivity and chemical stability. Consequently, controlling the surface termination profile is critical for optimizing MXene performance in devices such as supercapacitors, batteries, and sensors.

Moreover, post-synthesis modifications, including thermal annealing, chemical etching, or plasma treatment, have been shown to selectively remove or convert surface groups, further refining the MXene surface chemistry.[91] For instance, annealing in inert or reducing atmospheres can reduce fluorine content and increase oxygen-based terminations, enhancing electrical conductivity and environmental stability. Alternatively, chemical treatments can functionalize the surface with additional groups tailored for specific applications, such as amines or thiols, to enhance sensing or catalytic behavior.

MXenes exhibit exceptional hydrophilicity due to polar surface terminations, particularly hydroxyl (–OH) and oxygen (–O) groups. The contact angle of water on MXene surfaces is typically less than 20°, indicating superhydrophilic behavior. This high hydrophilicity facilitates the dispersion of MXenes in aqueous solutions, enabling the formation of stable colloidal suspensions without the need for surfactants.[27]

The hydrophilic nature of MXenes also enhances their interaction with polar solvents and electrolytes, making them suitable for aqueous-based applications such as supercapacitors and batteries. The surface energy of MXenes is estimated to be 70–80 mJ m^{-2}, which is higher than that of graphene (46 mJ m^{-2}) but lower than that of graphene oxide (62 mJ m^{-2}).[7]

The hydrophilic surface chemistry and intrinsic layered structure of MXene nanosheets facilitate efficient ion intercalation and exceptional pseudocapacitive energy storage capabilities. The abundant surface terminations, typically consisting of –O, –OH, and –F groups, provide numerous active sites for faradaic redox reactions. At the same time, the interlayer spacing between MXene sheets creates accessible channels that can accommodate hydrated ions from electrolytes. This unique combination enables rapid and reversible charge transfer processes, underpinning the pseudocapacitive behavior characteristic of MXenes. Unlike conventional electrical double-layer capacitors, which rely solely on electrostatic charge accumulation at electrode/electrolyte interfaces, MXenes leverage faradaic reactions at their surface functional groups, resulting in significantly enhanced charge storage capacities.

The charge storage mechanism in these MXene electrodes involves a synergistic combination of electrical double-layer capacitance and pseudocapacitance; the latter arises from fast redox reactions occurring at surface terminations, particularly oxygen and hydroxyl groups, that can undergo reversible electron transfer. This dual mechanism enables MXenes to achieve both high energy density and power density, positioning them as promising candidates for next-generation supercapacitors.

Furthermore, the layered morphology of MXenes facilitates facile ion diffusion within the interlayer galleries, reducing diffusion resistance and enhancing rate capabilities even at high charge–discharge speeds. The tunable interlayer spacing, which can be modulated by varying synthesis conditions or post-synthesis treatments, allows optimization for different ion

sizes and solvent environments, thereby broadening the electrolyte compatibility of MXene electrodes. The hydrophilic surface additionally promotes strong electrolyte wetting and stable electrode/electrolyte interfaces, which are crucial for long-term cycling stability and capacitance retention.

The reactive surface terminations of MXene nanosheets offer versatile platforms for chemical functionalization and surface modification, enabling precise tailoring of their physicochemical properties to meet the requirements of specific applications.[75] These surface groups, primarily consisting of –O, –OH, and –F functionalities, provide abundant sites for covalent and non-covalent interactions, facilitating a wide range of functionalization strategies. Common approaches include the covalent attachment of organic molecules, polymer grafting, and decoration with metal or metal oxide nanoparticles. Such modifications are instrumental in enhancing MXene stability, improving selectivity, and boosting performance in diverse fields such as chemical sensing, catalysis, and energy storage devices.

For instance, the covalent grafting of alkyl chains onto MXene surfaces has been demonstrated to significantly enhance their dispersibility and stability in organic solvents, which is crucial for processing in non-aqueous media. This functionalization also improves compatibility with hydrophobic polymer matrices, thereby enabling the fabrication of MXene-based composite materials with superior mechanical strength and electrical conductivity.[92] The ability to seamlessly integrate MXenes into polymer matrices expands their applicability in flexible electronics, EMI shielding, and structural composites.

In another notable example, MXene nanosheets have been decorated with noble metal nanoparticles, such as gold, platinum, or palladium, to enhance their catalytic activity and selectivity. The synergistic effects arising from intimate contact between MXene substrates and metal nanoparticles increase the active surface area and improve charge-transfer kinetics, which are crucial for catalysis. Mehrpooya *et al.*[93] demonstrated that noble-metal-decorated MXenes exhibit superior catalytic performance in reactions including hydrogen evolution, oxygen reduction, and selective organic transformations. This approach leverages the conductive and chemically active MXene platform to stabilize and disperse metal nanoparticles, preventing aggregation and maximizing catalytic efficiency.

7. Electrical conductivity and electronic properties

MXene nanosheets, owing to their unique 2D structure and rich electronic configurations, exhibit exceptional electrical conductivity and tunable electronic properties.[94]

The electrical conductivity of MXenes depends strongly on their transition-metal composition and atomic configuration. The pristine (non-functionalized) forms of most MXenes are metallic due to the delocalized d-electrons from the transition metal atoms.[95] For example, Ti_3C_2, Ti_2C, and Nb_2C are known to be metallic in their ideal, termination-free forms. These materials exhibit high electronic density of states (DOS) at the Fermi level, allowing free electrons to move with minimal resistance.

However, the introduction of surface terminations (–O, –F, –OH), which is unavoidable during synthesis, particularly when using HF or *in situ*-generated HF, significantly affects the band structure. First-principles calculations have shown that functionalization can induce semiconducting behavior in otherwise metallic MXenes. For example, oxygen-terminated Ti_2CO_2 exhibits a semiconducting band gap of approximately 0.92 eV, which is absent in its pristine metallic form.[96] Similarly, Mo_2CO_2 and Sc_2CO_2 exhibit semiconducting properties due to strong orbital hybridization between the oxygen p-orbitals and the transition-metal d-orbitals. This tunability of the bandgap *via* surface functionalization makes MXenes excellent candidates for optoelectronic and sensor devices.

MXenes, particularly $Ti_3C_2T_x$, are among the very few two-dimensional material families that combine bulk metallic conductivity with solution processability. Freestanding $Ti_3C_2T_x$ films have been reported to exhibit electrical conductivities exceeding 10 000 S cm^{-1}, which are substantially higher than those of most other solution-processable conductive materials, including conductive polymers. This exceptional conductivity originates from the strong covalent bonding within the M–X layers and the presence of delocalized Ti d-electrons, which enable efficient in-plane charge transport.[97]

The broad range of electrical conductivity values reported for $Ti_3C_2T_x$, spanning approximately 500 S cm^{-1} to over 10 000 S cm^{-1}, does not reflect inconsistencies or contradictions in the literature. Rather, it is the predictable consequence of several well-defined and experimentally controllable factors that strongly influence charge transport.[98]

The broad range of electrical conductivity values reported for $Ti_3C_2T_x$, spanning approximately 500 S cm^{-1} to over 10 000 S cm^{-1} does not reflect inconsistencies or contradictions in the literature. Rather, it is the predictable consequence of several well-defined and experimentally controllable factors that strongly influence charge transport.

First, film microstructure and flake alignment play a dominant role. Vacuum-filtered films composed of well-delaminated, single-layer MXene flakes typically exhibit strong in-plane orientation and minimal interflake resistance, consistently achieving conductivities above 10 000 S cm^{-1}. Vacuum-filtered films consistently demonstrate high conductivity: Zhang *et al.*[34] achieved 15 100 S cm^{-1}, while Li *et al.*[99] reported up to 20 000 S cm^{-1} and Zhuang *et al.*[100] achieved 16 600 S cm^{-1} all exceeding the stated 10 000 S cm^{-1} threshold. Chen *et al.*[101] confirmed 12 800 Ω^{-1}. m^{-1} for vacuum-filtered films.

In contrast, films prepared by spray coating or other non-directional methods often display random stacking and increased grain-boundary scattering, resulting in significantly lower conductivities than 10 000 S cm^{-1}.[102,103] Importantly, $Ti_3C_2T_x$ films exhibit pronounced electrical anisotropy, with in-plane conductivity exceeding out-of-plane conductivity by one to two orders of magnitude.[104,105] Consequently, measurement orientation alone can account for substantial differences in reported values.

Second, the oxidation state of the MXene at the time of measurement critically affects conductivity. The multiple

studies demonstrate that freshly synthesized samples exhibit markedly higher conductivity than aged samples.

Osama *et al.*[106] found that a $Ti_3C_2T_x$ film's conductivity decreased by nearly one order of magnitude after one year of storage in nitrogen, despite only minor surface oxidation. Mičušík *et al.*[107] used XPS to directly observe progressive Ti^{4+} development and TiO_2 formation during air aging. Römer *et al.*[108] demonstrated that oxidation state changes are reversible, with film resistivity switching between 5.6 μΩm (oxidized) and 4.6 μΩm (reduced) *via* plasma treatment. Lipatov *et al.*[27] These findings collectively validate the caution recommended for low conductivity values without documented sample history. As a result, films characterized shortly after synthesis typically exhibit markedly higher conductivity than those measured after prolonged exposure to ambient conditions. Conductivity values below approximately 2000 S cm^{-1} should therefore be interpreted cautiously when sample age and storage conditions are not explicitly reported.

Third, measurement geometry significantly influences the extracted conductivity values. Two-probe configurations inherently include contact resistance contributions and therefore tend to underestimate intrinsic film conductivity. In contrast, four-probe or van der Pauw measurements performed on films of comparable thickness routinely yield conductivities up to an order of magnitude higher.

Pöhls *et al.*[109] confirm that discrepancies in reported electrical conductivities underscore the critical role of measurement methodologies and note that contact resistance strongly affects measured conductivities. Gao *et al.*[110] demonstrates that four-probe measurements themselves can suffer "significant systematic error", producing "arbitrarily high measured conductivity", complicating simple geometry comparisons. Veazey *et al.*[111] confirm that geometry effects are substantial, but show accuracy depends on contact separation and sample dimensions rather than geometry type alone. The standardization requirement is strongly supported across multiple sources, though the specific magnitude of two-probe underestimation *versus* four-probe/van der Pauw overestimation remains incompletely characterized in the available literature. Meaningful comparison of conductivity data across studies is thus only valid when identical measurement geometries and appropriate thickness normalization are employed.

Fourth, surface termination chemistry exerts a non-negligible influence on charged transport. Fluorine terminations are known to withdraw electron density from the Ti d-band, thereby reducing carrier mobility, whereas –O and –OH terminations enhance hydrophilicity but may induce partial bandgap opening. Berdiyorov *et al.*[112] found that fluorinated samples exhibit the highest transmission, up to 4 times that of bare MXene, while oxidation reduces transmission. Khanal *et al.*[113] confirmed that pristine Ti_3C_2 exhibits higher conductivity than functionalized versions, with –O terminations showing lower conductivity than –OH terminations. The number of MXene layers also affects electronic conductivity. Monolayer and few-layer $Ti_3C_2T_x$ typically exhibit higher conductivity than thicker multilayer stacks due to reduced interlayer resistance and enhanced charge carrier delocalization.

Collectively, these considerations underscore that reported conductivity values for $Ti_3C_2T_x$ must be interpreted within the full experimental context. Direct comparison across studies is only scientifically meaningful when synthesis conditions, termination chemistry, film morphology, oxidation state, and measurement protocols are carefully accounted for. Establishing standardized reporting practices for conductivity measurements will be essential for enabling meaningful cross-study comparisons and accelerating the rational design of MXene-based electronic materials.

Carrier mobility in MXenes is also notable. For example, $Ti_3C_2T_x$ nanosheets exhibit electron mobilities on the order of 100 cm^2 V^{-1} s^{-1}. While these values are lower than those of pristine graphene, they are considerably higher than most conventional 2D semiconductors. Incorporation of graphene significantly reduced the surface roughness of the composite films. Electrical measurements revealed a clear enhancement in electrical conductivity and Hall carrier mobility with increasing graphene concentration, achieving values of 9.5×10^4 S cm^{-1} and 54.58 cm^2 V^{-1} s^{-1}, respectively, with only 2.5 wt% graphene. These results position the MXene-based composite among the most electrically conductive MXene materials reported to date.[114] This combination of high mobility and high conductivity makes MXenes suitable for high-performance field-effect transistors (FETs), EMI shielding, and flexible electronic circuits.

Surface terminations have a significant impact on the electrical properties of MXenes, modifying their electronic structure, work function, and carrier density. Oxygen- and hydroxyl-terminated surfaces typically lead to a slight decrease in conductivity due to electron localization and bandgap opening. Fluorine terminations, which are electronegative and bulky, may also reduce conductivity by scattering carriers and reducing orbital overlap between adjacent atoms.

Moreover, the type and density of surface terminations directly influence the work function of MXenes. For instance, the work function (WF) tuning behavior of $Ti_3C_2T_x$ MXene, where T_x represents surface terminations, was systematically investigated for samples synthesized *via* both conventional HF etching and the more recent molten-salt etching route. Gas-phase surface reactions enabled WF modulation exceeding 0.6 eV, demonstrating precise control over electronic properties. Specifically, the WF increased from ~4.23 eV in N-doped MXene produced by molten salt etching to ~4.85 eV in N-doped MXene generated through HF etching. Density functional theory (DFT) calculations further supported these results, predicting WF tuning over >1 eV by modifying surface terminal groups (bare metal, F, O, N, and Cl). The observed WF variations arise from changes in surface terminations and the formation of TiO_2 and TiN phases during annealing. DFT analysis also revealed an inverse correlation between the WF and the electron affinity of terminal groups.[115]

Tailoring surface chemistry through post-synthesis treatments (*e.g.*, thermal annealing, chemical substitution, or plasma treatments) can partially remove or replace

terminations, thereby restoring metallic behavior and enhancing electrical performance. For example, thermal annealing in inert atmospheres has been shown to improve conductivity by reducing surface functional groups.

Structural defects, vacancies, and grain boundaries introduced during synthesis and exfoliation can have a dual role in electrical properties. On one hand, they may serve as scattering centers, reducing carrier mobility and increasing resistance. On the other hand, defects can introduce localized electronic states that enhance certain functionalities, such as catalysis or sensing, by creating active sites for charge-transfer reactions.

Doping is another strategy to modulate MXene's electrical properties. Substitutional doping with heteroatoms (*e.g.*, S, N, B) or transition metals can alter the carrier concentration, band structure, and conductivity.[116] MXenes hold strong promise for advanced electronics and sensing technologies. In this study, metallic Ti_3C_2 MXene, with a work function of 4.60 eV, forms excellent electrical contacts with both zinc oxide (ZnO) and tin monoxide (SnO) semiconductors, exhibiting negligible band offsets. Leveraging this favorable interfacial alignment, both n-type ZnO and p-type SnO thin-film transistors (TFTs) were successfully fabricated using large-area Ti_3C_2 MXene as the gate, source, and drain electrodes. The resulting n- and p-type TFTs show balanced and robust performance, with field-effect mobilities of 2.61 and 2.01 $cm^2\ V^{-1}\ s^{-1}$ and switching ratios of 3.6×10^6 and 1.1×10^3, respectively. Complementary metal-oxide-semiconductor (CMOS) inverters constructed from these MXene-contacted TFTs exhibit a high voltage gain of 80 and an excellent noise margin of 3.54 V, equivalent to 70.8% of the ideal value, along with stable operation under a 100 Hz square-wave input. These findings highlight the strong potential of Ti_3C_2 MXene as a high-performance contact material in next-generation nanoelectronic devices.[117] Similarly, mechanical deformation of flexible substrates can alter band alignment and carrier mobility, which are relevant to wearable electronics.

Compared to other 2D materials, MXenes stand out due to their combination of high electrical conductivity, hydrophilicity, and processability. While graphene offers superior conductivity and mobility, it lacks functional groups and is typically hydrophobic, limiting its dispersion and chemical tunability.[99] In contrast, MXenes can be dispersed in water and are compatible with polymers and other materials.

In supercapacitors, MXenes demonstrate high power density due to rapid electron transport and capacitive behavior. Their conductivity is crucial for fast charge/discharge cycles and minimal ohmic losses.[118] In EMI shielding, MXene films offer excellent shielding effectiveness owing to their high conductivity and strong interlayer interactions, outperforming traditional materials such as carbon nanotubes or metal foils.

For electronic devices, MXenes have been utilized in sensors, FETs, and memory devices.[119] Their electronic tunability and high conductivity enable the sensitive detection of analytes through changes in resistance or capacitance. In batteries, especially lithium-ion and sodium-ion systems, MXenes serve as conductive scaffolds that enhance electron transport and mechanical stability.

Fig. 5a presents an innovative three-dimensional visualization of the periodic table, where elements are represented as colorful building blocks arranged in a spatial configuration that emphasizes their chemical relationships. The arrangement is specifically designed to highlight the elements most relevant to MXene formation, with transition metals prominently displayed in red blocks. This visual approach effectively demonstrates the M–A–X nomenclature system, where M represents transition metals (such as Ti, V, Cr, Nb, Mo), A represents A-group elements (like Al, Si, Ga), and X represents carbon or nitrogen atoms. The 3D structure helps viewers understand how these different element families combine to form the precursor MAX phases, which are subsequently etched to produce 2D MXenes. The color coding and spatial organization make it immediately apparent which elements can serve as building blocks for MXene synthesis, providing an intuitive understanding of the chemical diversity available in this material family.

Fig. 5b illustrates the fundamental layered architecture of MXenes, specifically depicting the $M_{n+1}X_n$ structure that results after selective etching of the A-layer from MAX phase precursors. The image showcases the characteristic 2D layered structure, in which transition-metal (M) layers alternate with carbon or nitrogen(x) layers, forming a sandwich-like arrangement that defines the MXene structure. The visualization clearly shows how surface terminations (T_x) are attached to the outer surfaces of the structure, which is a defining feature of MXenes that distinguishes them from other 2D materials. These surface terminations, including –OH, –O, and fluorine (–F) groups, are crucial for determining the material's properties and applications. The legend in the figure helps identify different atomic species and their roles within the structure, making it clear how the 2D nature is maintained while allowing surface functionalization tailored to specific applications. Fig. 5c adapted from the work of Chu *et al.*[120], provides specific examples of $Ti_3C_2T_x$ MXene STM images and their corresponding electronic properties, which are crucial for understanding how surface chemistry influences material behavior. Fig. 5d demonstrates that OH-rich terminations exhibit significantly higher density of states at the Fermi level (approximately 50 states per eV), leading to enhanced electrical conductivity and stronger contrast in scanning tunneling microscopy imaging compared to oxygen or fluorine-rich surfaces, which typically show around 30 states per eV. The panel also illustrates how different termination types create substantial variations in work function values, ranging from 1.81 to 6.04 eV, which directly impact the material's electronic properties and potential applications in energy storage and electronic devices. The visualization likely shows mixed termination scenarios, in which combinations of –OH, –O, and –F groups yield heterogeneous surface properties. The research demonstrates that electronic characteristics are primarily determined by the stoichiometric ratio of termination rather than their spatial distribution. Additionally, the MXenes exhibit metallic or semi metallic behavior due to their unique electronic band structure, which is primarily determined by the transition-metal d-orbitals and surface terminations. The electrical conductivity of MXene nanosheets ranges from 4600 to 15

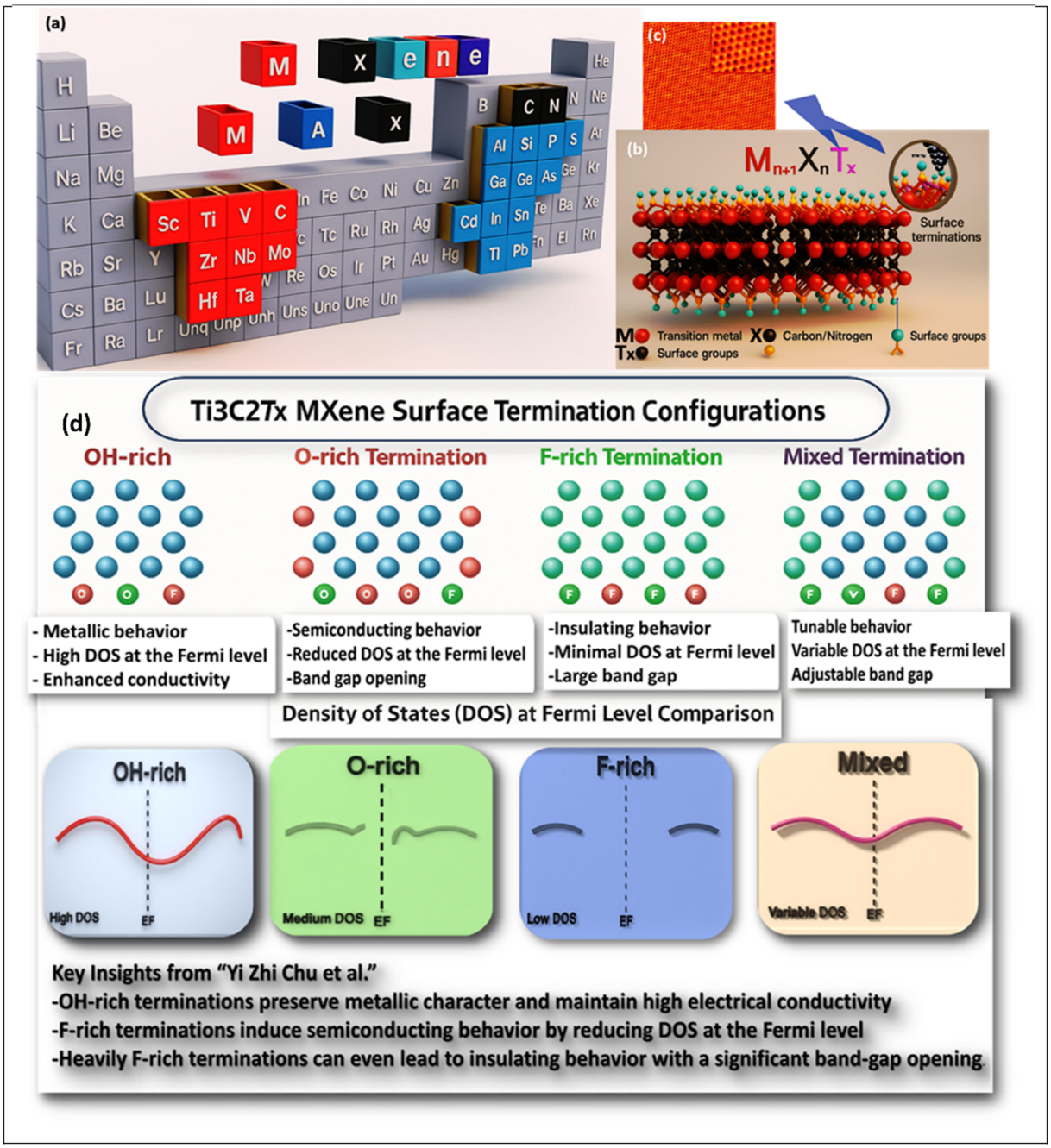

Fig. 5 (a) Three-dimensional periodic table highlighting the elements used in MXene synthesis. Schematic of the MXene crystal structure showing the characteristic $M_{n+1}X_n$ layered architecture after selective etching of the A-layer, with surface terminations (T_x) such as –OH, –O, and –F attached to the outer transition metal layers. (b) Atomic configuration of MXene showing transition metal layers (M), carbon/nitrogen layers (X), and surface functional groups (T_x). (c) Examples of $Ti_3C_2T_x$ STM image, this figure has been reproduced from ref. 120 with permission from iScience, copyright 2024, and (d) illustrating how OH-rich, O-rich, F-rich, and mixed terminations influence electronic properties, including variations in the density of states at the Fermi level.

100 S cm^{-1}, making them among the most conductive 2D materials.[12] The high conductivity arises from delocalized electrons in the transition-metal carbide/nitride layers, which form continuous conduction pathways. Theoretical studies using density functional theory (DFT) have shown that the electronic properties of MXenes are sensitive to surface terminations. For instance, $Ti_3C_2T_x$ with different surface terminations (–O, –OH, –F) exhibits varying electronic behavior, with oxygen-terminated surfaces showing higher conductivity than fluorine-terminated ones.[121]

The 2D nature of MXene nanosheets leads to quantum confinement effects that significantly modify their electronic properties relative to those of their bulk MAX phase counterparts. This structural confinement in single- or few-layer MXenes alters the band structure, increasing the electronic density of states at the Fermi level and thereby enhancing both

electrical conductivity and electrochemical activity. Among various MXene compositions, $Ti_3C_2T_x$ is the most extensively studied, and its performance illustrates the profound effect of layer thickness and surface terminations on electronic behavior. Experimental studies by Lukatskaya *et al.*[122] demonstrated that delaminated $Ti_3C_2T_x$ nanosheets, comprising few or single layers, exhibit significantly superior electrochemical performance in supercapacitor applications compared to their multilayer counterparts. This enhancement is primarily due to the increased surface area and improved ion accessibility in the delaminated structures, which facilitate faster charge storage and transfer. The intrinsic electronic properties of MXenes are further influenced by their surface chemistry, especially the functional groups that terminate their surfaces, typically –O, –OH, or –F, introduced during the etching process. These terminations play a pivotal role in tuning the electronic band structure of MXenes. For example, density functional theory (DFT) calculations have shown that oxygen-terminated $Ti_3C_2T_x$ exhibits higher electrical conductivity than its fluorine-terminated variant, which tends to be semiconducting or even insulating in some cases.[121] The surface terminations also modulate the work function of MXenes, with reported values for $Ti_3C_2T_x$ ranging from 1.6 to 4.6 eV depending on the terminating species. This variability has crucial implications for MXene integration in electronic and optoelectronic devices, where precise control over energy levels is necessary.

Regarding charge-transport mechanisms, the electronic conductivity of MXene nanosheets generally shows a temperature-dependent trend. At room temperature, MXenes typically exhibit metallic behavior, with conductivity decreasing with increasing temperature a hallmark of metallic conduction. However, at lower temperatures, conduction may proceed *via* a hopping mechanism, particularly in samples with significant structural defects or interflake resistance. Ling *et al.*[7] reported that temperature-dependent conductivity measurements of $Ti_3C_2T_x$ support this dual conduction model, confirming its metallic nature at ambient conditions. Furthermore, while the charge-carrier mobility in MXenes is generally lower than that of graphene, typically ranging from 1 to 10 cm2/V s, it remains sufficient for most practical applications in sensors, supercapacitors, and flexible electronics. This mobility, combined with high conductivity and tunable surface chemistry, enables MXenes to bridge the gap between metallic and semiconducting behavior, providing an adaptable platform for diverse electronic applications. Thus, the electronic properties of MXene nanosheets are intrinsically linked to their structural features, surface terminations, and dimensionality, all of which must be carefully engineered to meet the demands of specific high-performance applications.

MXenes exhibit unique plasmonic properties arising from their high free-carrier concentration and intrinsic metallic behavior, setting them apart from other 2D materials. These plasmonic features are primarily characterized by localized surface plasmon resonance (LSPR), a collective oscillation of conduction electrons induced by incident light, which can be finely tuned through structural and chemical modifications. In MXene nanosheets, particularly $Ti_3C_2T_x$, the LSPR can be modulated across a broad spectral range from the near-infrared (NIR) to the visible region by tailoring parameters such as flake size, thickness, aspect ratio, and surface functionalization. The ability to adjust LSPR *via* surface chemistry is especially important, as terminal groups such as –O, –OH, and –F influence the electron density and dielectric environment around the nanosheets, thereby affecting the plasmonic resonance frequency. Experimental studies by Dillon *et al.*[59] provided strong evidence of the plasmonic behavior of $Ti_3C_2T_x$ nanosheets, demonstrating pronounced optical absorption in the near-infrared region. This absorption behavior is attributed to the LSPR effect and indicates their ability to convert light into heat efficiently. Consequently, these properties make MXenes particularly attractive for photothermal applications, including cancer therapy, where localized heating is crucial, as well as in solar energy harvesting systems, where light-to-heat conversion can be effectively utilized. Moreover, the strong NIR absorption combined with the high surface area and tunable surface chemistry renders MXene nanosheets highly suitable for optical sensing applications. Changes in the local refractive index or the chemical environment at the MXene surface can shift the plasmon resonance, providing a sensitive platform for detecting analytes such as gases, biomolecules, or ions. The flat, flexible structure of MXene also allows easy integration into optical devices and substrates, further broadening their applicability. Compared to noble metal-based plasmonic materials such as gold or silver, MXenes offer additional advantages, including lower cost, higher mechanical flexibility, and chemical versatility due to their rich surface chemistry.

Furthermore, their compatibility with aqueous processing and solution-phase synthesis enhances their scalability for large-area or wearable optoelectronic applications. Thus, the plasmonic behavior of MXenes is not only a fundamental property linked to their electronic structure but also a versatile tool that can be leveraged in a wide array of advanced technologies, from photothermal therapy and bioimaging to environmental and biomedical sensing. Their tunable LSPR, high photothermal conversion efficiency, and chemical functionality collectively position MXenes as a promising new class of plasmonic nanomaterials with capabilities extending well beyond conventional metallic systems.

8. Mechanical strength and stability

MXene nanosheets exhibit outstanding mechanical properties, making them highly suitable for a wide range of structural, flexible, and wearable device applications. Their mechanical robustness stems from strong covalent bonding between transition metals (such as titanium) and carbon or nitrogen atoms in the layered carbide or nitride backbone, which underpins their high stiffness and strength. Theoretical studies based on molecular dynamics simulations have predicted remarkably high mechanical parameters for these materials, with Ti_3C_2 exhibiting a Young's modulus of up to 502 GPa and a tensile strength approaching 15 Gpa.[123] However, experimental assessments of MXene mechanical behavior, particularly using nanoindentation techniques, typically yield lower values than

those predicted by theory. For instance, $Ti_3C_2T_x$ films where T_x denotes surface terminations such as –O, –OH, or –F demonstrated Young's modulus values of approximately 330 ± 30 GPa using AFM nanoindentation.[124]

These reductions are primarily due to imperfections in real materials, such as vacancies, grain boundaries, disordered terminations, and interlayer water molecules, which can act as stress concentrators or weaken interatomic interactions. Additionally, surface terminations alter the electronic structure and bonding environment at nanosheet surfaces, leading to deviations from ideal stiffness values. The number of MXene layers also plays a significant role in determining mechanical performance; single-layer MXenes generally exhibit higher stiffness and strength than multilayer stacks, primarily because multilayer assemblies experience weaker van der Waals interlayer forces and potential layer sliding under load. This interlayer interaction, although beneficial for certain applications such as lubrication, introduces mechanical compliance, reducing overall rigidity. Importantly, the exceptional mechanical behavior of MXenes is maintained under bending and stretching, making them particularly attractive for integration into flexible electronics, structural nanocomposites, strain sensors, and reinforcement agents in polymer matrices. Their ability to retain mechanical integrity while undergoing deformation ensures reliable performance in dynamic environments. Moreover, the mechanical properties of MXenes can be further engineered through doping, surface functionalization, or hybridization with other 2D materials, thereby enabling the design of materials with customized mechanical responses. Overall, the combination of high intrinsic stiffness, tunability *via* surface chemistry, and superior mechanical performance positions MXenes as a top-tier candidate among mechanically resilient nanomaterials.

From a practical standpoint, the mechanical properties most relevant to MXene's core application domains flexible energy storage films, conformal EMI shields, and wearable biosensor substrates, are bending resilience, tensile flexibility, and resistance to delamination under cyclic strain. MXene films retain structural integrity through repeated flexure cycles, and their inherent brittleness under large strains is effectively mitigated by polymer composite design and layer-by-layer architectures, which distribute stress and suppress failure, strategies already employed in the EMI shielding composites discussed in Section 9.2.

One of the primary challenges limiting the practical applications of MXenes is their environmental instability, particularly their susceptibility to oxidation in the presence of moisture and oxygen. Experimental investigations have demonstrated that $Ti_3C_2T_x$ gradually oxidizes under ambient conditions, leading to the formation of titanium dioxide (TiO_2) and other oxidation products that significantly degrade its electrical conductivity and mechanical integrity.[125] This oxidative degradation compromises the long-term performance of MXene-based devices, especially in energy storage, sensing, and flexible electronics. The oxidation mechanism primarily involves the diffusion of oxygen molecules through the surface termination layers, followed by their interaction with the underlying titanium carbide framework. This leads to the progressive formation of amorphous or crystalline oxide layers, which disrupt the conductive Ti–C network. The oxidation rate is highly dependent on several environmental and structural factors, including temperature, relative humidity, pH of the surrounding medium, and the density of surface defects or edge sites, which serve as preferential nucleation centers for oxidation.

To enhance the oxidative stability of MXenes, several strategies have been proposed. Surface passivation using antioxidants or protective molecular coatings can delay oxygen ingress and inhibit surface reactions. Encapsulation techniques, such as polymer coating or embedding in inert matrices, have also been employed to provide physical barriers against environmental exposure. Additionally, the development of alternative MXene compositions, such as carbonitride MXenes (*e.g.*, Ti_3CNT_x) and ordered double-transition-metal MXenes (*e.g.*, $Mo_2TiC_2T_x$), continues to be explored to potentially enhance chemical stability and tailor properties. These approaches collectively aim to extend the operational lifespan of MXene-based materials and broaden their applicability in real-world environments.[126]

9. Key applications and performance of MXene nanosheet

The unique combination of metallic conductivity, hydrophilicity, and tunable surface chemistry makes MXene nanosheets exceptionally versatile materials for a wide range of applications. Their 2D structure offers a high surface area and efficient ion transport pathways, while their excellent mechanical properties and processability facilitate the development of flexible and scalable devices.[127] This section examines the key applications where MXenes have demonstrated outstanding performance and commercial potential.

9.1. Energy storage (supercapacitors, batteries)

Supercapacitors, also known as electrochemical capacitors, store energy *via* electrical double-layer capacitance and pseudocapacitance mechanisms. Electrochemical studies have reported specific capacitances for $Ti_3C_2T_x$-based electrodes ranging from 200 to 900 F g^{-1}, with performance strongly dependent on electrolyte composition, concentration, and operating conditions.[122]

The synergistic contribution of electrical double-layer capacitance and pseudocapacitance endows MXene-based electrodes with high power density and excellent rate capability. In addition, the intrinsically hydrophilic surface chemistry of MXenes promotes efficient electrolyte wettability and the formation of stable electrode–electrolyte interfaces, which are essential for fast ion transport and electrochemical stability. Sarangapani *et al.*[128] demonstrated that electrochemical capacitors derive their large capacitance from "a combination of the double-layer capacitance and pseudocapacitance associated with surface redox-type reactions. Fleischmann *et al.*[129] confirmed that combining "pseudo-capacitive nanomaterials"

with advanced nanostructured designs achieves both high energy and power density.

Regarding hydrophilic surface chemistry, Soni *et al.*[130] provided concrete evidence: superhydrophilic PANI electrodes delivered 1335 F g^{-1} gravimetric capacitance and 1217 F g^{-1} at high current density (50 A g^{-1}), demonstrating excellent rate capability. Yoo *et al.*[131] showed hydrophilic carbon electrodes exhibited "low ion-transfer resistance" and superior capacitance (58 F cm^{-3}). Zhao *et al.*[132] confirmed that surface wettability optimization improves energy density while maintaining power density performance.

MXenes can be easily dispersed in water and functionalized. Strategies to further enhance MXene supercapacitor performance include increasing the interlayer spacing *via* intercalation with organic molecules or ions, thereby improving ion diffusion kinetics. Additionally, composite electrodes combining MXenes with conductive polymers, carbon nanotubes, or graphene have been developed to enhance conductivity, mechanical flexibility, and electrochemical stability in a synergistic manner.

In rechargeable batteries, MXenes serve as attractive electrode materials due to their high conductivity and ability to accommodate ion intercalation. MXenes have been explored as anodes and cathodes in lithium-ion, sodium-ion, and potassium-ion batteries, among others. Their layered structure enables reversible intercalation of various alkali metal ions with minimal volume expansion, thereby reducing mechanical degradation and enhancing cycle life.

$Ti_3C_2T_x$ anodes, for example, demonstrate high-capacity retention and fast charge–discharge rates, benefiting from a pseudocapacitive charge-storage mechanism in addition to traditional intercalation processes. A key challenge in flexible supercapacitors is balancing the trade-off between high capacity and rapid charging, which is typically limited by sluggish ion diffusion and storage dynamics within densely packed electrode structures. A hydrogen-rich graphene (GDY)-$Ti_3C_2T_x$ electrode featuring tunable interlayer spacing, abundant active sites, and extensive nanoscale charge-storage channels. Notably, the GDY-$Ti_3C_2T_x$ (12.6 wt%) electrode delivers an impressive volumetric capacitance of 2296 F cm^{-3} at 1 A cm^{-3}. It maintains fast-charging performance with 1262 F cm^{-3} at 50 A cm^{-3}, enabled by shortened ion-transport pathways, enhanced diffusion rates, and improved electrolyte mass transport. Furthermore, an all-solid-state supercapacitor (ASSC) based on this architecture achieves a high volumetric energy density of 65.6 mWh cm^{-3}, alongside excellent long-term cycling stability, mechanical deformability, and high capacitance retention under harsh operating conditions. Density functional theory (DFT) calculations and molecular dynamics simulations reveal that the GDY-$Ti_3C_2T_x$ heterostructure exhibits rapid electronic responsiveness due to stronger H^+ electrostatic attraction, reduced migration resistance, and accelerated intercalation-driven pseudocapacitance kinetics. *In situ* X-ray diffraction further confirms that a robust Ti–O–C-bridged organic–inorganic heterostructure withstands repeated high-current charge/discharge cycles. This state-of-the-art ASSC demonstrates multifunctional performance and holds significant promise for efficient energy delivery in practical flexible-electronics applications.[133] Surface functional groups on MXenes play a critical role in modulating ion diffusion barriers and electrochemical activity, influencing capacity and cycling performance. Research has shown that modifying MXene surface terminations or doping with heteroatoms can improve ion storage capacity and electrode stability.

Moreover, MXenes have been used as conductive additives or protective coatings on battery electrodes, enhancing electronic conductivity and mitigating electrode pulverization. Their high mechanical flexibility and chemical stability also make them suitable for flexible and wearable energy storage devices.

Despite their promising attributes, MXenes face challenges, including oxidative instability under ambient conditions, which can degrade their electrochemical performance.[134] Research efforts are ongoing to improve their environmental stability through surface passivation, encapsulation, and the synthesis of more oxidation-resistant MXene compositions.

Future developments in MXene-based energy storage devices will focus on optimizing surface chemistry, controlling interlayer spacing, and integrating MXenes into hybrid architectures. Such advances are expected further to improve capacity, rate performance, and cycling stability, paving the way for MXene-enabled supercapacitors and batteries that meet the demands of high-performance, flexible, and sustainable energy storage technologies.

MXenes have emerged as one of the most promising materials for supercapacitor applications due to their unique combination of high electrical conductivity, hydrophilic surface, and pseudocapacitive behavior.[118] The energy storage mechanism in MXene-based supercapacitors involves both electrical double-layer capacitance (EDLC) and pseudocapacitance, with the latter contributing significantly to the overall capacitance through rapid redox reactions at the surface terminations.

$Ti_3C_2T_x$, the most extensively studied MXene, has demonstrated exceptional supercapacitor performance in aqueous electrolytes. Ghidiu *et al.*[135] reported a volumetric capacitance of 900 F cm^{-3} for rolled $Ti_3C_2T_x$ clay films in 1 M H_2SO_4 at a scan rate of 2 mV s^{-1}, which is among the highest values reported for any material. The high performance is attributed to the combination of pseudocapacitive charge storage and the ability to accommodate hydrated protons between the MXene layers. The charge storage mechanism involves proton intercalation coupled with electron transfer, as described by the reaction:

$$Ti_3C_2T_x + xH^+ + xe^- \leftrightarrow H_xTi_3C_2T_x$$

The excellent performance of MXenes in organic electrolytes has opened new possibilities for high-voltage supercapacitors. Dall'Agnese *et al.*[136] investigated the performance of pseudocapacitive materials that store charge through fast surface or near-surface redox reactions are key contenders for achieving high-energy-density electrochemical capacitors. MXenes recently discovered two-dimensional transition-metal carbides exhibit excellent capacitance in aqueous electrolytes, but their

narrow operational potential window restricts both energy and power density. In this study, we investigate the electrochemical behavior of Ti_3C_2 MXene in 1 M 1-ethyl-3-methylimidazolium bis(trifluoromethylsulfonyl)imide (EMITFSI) dissolved in acetonitrile, along with two other commonly used organic electrolytes. Clay, delaminated, and Ti_3C_2/carbon-nanotube composite electrodes were examined to elucidate how electrode architecture and composition influence performance. Capacitances of 85 F g^{-1} and 245 F cm^{-3} at 2 mV s^{-1} were achieved, accompanied by strong rate capability and good cycling stability. *In situ* X-ray diffraction reveals the intercalation of the large EMI^+ cation into MXene layers, which enhances capacitance but may also act as the rate-limiting step governing device performance.

In ionic liquid electrolytes, MXenes demonstrate exceptional stability and performance. Lin *et al.*[137] reported that $Ti_3C_2T_x$ in 1-ethyl-3-methylimidazolium bis(trifluoromethylsulfonyl)imide (EMI-TFSI) ionic liquid achieved a capacitance of 70 F g^{-1} with a large voltage window of 3 V and excellent cycling stability over 10 000 cycles. The use of ionic liquids also enables operation at elevated temperatures, expanding the application range of MXene supercapacitors. Zhao *et al.*[138] reported that $Ti_3C_2T_x$/CNT sandwich-like composites achieved a volumetric capacitance of 390 F cm^{-3} with improved cycling stability. Boota *et al.*[139] demonstrated that $Ti_3C_2T_x$/polypyrrole composites exhibit enhanced gravimetric capacitance (416 F g^{-1}) and excellent rate capability. The conducting polymer provides additional pseudocapacitive sites while preventing MXene oxidation, thereby improving long-term stability.

MXenes have attracted considerable interest as active materials for rechargeable batteries due to their outstanding electrical conductivity, structural tunability, rich surface chemistry, and 2D layered architecture. These characteristics make them suitable for use in various battery systems, including lithium-ion batteries (LIBs), sodium-ion batteries (SIBs), potassium-ion batteries (PIBs), and emerging systems such as magnesium-ion and zinc-ion batteries.

MXenes have shown great promise as anode materials for lithium-ion batteries due to their high theoretical capacity and excellent conductivity. The lithium storage mechanism involves intercalation into the interlayer spaces of MXene structures, with additional storage occurring through conversion reactions with surface terminations.

Naguib *et al.*[140] first demonstrated the use of $Ti_3C_2T_x$ as a lithium-ion battery anode, achieving a reversible capacity of 225 mAh g^{-1} with excellent rate capability. The lithium storage occurs through the intercalation mechanism:

$$Ti_3C_2T_x + xLi^+ + xe^- \leftrightarrow Li_xTi_3C_2T_x$$

Theoretical calculations by Xie *et al.*[141] predicted that bare Ti_3C_2 (without surface terminations) could achieve a theoretical capacity of 320 mAh g^{-1}, which is comparable to graphite anodes but with superior rate capability due to the metallic conductivity of MXenes.

Recent advances have focused on optimizing surface chemistry and developing MXene composites to improve battery performance. Come *et al.*[142] demonstrated that $Ti_3C_2T_x$/graphene composites exhibit enhanced capacity (410 mAh g^{-1}) and cycling stability, with the graphene layers preventing MXene restacking and providing additional lithium storage sites.

The development of beyond-lithium battery technologies has driven interest in MXenes for sodium-ion and potassium-ion batteries. The larger interlayer spacing in MXenes compared to graphite makes them particularly suitable for accommodating larger alkali ions. Kajiyama *et al.*[143] investigated $Ti_3C_2T_x$ as a sodium-ion battery anode and achieved a reversible capacity of 200 mAh g^{-1}, accompanied by excellent rate performance. The sodium storage mechanism involves intercalation with minimal volume change, leading to excellent cycling stability over 300 cycles. The larger size of sodium ions compared to lithium ions results in stronger interactions with MXene surfaces, providing stable electrochemical performance.

For potassium-ion batteries, Zhao *et al.*[138] demonstrated that $Ti_3C_2T_x$ can accommodate potassium ions with a reversible capacity of 192 mAh g^{-1}. Despite potassium ions' large size, the flexible interlayer spacing in MXenes enables efficient ion transport and storage, making them promising candidates for large-scale energy storage applications.

MXenes have also been explored as electrocatalysts and conductive supports in metal-air batteries. Their high conductivity and tunable surface chemistry make them excellent platforms for catalyst development. Shabana *et al.*[144] demonstrated that $Ti_3C_2T_x$-supported platinum nanoparticles exhibit enhanced oxygen reduction reaction (ORR) activity compared to conventional carbon supports, attributed to the strong metal-support interactions and high conductivity of MXenes.

In lithium-air batteries, MXene-based air electrodes have shown improved performance due to their high surface area and excellent conductivity. The hydrophilic surface of MXenes also facilitates the wetting of electrolytes, improving ion transport and reducing polarization losses. In sodium-ion battery applications, MXenes demonstrate remarkable versatility as electrode materials (Fig. 6). The Ex-Ti_3C_2 MXene variant shows excellent compatibility with sodium ions, as evidenced by the intercalation of Na^+ ions between the MXene layers. The system also accommodates various electrolyte components, including ClO_4^- anions and PDDA-BP (poly(diallyldimethylammonium chloride)-biphenyl) additives. This combination creates an optimal environment for sodium storage, with the MXene layers providing both high conductivity and structural stability. The rapid ion-diffusion pathways enable fast charging and discharging, making these materials promising candidates for next-generation sodium-ion batteries.

The application of MXenes in lithium-sulfur batteries represents another significant advancement in energy storage technology. Fig. 6 illustrates how MXenes can effectively interact with sulfur-containing species, demonstrating compatibility with lithium, sulfur, hydrogen, oxygen, titanium, and carbon atoms. The discharge process involves complex electrochemical reactions, during which the MXene framework stabilizes intermediate polysulfide species and facilitates

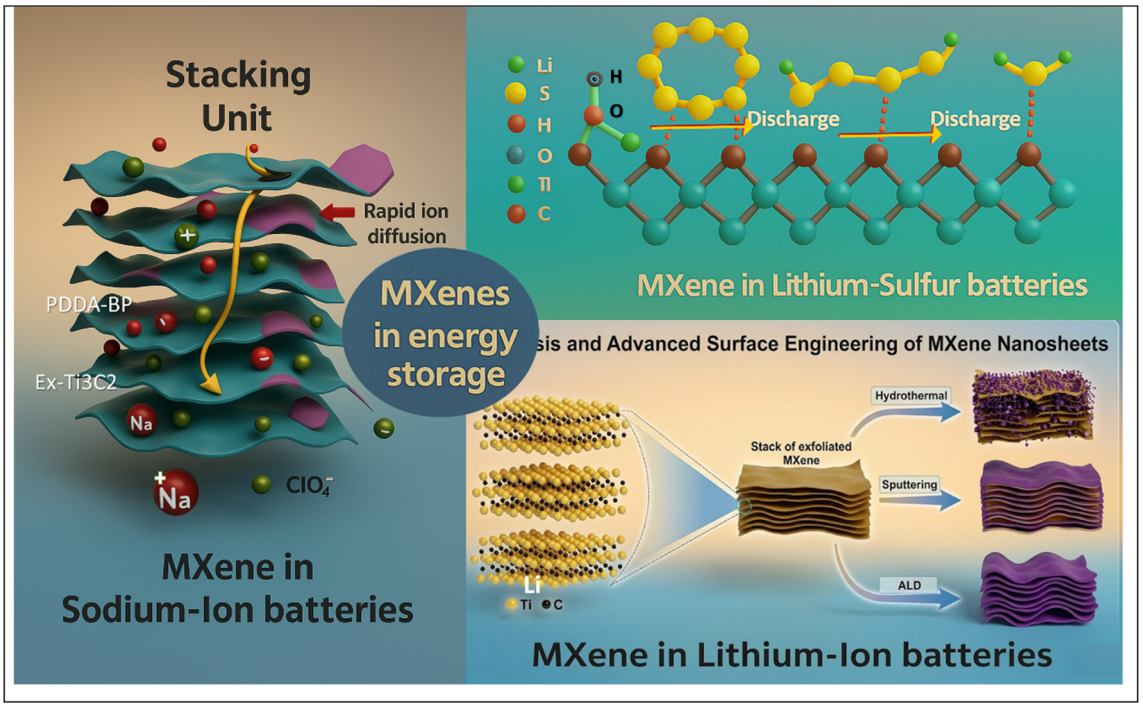

Fig. 6 Schematic representation of MXene interactions with sulfur-containing species, highlighting their compatibility with lithium, sulfur, hydrogen, oxygen, titanium, and carbon atoms, this figure has been reproduced from ref. 145 with permission from Oxford University Press, copyright 2025.

efficient lithium-ion transport. This application is significant because lithium-sulfur batteries offer high theoretical energy densities, and MXenes help address traditional challenges such as polysulfide dissolution and poor conductivity.

For lithium-ion battery applications, MXenes can be processed through various methods to optimize their performance. Fig. 6 illustrates how stacks of exfoliated MXene sheets can be further modified through different processing techniques. Hydrothermal treatment creates materials with enhanced structural properties, while sputtering methods can be used to make thin-film electrodes with controlled thickness and uniformity. Atomic layer deposition (ALD) is another processing route that enables precise control over surface modifications and the creation of composite materials. These various processing methods enable tailoring MXene properties to specific lithium-ion battery requirements, including capacity, rate capability, and cycle-life optimization.

9.2. Electromagnetic interference EMI shielding

MXenes have emerged as highly promising materials for electromagnetic interference (EMI) shielding owing to their exceptional electrical conductivity, low density, and tunable surface chemistry.[146] The same metallic conductivity that underpins their electrochemical charge storage in supercapacitors and batteries (Section 9.1) also governs their interaction with electromagnetic waves, establishing a direct mechanistic link between the two application domains. Their intrinsic metallic conductivity enables efficient reflection of incident electromagnetic radiation, while their two-dimensional layered architecture promotes multiple internal reflections and enhanced absorption, resulting in high shielding effectiveness. In addition, surface terminations such as –OH, –F, and –O not only improve dispersion and processability in composite systems but also contribute to interfacial polarization and dielectric loss, further strengthening EMI attenuation mechanisms. As a result, free-standing $Ti_3C_2T_x$ films have demonstrated EMI shielding effectiveness values exceeding 50–60 dB at thicknesses below 50 μm, surpassing the performance of many conventional metal-based shielding materials. Moreover, MXene-based composites incorporating polymers or secondary conductive fillers, such as carbon nanotubes and graphene, have enabled the development of lightweight, flexible, and mechanically robust shielding materials, making them attractive for applications in wearable electronics, aerospace systems, and telecommunications devices. Despite these advantages, challenges related to environmental stability, scalable synthesis, and interfacial compatibility with polymer matrices remain. Addressing these limitations through surface passivation strategies, microstructural optimization, and environmentally benign fabrication routes will be essential for the practical deployment of MXene-based EMI shielding technologies.[147]

A fundamental methodological limitation in the MXene EMI shielding literature lies in the direct comparison of absolute shielding effectiveness (SE) values without appropriate normalization for sample thickness, areal density, or measurement frequency band. Shielding effectiveness is inherently dependent on conductor thickness (*via* skin-depth effects), material density (reflecting the mass of conductive

material per unit area), and operating frequency, as eddy-current generation and dielectric losses vary strongly with frequency. Consequently, absolute SE values reported without these contextual parameters provide limited insight and may lead to misleading comparisons across studies.

For instance, MXene aerogel foams reporting shielding effectiveness values approaching 90 dB often achieve such performance primarily through multiple internal reflections within thick, low-density porous networks.

Han *et al.*[148] reported $Ti_3C_2T_x$ aerogels reaching 70.5 dB at 1 mm thickness with a specific SE of 8818.2 dB cm^3 g^{-1}, while Sambyal *et al.*[149] achieved 103.9 dB at 3 mm in X-band.

In contrast, dense $Ti_3C_2T_x$ films exhibit shielding effectiveness values of approximately 50 dB operate predominantly through surface reflection and single-pass absorption at substantially lower thicknesses. Shahzad *et al.*[67] demonstrated 92 dB for 45 μm films but only >50 dB for 2.5 μm films. Normalized metrics prove essential for meaningful comparison. Liu *et al.*[150] reported Ka-band performance with SSE/t of 81 408 dB cm^2 g^{-1} for ultrathin films, while Yun *et al.*[151] achieved 3.89 $\times$ 10^6 dB cm^2 g^{-1} for 55 nm films. Mannafi *et al.*[152] explicitly categorizes architectures by mechanism (reflection-dominated *versus* absorption-dominated), supporting the need for frequency-band and mechanism-specific evaluation.

The EMI shielding effectiveness of a material is its ability to attenuate electromagnetic waves and is usually quantified in decibels (dB). The total shielding effectiveness (SE_{total}) comprises three main components: reflection (SE_R), absorption (SE_A), and multiple internal reflections (SE_M). The interplay between these mechanisms determines the overall EMI shielding performance of MXene-based materials.

9.2.1 Reflection (SE_R). Reflection is often the dominant shielding mechanism in highly conductive materials. When electromagnetic waves encounter the surface of a conductive MXene film, a significant portion of the incident radiation is reflected due to impedance mismatch between the free space and the material surface. MXenes, such as $Ti_3C_2T_x$, exhibit high metallic conductivity (10^3–10^4 S cm^{-1}), which provides a high density of free charge carriers that interact with the oscillating electric field of the incident wave, causing it to be reflected.[67] The extent of reflection is primarily governed by the surface conductivity and dielectric constant of the material, both of which are inherently high in MXenes. Additionally, the stacked lamellar structure of MXene films further contributes to interface polarization, enhancing their reflective capabilities.

9.2.2 Absorption (SE_A). While reflection helps deflect electromagnetic waves, absorption plays a crucial role in energy dissipation. In MXenes, absorbed electromagnetic radiation is converted into thermal energy through ohmic, eddy-current, and dielectric losses. The high conductivity of MXenes enables significant joule heating when electromagnetic waves induce current flow, resulting in energy dissipation. Eddy current losses become more pronounced at high frequencies, particularly in thicker films where loops of induced currents form in response to alternating magnetic fields. Moreover, surface terminations (–OH, –F, –O) introduce dipoles that interact with the electromagnetic field, leading to dielectric relaxation losses that consume electromagnetic energy and dissipate it as heat.[153] These dielectric losses increase the imaginary part of the permittivity, enhancing the absorption of electromagnetic radiation. Film thickness, frequency of the incident radiation, and interlayer spacing play critical roles in determining absorption efficiency. For instance, studies have shown that thicker MXene films (*e.g.*, 20–50 μm) can achieve absorption-dominated shielding, contributing over 80% of the total EMI SE.[138] Moreover, tuning the interlayer spacing *via* chemical or physical methods, such as intercalation with metal ions or polymer chains, enhances internal dipole polarization and provides multiple energy dissipation pathways, thereby improving absorption.

9.2.3 Multiple internal Reflections (SE_M). In thin or porous MXene films, incident waves can penetrate deeper into the material and undergo multiple reflections between internal surfaces and interlayer gaps before being completely absorbed or transmitted. These repeated reflections, referred to as numerous internal reflections (SE_M), effectively increase the electromagnetic path length within the material, giving more opportunities for energy dissipation through dielectric and ohmic losses. Although SE_M is typically significant in thin films (<8 μm), its contribution diminishes in thicker films, where most of the energy is already absorbed or reflected.[154]

Enhancing surface roughness or introducing hierarchical structures in MXene films (*e.g.*, porous architectures, foam scaffolds, or 3D networks) can amplify internal reflections, thereby improving overall EMI shielding. For example, hybrid MXene foams or aerogels produced by freeze-drying or 3D printing exhibit highly porous, interconnected structures that promote multiple scattering and attenuation of electromagnetic waves.[155]

While pure MXene films show excellent EMI shielding properties, their performance can be further enhanced by forming composites with conductive polymers (*e.g.*, polyaniline, PEDOT:PSS), carbon-based nanomaterials (*e.g.*, graphene, CNTs), or magnetic fillers (*e.g.*, Fe_3O_4, Ni nanoparticles). These hybrid systems combine different shielding mechanisms for instance, dielectric polarization from polymers and magnetic loss from nanoparticles resulting in synergistic improvements in EMI SE.

Fig. 7 illustrates various innovative strategies for integrating MXene into textile-based, flexible electronic devices. In Fig. 7a, MXene nanosheets are spray-deposited onto plain-woven cotton fabric, forming a vertically aligned conductive network that enables multifunctional textile performance such as Joule heating, EMI shielding, and strain sensing without sacrificing breathability or mechanical flexibility.[67,156] Fig. 7b illustrates a stretchable and fatigue-resistant antenna/shielding device fabricated by layering $Ti_3C_2T_x$ MXene and single-walled carbon nanotubes (SWNT) on pleated latex. This composite structure maintains conductivity under extreme elongation (up to 800% strain) and repeated mechanical stress, making it ideal for wearable wireless applications.[157] In Fig. 7c, a hybrid fabric is created by *in situ* polymerization of polypyrrole on MXene sheets, followed by a silicone coating on a PET fabric. This method significantly enhances the hydrophobicity and long-term stability of MXene against oxidation in humid

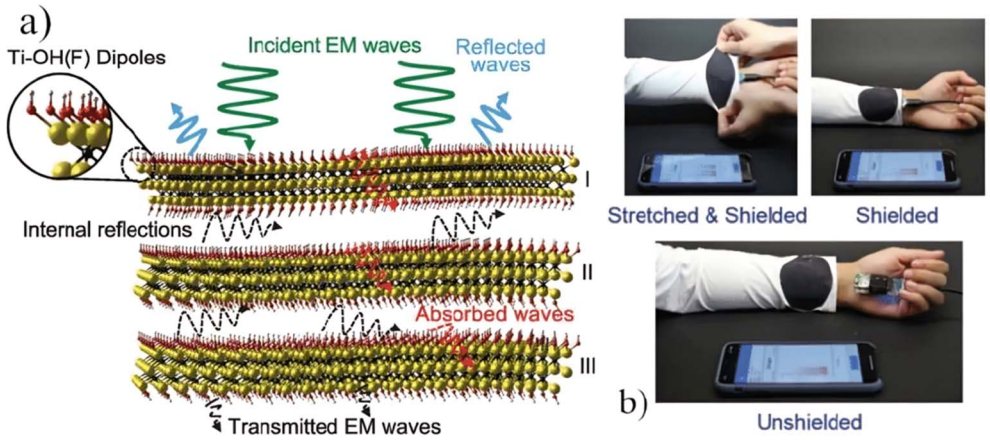

Fig. 7 (a) Schematic illustration of the electromagnetic interference (EMI) shielding mechanism of MXene-based materials, highlighting the roles of incident wave reflection, multiple internal reflections, absorption, and attenuation within the layered conductive structure enriched with Ti–OH(F) surface dipoles. The multilayered MXene architecture effectively suppresses transmitted electromagnetic waves through synergistic reflection and absorption pathways. (b) Photographic demonstration of the flexible S-MXene shielding material under different operating conditions, including stretched and shielded, normal shielded, and unshielded states, confirming its effective EMI shielding capability and mechanical adaptability for wearable electronic applications, this figure has been adapted from ref. 85 with permission from iopscience, copyright 2021.

environments, while maintaining excellent EMI shielding and Joule heating capabilities.[158] Collectively, these innovations showcase the potential of MXene-integrated textiles in the development of next-generation smart clothing and wearable electronics.

Experimental studies have demonstrated the exceptional EMI shielding performance of MXenes. Shahzad *et al.*[67] reported that Materials that combine high electrical conductivity, mechanical flexibility, and strong EMI shielding in minimal thickness are highly sought after, particularly when they can be readily processed into films. Two-dimensional metal carbides and nitrides, known as MXenes, uniquely integrate metallic conductivity with hydrophilic surfaces. In this work, we demonstrate the exceptional EMI shielding capabilities of several MXenes and their polymer composites. A 45 μm-thick $Ti_3C_2T_x$ film achieves an EMI shielding effectiveness of 92 dB (and >50 dB for a 2.5 μm film), representing the highest performance reported for synthetic materials of comparable thickness. This remarkable shielding arises from the excellent electrical conductivity of $Ti_3C_2T_x$ films (4600 S cm^{-1}) and the multiple internal reflections generated within the stacked MXene flakes in free-standing films.

The exceptional mechanical flexibility and facile processability of MXenes and their composites enable conformal coating of substrates with complex geometries while maintaining high EMI shielding performance. The total electromagnetic interference shielding effectiveness can be expressed as:

$$SE_{total} = SE_R + SE_A + SE_M$$

The structure–property relationships in MXene films are crucial for optimizing EMI shielding performance. The layered morphology of MXenes, arising from their 2D nature, enables effective nanosheet stacking, creating dense yet flexible films with high electrical conductivity and multiple interfaces for wave attenuation.[159] Additionally, the interlayer spacing can be tailored by introducing intercalants (*e.g.*, organic molecules, metal cations, or water), thereby further enhancing multiple internal reflections and dielectric losses. The incorporation of polymers, carbon nanotubes, or other 2D materials (*e.g.*, graphene or boron nitride) can also be used to form MXene-based composites that maintain, or even improve, shielding effectiveness while adding mechanical robustness, thermal stability, and corrosion resistance.

Another essential aspect of MXene EMI shielding is its tunability *via* surface chemistry. The surface of MXenes is typically terminated with functional groups such as –O, –OH, and –F, which are introduced during the selective etching of the A layer (typically Al) in MAX phases using HF or other etchants. These terminations affect not only the surface conductivity but also the interaction with matrix materials in composites.[160] For instance, modifying MXene surfaces *via* post-treatment or functionalization can enhance their dispersibility, compatibility, and interfacial bonding with polymer matrices, thereby improving film uniformity and performance.

Moreover, MXenes exhibit frequency-dependent shielding behavior, with higher shielding effectiveness in the GHz range due to enhanced dielectric polarization and increased conductive losses. Studies have reported that adjusting the thickness and layering of MXene films enables control over the frequency range in which optimal EMI shielding occurs.[161] This is advantageous for designing materials tailored to specific applications, such as military communications, radar systems, and consumer electronics, which operate at different frequency bands.

Importantly, MXenes also offer scalability and processability, as they can be fabricated into films *via* solution-based processes such as vacuum-assisted filtration, spray coating, spin coating, and inkjet printing. This allows for low-cost, scalable

manufacturing of shielding components, including coatings for enclosures, substrates for circuit boards, and flexible films for wearable electronics.[162]

In addition to standalone films, MXene-based hybrid and composite structures have been developed to further enhance EMI shielding performance. For example, combining $Ti_3C_2T_x$ with conductive polymers like polyaniline (PANI) or polypyrrole (PPy), or incorporating carbon nanotubes (CNTs), results in synergistic interactions that enhance conductivity, mechanical integrity, and interface-induced losses.[163] These hybrid architectures not only achieve high SE but also offer tunability of mechanical and thermal properties suitable for harsh environments.

Layer-by-layer (LbL) assembled multilayer composites represent another powerful approach for constructing ordered structures with alternating conductive and insulating layers. These configurations create interfacial polarization and reflection effects, substantially increasing EMI shielding. MXene-based composites are also being explored for dynamic EMI shielding, where tunability in shielding effectiveness is achieved by external stimuli such as electric fields, temperature, or mechanical deformation. For example, electrically tunable EMI shields based on MXene-hydrogel composites have shown promise in applications such as smart windows and reconfigurable electronics. By swelling or shrinking the hydrogel matrix, the interlayer spacing of MXene sheets can be modulated, thereby altering the conductivity and EMI SE. These smart materials can switch between high- and low-shielding states on demand, enabling their use in adaptive electromagnetic environments.

A critical factor in all MXene composites is the maintenance of oxidation stability, as MXenes tend to degrade in humid or oxidative environments. Strategies such as surface passivation, encapsulation within polymer matrices, or the introduction of antioxidative agents (*e.g.*, tannic acid, boron nitride) are actively pursued to prolong the lifespan of MXene-based EMI shields. Furthermore, hybridization with graphene oxide or carbon-based coatings has been shown to act as physical barriers to oxygen and water, further enhancing environmental stability.

In conclusion, MXene-based composite and hybrid materials present a versatile and powerful platform for developing high-performance EMI shielding materials. By leveraging their intrinsic properties high conductivity, tunable surface chemistry, and 2D structure along with synergistic interactions from polymers, carbonaceous materials, metals, and porous architectures, these systems achieve exceptional shielding performance with mechanical robustness and multifunctionality. Continued advancements in composite engineering, surface modification, and fabrication techniques are expected to unlock the full potential of MXenes in emerging electromagnetic shielding applications across flexible electronics, the aerospace, telecommunications, and defense sectors.

Fig. 8 illustrates multiple strategies for designing biopolymer-based EMI shielding membranes with enhanced mechanical flexibility and performance. In Fig. 8A, Zhou *et al.*[164] developed a multilayer alternating cellulose nanofiber (CNF)

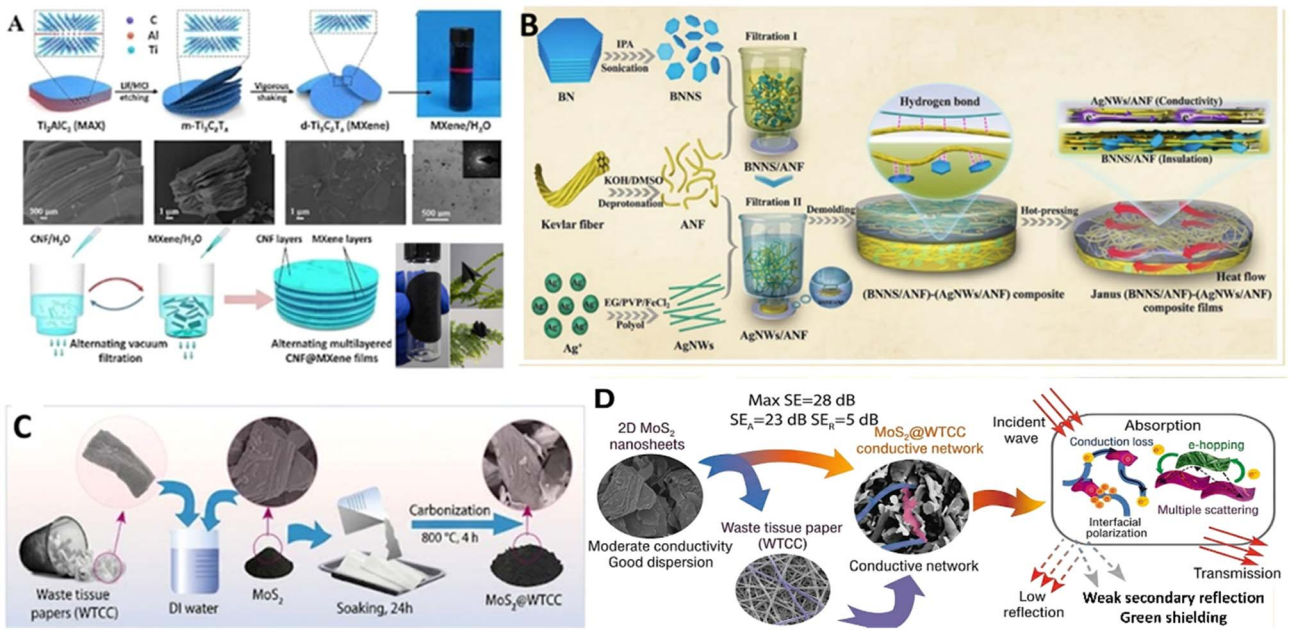

Fig. 8 Schematic diagrams of cellulose-based EMI shielding membranes: (A) CNF@MXene multilayer composite with alternating CNF/MXene structure for mechanical enhancement, this figure has been adapted ref. 164 with permission from American Chemical Society, copyright 2020. (B) Janus-structured thermal-conductive membrane (BNNS/ANF-AgNWs/ANF) with dual functional layers, this figure has been adapted from ref. 165 with permission from Springer, copyright 2022. (C) MoS_2-integrated waste cellulose paper (MoS_2@WTCC) with enhanced absorption shielding *via* interfacial polarization, this figure has been adapted from ref. 166 with permission from Elsevier, copyright 2022. (D) Conductive network formation from MoS_2-cellulose hybrids enhances shielding while preserving green material integrity, this figure has been reproduced from ref. 166 with permission from Elsevier, copyright 2022.

and MXene membrane (CNF@MXene) *via* vacuum-assisted filtration. The CNF layers serve as mechanical reinforcements, preventing nano-zigzag crack propagation in the MXene layers and enabling superior flexibility, with more than 1000 folding cycles without failure. Fig. 8B shows a Janus-structured membrane composed of boron nitride nanosheets (BNNS) and aramid nanofibers (ANFs), reported by Han *et al.*[165] This structure combines thermal conductivity and EMI shielding in a multifunctional platform with distinct conductive and insulating layers. In Fig. 8C, Uddin *et al.*[166] integrated low-conductivity MoS_2 nanosheets into carbonized waste cellulose paper, creating MoS_2@WTCC composites. The MoS_2 sheets act as interfacial polarization centers and bridges for conductive networks, improving dielectric loss and lowering reflectance for green EMI shielding. Fig. 8D illustrates how the unique MoS_2-cellulose hybrid structure enhances both shielding performance and sustainability by minimizing the use of conductive components.

Despite the superior shielding characteristics of pure MXene films, their mechanical brittleness and difficulty in large-scale processing necessitate the development of composite systems that preserve shielding efficiency while improving flexibility, durability, and manufacturability. Composite and hybrid systems, particularly those combining MXenes with polymers, offer a compelling solution. By embedding MXene flakes into flexible polymer matrices, researchers have engineered materials that combine MXene's electrical conductivity with the toughness, processability, and lightweight nature of polymers. A notable example involves MXene/poly(vinyl alcohol) (PVA) composites, which have demonstrated a shielding effectiveness of 66 dB at 10 vol% $Ti_3C_2T_x$ content.[167] The strong hydrogen bonding between the hydroxyl-rich PVA chains and the terminal functional groups on MXene surfaces (such as –OH, –O, and –F) ensures excellent dispersion and interfacial adhesion, resulting in homogenous composites with superior mechanical properties and reliable EMI performance. The uniform dispersion of MXene nanosheets within the polymer matrix facilitates the formation of continuous conductive networks, which are critical for efficient reflection and absorption of incidental electromagnetic waves.

These composites also offer enhanced long-term stability and oxidation resistance, a notable advantage over pure MXene films, which are prone to degradation under ambient conditions. Functionalizing MXenes with organic or inorganic species further enhances their compatibility with polymer matrices, preven/ting layer restacking and maintaining a high surface area and effective conductive pathways. For instance, surface modification using alkyl chains improves their dispersion in non-polar polymers. At the same time, decorating with metal nanoparticles can introduce additional dielectric interfaces, further boosting EMI attenuation through interfacial polarization.

Beyond synthetic polymers, research has also explored incorporating MXenes into natural or biodegradable matrices, such as cellulose, chitosan, and gelatin, to create eco-friendly shielding materials suitable for biomedical or disposable electronics. The combination of biocompatibility, processability, and high shielding efficiency makes these materials attractive for emerging applications in sustainable and wearable electronics.

Recent advancements in processing techniques, such as spray coating, vacuum-assisted filtration, 3D printing, and electrospinning, have enabled the scalable fabrication of MXene/polymer composites with customizable thickness, porosity, and mechanical properties. These techniques not only simplify the manufacturing of complex geometries but also enable the creation of multilayer or gradient structures that can optimize shielding effectiveness across broad frequency ranges. Additionally, layer-by-layer (LbL) assembly of alternating MXene and polymer layers has been demonstrated to yield tunable EMI shielding films with a controllable architecture and high anisotropy, enabling directional shielding properties required in specialized devices. Fig. 9 comprehensively illustrates the various techniques used to fabricate MXene-based devices, including stamping, inkjet printing, and 3D printing. In Fig. 9A, different stamping molds were fabricated through 3D printing, allowing the formation of specific patterns tailored to various applications, such as interdigitated electrodes for energy storage devices. These molds enable precise control over the pattern geometry, which is critical for device performance. In Fig. 9B, the synthesis and use of $Ti_3C_2T_x$ and Ti_3CNT_x MXenes as stamping inks are presented. These inks are essential for creating high-quality, conductive patterns on flexible substrates. Fig. 9C illustrates the stamping process, where MXene ink is applied to the mold surface and then pressed onto a flexible PET substrate. This process enables the direct transfer of conductive patterns with high fidelity and precise control over thickness and uniformity.

Fig. 9D shows the performance results of the stamped MXene-based micro-supercapacitors, which exhibit a high areal capacitance of 61 mF cm^{-2}. This demonstrates the viability of the stamping method for producing flexible, high-performance energy storage devices. In addition to stamping, Fig. 9E–I highlights the preparation and use of MXene inks for inkjet and 3D printing. Fig. 9E illustrates how MXene inks can be formulated in various solvents suitable for extrusion and inkjet printing, offering flexibility in processing methods. Fig. 9F provides a schematic of the 3D printing process, starting from the synthesis of large-flake, few-layer $Ti_3C_2T_x$ MXenes, which are ideal for maintaining the desired mechanical and electrical properties during fabrication.

The rheological properties of MXene inks are shown in Fig. 9G, where tuning these properties ensures suitability for extrusion printing processes by adjusting the ink's viscosity and flow behavior. Fig. 9H illustrates the 3D printing process, in which MXene inks are deposited layer by layer to construct the desired structures for energy devices. Finally, Fig. 9I depicts the freeze-drying step applied after printing to stabilize the 3D structures, resulting in free-standing MXene architectures suitable for constructing energy storage devices. Overall, Fig. 9 highlights the versatility of MXene inks in multiple fabrication techniques, enabling the scalable production of flexible, wearable, and high-performance electronic and energy devices.

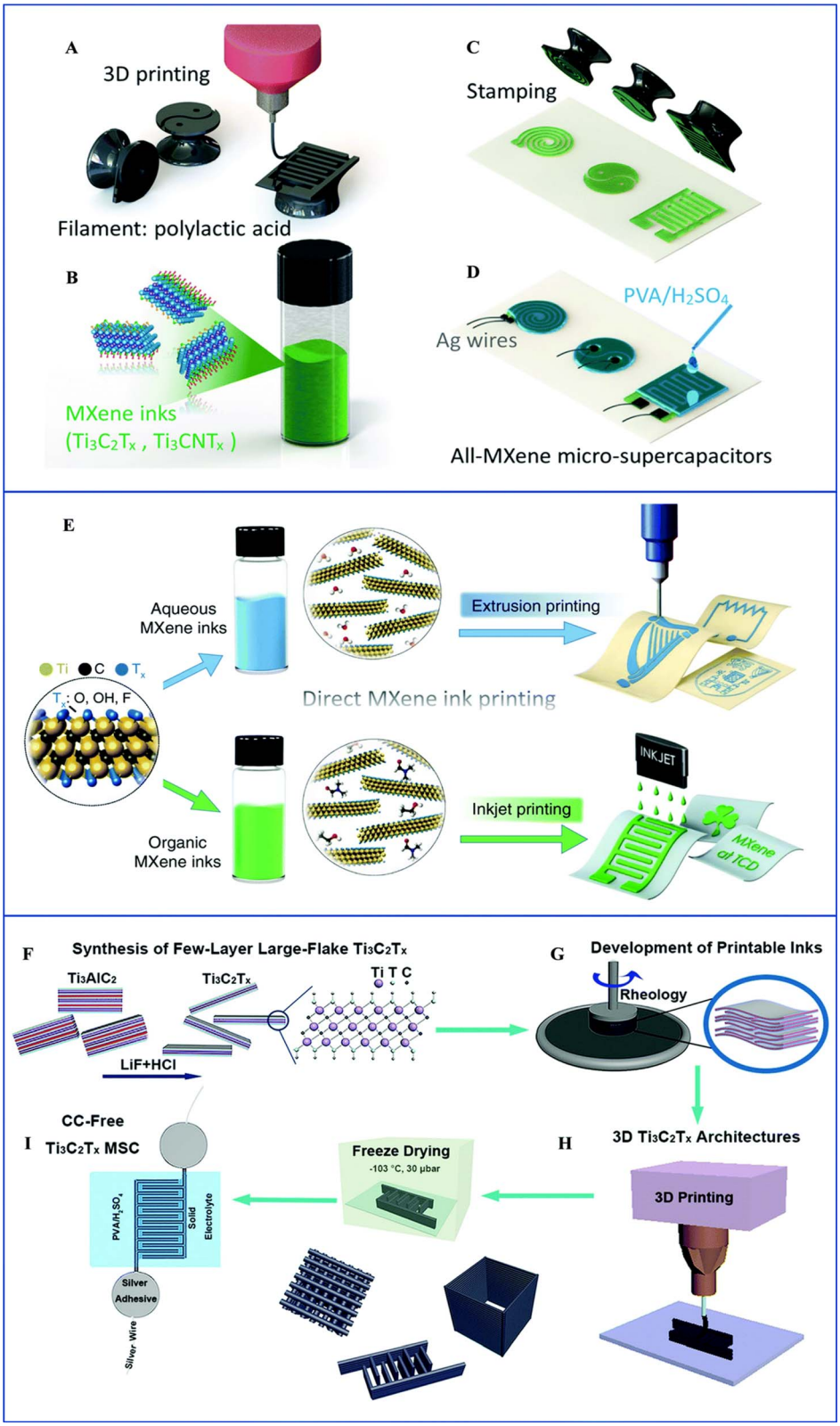

Fig. 9 Stamping, inkjet, and 3D printing of MXene-based devices. (A) 3D-printed molds with different shapes are designed for stamping applications. (B) Synthesis of $Ti_3C_2T_x$ and Ti_3CNT_x MXenes used as functional inks for stamping. (C) Stamping process where MXene ink is applied to the mold and transferred to a flexible PET substrate. (D) Interdigitated micro-supercapacitors fabricated *via* stamping, demonstrating high areal capacitance performance. (E) Preparation of MXene inks in various solvents, suitable for extrusion and inkjet printing. (F) Schematic of the 3D printing process starting from the synthesis of large-flake, few-layer $Ti_3C_2T_x$ MXene. (G) Rheological tuning of MXene inks to optimize their flow properties for extrusion printing. (H) 3D printing of MXene ink layer-by-layer to build complex structures for energy storage devices. (I) Freeze-drying of printed MXene structures to form stable, free-standing architectures. These methods highlight the versatility of MXene inks for fabricating flexible, wearable, and high-performance energy storage and sensing devices, this figure has been adapted from ref. 168 with permission from Royal Society of Chemistry, copyright 2022.

In conclusion, MXene-based composites represent a highly versatile and effective class of EMI shielding materials. Their outstanding intrinsic conductivity, tunable surface functionalities, and ease of integration into flexible and multifunctional composites make them ideal candidates for lightweight, high-performance shielding solutions in next-generation electronics. By carefully controlling structure, composition, and processing, it is possible to design MXene-based shielding systems that outperform traditional materials, meet stringent mechanical and thermal requirements, and support emerging applications such as flexible displays, wireless communication devices, and implantable electronics.

To address limitations such as brittleness and restacking tendencies of pristine MXene films, researchers have developed a variety of MXene-based composites that incorporate polymers and carbonaceous materials to enhance their mechanical flexibility, structural stability, and processability while maintaining high EMI shielding performance. One prominent approach is to integrate MXenes with polymer matrices. These MXene/polymer composites benefit from MXenes' intrinsic conductivity and polymers' lightweight, flexible nature. Fig. 10 expands on the use of porous and hybrid cellulose structures for high-performance shielding. Fig. 10a shows a novel "egg-carton" design proposed by inserting carbonized cellulose microspheres (CCM) into MXene layers, yielding a CCM@void@MXene composite with improved graded conductivity and effective microwave attenuation.[169] Fig. 10b describes two methods for engineering porous carbon nanotube (CNT)/cellulose composites: one *via* matrix embedding and the other *via* CNT interfacing. These lightweight, high-modulus composites achieve shielding levels up to 40 dB.[170] Fig. 10c presents bacterial cellulose (BC) hybrid membranes (BC–SiO_2–TiO_2/Ag),[171] capable of UV-induced self-sterilization, recyclability, and flexible EMI shielding. Finally, Fig. 10d shows that introducing 1.4 nm cellulose nanofibers enables both physical and chemical crosslinking of MXene nanosheets, forming ultra-thin PC-MXene membranes with improved electrical pathways and reduced inter-nanosheet insulation gaps.[172] These studies underscore the vast potential of cellulose as a green, effective scaffold for multifunctional EMI shielding.

9.3. Biomedical applications (drug delivery, biosensing)

Before discussing individual biomedical applications, it is important to establish a critical baseline on MXene biocompatibility, as this governs clinical translatability. While early studies reported favorable cell viability for $Ti_3C_2T_x$ at moderate doses, biocompatibility is not an intrinsic property of MXenes but is highly context-dependent. Key modulating factors include: (i) surface termination chemistry, where –OH-rich surfaces are associated with greater reactive oxygen species (ROS) generation than –F-terminated counterparts; (ii) lateral flake size and aspect ratio, with smaller flakes showing higher internalization rates and potential lysosomal disruption; (iii) functionalization strategy, where PEG or chitosan coatings

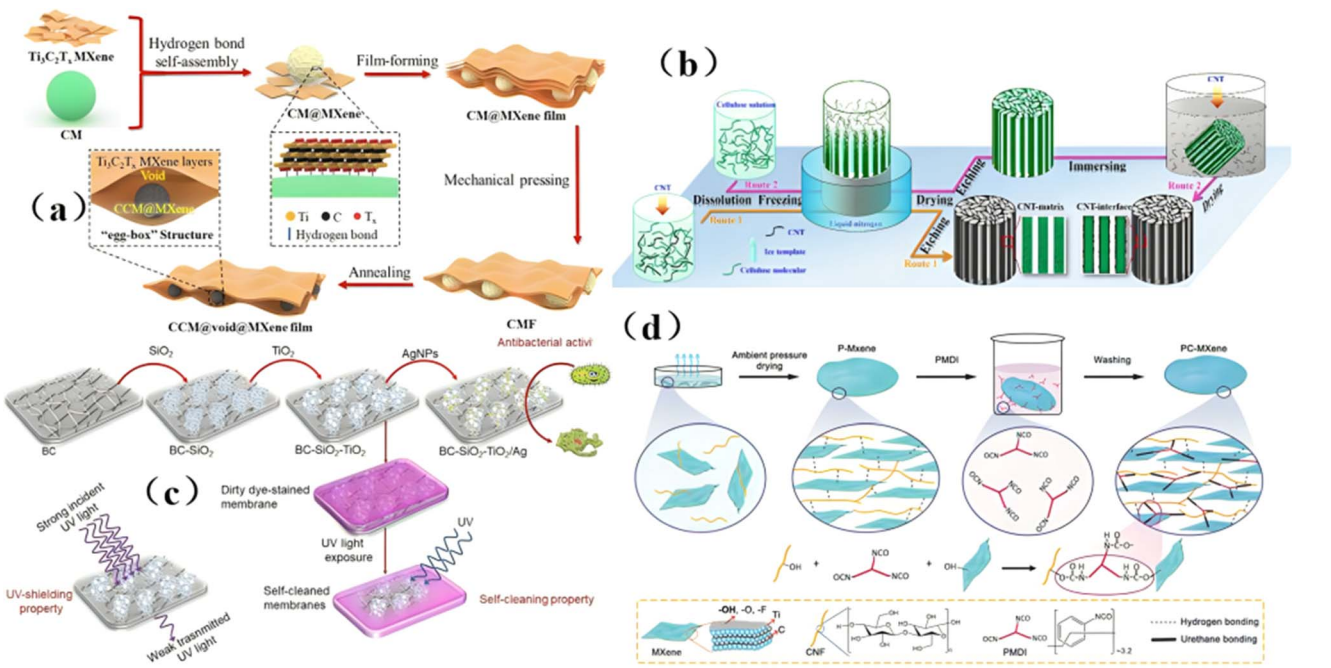

Fig. 10 Cellulose-derived porous and hybrid composites for EMI shielding: (a) egg-carton structured CCM@void@MXene composite for improved graded absorption and reflection control, this figure has been adapted from ref. 169 with permission from Elsevier, copyright 2021. (b) CNT/cellulose composites with tunable porosity and CNT distribution for mechanical robustness and high shielding, this figure has been reproduced from ref. 170 with permission from American Chemical Society, copyright 2018. (c) Flexible and UV-disinfectable bacterial cellulose hybrid membranes (BC–SiO_2–TiO_2/Ag), this figure has been adapted from ref. 171 with permission from Elsevier, copyright 2021. (d) PC-MXene membranes formed by dual cross-linking of 1.4 nm cellulose nanofibers for enhanced flexibility and electrical conductivity, this figure has been adapted from ref. 172 with permission from Wiley, copyright 2021.

substantially reduce cytotoxicity and extend circulation time *in vivo*; and (iv) dose and exposure duration, as viability thresholds differ markedly across cell lines and target organs. Critically, *in vivo* long-term biodistribution and clearance data remain sparse for most MXene compositions, and dose-dependent inflammatory responses have been documented in several studies. These limitations must be borne in mind when evaluating the performance results reported throughout this section.

MXenes serve as efficient platforms for drug delivery, biosensing, imaging, and other therapeutic interventions. In drug delivery, the high surface area of MXene nanosheets enables a significant drug-loading capacity. At the same time, the presence of functional groups provides multiple anchoring sites for chemical conjugation with therapeutic molecules or targeting ligands. Among the most studied MXenes, $Ti_3C_2T_x$ has demonstrated considerable potential. Zhang *et al.*[173] reported that functionalized $Ti_3C_2T_x$ nanosheets can be loaded with anticancer drugs, such as doxorubicin (DOX), and exhibit pH-controlled release behavior, making them ideal for tumor-specific drug delivery. The acidic tumor microenvironment promotes drug release from the MXene carrier, thereby reducing off-target effects. Furthermore, MXenes exhibit good biocompatibility and low cytotoxicity when appropriately functionalized or coated with biocompatible polymers such as polyethylene glycol (PEG) or chitosan. Moreover, the photothermal properties of MXenes can be harnessed for combinational therapy.

When exposed to near-infrared (NIR) light, MXenes convert light into heat, inducing localized hyperthermia that can kill cancer cells while simultaneously triggering drug release, thereby providing a synergistic photothermal-chemotherapy approach. In biosensing, MXenes' superior electrical conductivity and large specific surface area make them excellent candidates for the fabrication of electrochemical and optical biosensors. Their metallic conductivity facilitates fast electron transfer, which is vital for the sensitivity and speed of electrochemical detection. The abundant terminal functional groups enable the immobilization of biomolecules, such as antibodies, aptamers, enzymes, and DNA probes, ensuring the selective recognition of target analytes. The 2D layered structure of MXenes facilitates efficient immobilization and probe molecule accessibility, thereby enhancing the biosensor's sensitivity and stability. MXenes also exhibit good compatibility with other nanomaterials such as gold nanoparticles, carbon nanotubes, and quantum dots, enabling the construction of hybrid biosensors with enhanced signal amplification. In optical biosensing, MXenes' strong absorbance in the NIR and visible regions makes them suitable for developing surface-enhanced Raman spectroscopy (SERS) and fluorescence-based sensors. Huang *et al.*[174] reported a Ti_3C_2-based fluorescence biosensor for glucose detection by immobilizing glucose oxidase on the MXene surface. The system demonstrated high sensitivity and selectivity, with a stable response over multiple cycles, highlighting the potential of MXenes for continuous glucose monitoring in diabetic patients.

Furthermore, MXenes are being explored for real-time health monitoring and wearable biosensors. Their flexibility, mechanical strength, and ability to form conductive networks make them ideal for integration into flexible substrates. Beyond biosensing and drug delivery, MXenes are also investigated for their antibacterial activity, gene delivery, and bioimaging capabilities. The sharp edges of MXene nanosheets, combined with their oxidative potential, disrupt bacterial membranes and generate reactive oxygen species (ROS), providing inherent antibacterial properties without the need for antibiotics. In gene delivery, Chen *et al.*[175] reported that $Ti_3C_2T_x$ nanosheets could effectively complex with metals, metal oxides, metal sulfides, organic frameworks, photosensitizers, and other components. Researchers have produced composite structures capable of exerting synergistic physical, chemical, and photodynamic antibacterial effects. These synergies not only enhance bacterial inactivation efficiency but also broaden the applicability of $Ti_3C_2T_x$-based materials across diverse environments where conventional antibiotics perform poorly.

Importantly, the biodegradability and long-term biosafety of MXenes remain key considerations for their clinical translation. Although initial studies have shown favorable biocompatibility, especially when coated or functionalized, the potential accumulation and degradation products of MXenes in biological systems must be thoroughly evaluated. Strategies such as surface engineering, biodegradable functional coatings, and size optimization are being employed to address these concerns. Additionally, their multifunctionality makes them excellent candidates for theranostics integrated platforms combining diagnostics and therapy. For example, by integrating drug delivery, photothermal therapy, and imaging functionalities (*e.g.*, photoacoustic or magnetic resonance imaging), MXenes can serve as versatile agents for precision medicine. Liu *et al.*[176] demonstrated this by fabricating a $Ti_3C_2T_x$-based nanoplatform Ti_3C_2 MXene is an emerging two-dimensional material that demonstrates a range of unique properties, including an excellent photothermal effect, highlighting its potential for multimodal tumor therapy. This field urgently requires effective materials. In this study, ultrathin Ti_3C_2 MXene nanosheets (~100 nm) were synthesized by introducing Al^{3+} ions to prevent aluminum loss and subsequently employed as a photothermal and photodynamic agent for cancer treatment. The resulting nanosheets exhibited remarkable optical and therapeutic properties, including a high mass extinction coefficient (28.6 $L\,g^{-1}\,cm^{-1}$ at 808 nm), a superior photothermal conversion efficiency (~58.3%), and efficient generation of singlet oxygen ($^1O_2$) under 808 nm laser irradiation. Building upon these nanosheets, a multifunctional nanoplatform (Ti_3C_2-DOX) was developed *via* layer-by-layer surface modification with doxorubicin (DOX) and hyaluronic acid (HA). Both *in vitro* and *in vivo* studies demonstrated that Ti_3C_2-DOX possesses enhanced biocompatibility, tumor-targeted accumulation, and stimuli-responsive drug release, achieving effective cancer cell eradication and tumor tissue destruction through a synergistic combination of photothermal, photodynamic, and chemotherapy modalities.

In conclusion, MXenes are versatile and highly functional materials for biomedical applications, particularly in drug delivery and biosensing. Their tunable surface chemistry, high

conductivity, biocompatibility, and multifunctionality enable them to address multiple challenges in targeted therapy and disease diagnostics. Ongoing research focused on improving their stability, targeting specificity, and biosafety will further advance their applicability in clinical settings, paving the way for next-generation nanomedicine platforms.

The limited efficacy and potential off-target toxicity of nanotherapeutic drugs remain significant challenges in liver cancer treatment. To address these issues, a novel targeted therapy approach utilizing a multifunctional nanocomposite, DOX/Ti_3C_2/PDA/PEG-FA, was developed by Lv *et al.*[177] for combined photothermal/chemotherapy (PTT/CHT) tumor treatment. The folic acid (FA)-modified nanomaterial facilitated specific targeting of folate receptor-overexpressing liver tumor cells, ensuring enhanced accumulation of the drug within the tumor site. Upon near-infrared (NIR) laser irradiation, the Ti_3C_2/PDA core exhibited efficient photothermal conversion, rapidly elevating tumor-region temperatures while simultaneously triggering controlled DOX release *via* photothermal and acidic stimulation, thereby promoting chemotherapy. *In vitro* results demonstrated that the DOX/Ti_3C_2/PDA/PEG-FA nanocomposites effectively inhibited the proliferation of HepG2 cells. Moreover, *in vivo* studies in the HepG2 xenograft mouse model showed a significant reduction in the tumor volume and complete tumor ablation with minimal side effects, indicating the high efficiency and low toxicity of the targeted PTT/CHT combination therapy. This study introduces a novel DOX/Ti_3C_2/PDA/PEG-FA nanoplatform that paves the way for targeted cancer therapy *via* a synergistic mechanism, significantly improving therapeutic efficacy against liver cancer while concurrently reducing systemic adverse effects.

Fig. 11 highlights the design and biomedical application of multifunctional scaffolds (HPEM) integrating polydopamine-coated $Ti_3C_2T_x$ MXene nanosheets (MXene@PDA) within a polymeric matrix of oxidized hyaluronic acid (HCHO) and branched poly(glycerol-ethyleneimine) (PGE), tailored for treating methicillin-resistant *Staphylococcus aureus* (MRSA)-infected wounds.[178] In Fig. 11A, the schematic illustrates the fabrication of HPEM scaffolds, where each component serves a functional purpose: MXene@PDA provides electrical conductivity and broad-spectrum antibacterial activity. At the same time, PGE and HCHO confer self-healing and bioadhesive properties through dynamic Schiff-base linkages. The TEM image in Fig. 11B confirms the core–shell structure of MXene@PDA. In contrast, the SEM image in Fig. 11C reveals the porous architecture of the resulting scaffold, critical for tissue integration and nutrient exchange. Fig. 11D and E demonstrate the material's self-healing capability, showing scaffold reformation after mechanical disruption. Fig. 11F presents antibacterial efficiency results, with HPEM scaffolds achieving over 99% bacterial reduction against *E. coli*, *S. aureus*, and MRSA, outperforming untreated controls. Fig. 11G shows the scaffold's rapid hemostatic activity, reducing total blood loss in a mouse liver injury model compared to untreated samples ($p < 0.05$, $p < 0.01$, "n" $= 3$). Most notably, Fig. 11H shows accelerated wound healing in a murine MRSA infection model, with 96.31% wound closure observed after 14 days. Histological analyses revealed enhanced granulation tissue formation, angiogenesis, and upregulation of α-SMA and CD31, accompanied by collagen deposition, confirming that the multifunctional HPEM scaffold not only combats infection but also significantly promotes skin regeneration.[178]

The unique physicochemical properties of MXenes, especially their high specific surface area, tunable surface chemistry, excellent hydrophilicity, and inherent biocompatibility, make them promising nanoplatforms for drug delivery applications. The negatively charged, hydrophilic surfaces of MXene nanosheets facilitate efficient drug loading through multiple interactions, including electrostatic forces, hydrogen bonding, and π–π stacking, enabling high drug payload capacity and controllable release profiles.

A study by Lin *et al.*[179] demonstrated the potential of $Ti_3C_2T_x$ MXene nanosheets as cancer therapy. A two-step exfoliation of MAX-phase Ti_3AlC_2 using combined HF etching and TPAOH intercalation. Remarkably, these Ti_3C_2 nanosheets demonstrated high photothermal conversion efficiency and were effective *in vitro* and *in vivo* for tumor ablation, achieved through both intravenous administration of soybean phospholipid-modified nanosheets and localized intratumoral implantation of a phase-changeable PLGA/Ti_3C_2 organic–inorganic hybrid. This study highlights the significant potential of Ti_3C_2 MXenes as novel ceramic photothermal agents for cancer therapy. It is expected to stimulate further exploration of MXene-based ceramic biomaterials for broader biomedical applications.

Beyond passive targeting enabled by the enhanced permeability and retention (EPR) effect, MXenes have been functionalized with specific targeting ligands to actively direct drug-loaded nanosheets to cancer cells, thereby minimizing side effects and improving therapeutic efficacy. Surface functionalization commonly involves covalently conjugating biomolecules, such as antibodies, peptides, aptamers, or small-molecule ligands, to the abundant –OH or –COOH terminations on MXene surfaces *via* amide bond formation or other chemical linkages.

An outstanding feature of MXenes is their intrinsic stimulus-responsiveness, especially their excellent photothermal conversion efficiency, owing to strong absorption in the near-infrared (NIR) region. This property enables the design of smart drug delivery systems that respond to external triggers such as light, pH, or temperature to achieve on-demand drug release with high spatial and temporal control.

In this regard, Lu *et al.*[180] engineered a photothermal-responsive drug delivery platform by loading DOX onto $Ti_3C_2T_x$ nanosheets. Upon exposure to 808 nm NIR laser irradiation, the MXene nanosheets converted light into localized heat, rapidly increasing the temperature and inducing drug release. Remarkably, approximately 90% of the loaded DOX was released within just 10 minutes of NIR exposure. This synergistic effect combines chemotherapy and photothermal therapy (PTT) to enhance tumor cell killing. Hyperthermia generated by MXenes sensitizes cancer cells to DOX, thereby increasing therapeutic efficacy. Additionally, the on-demand release

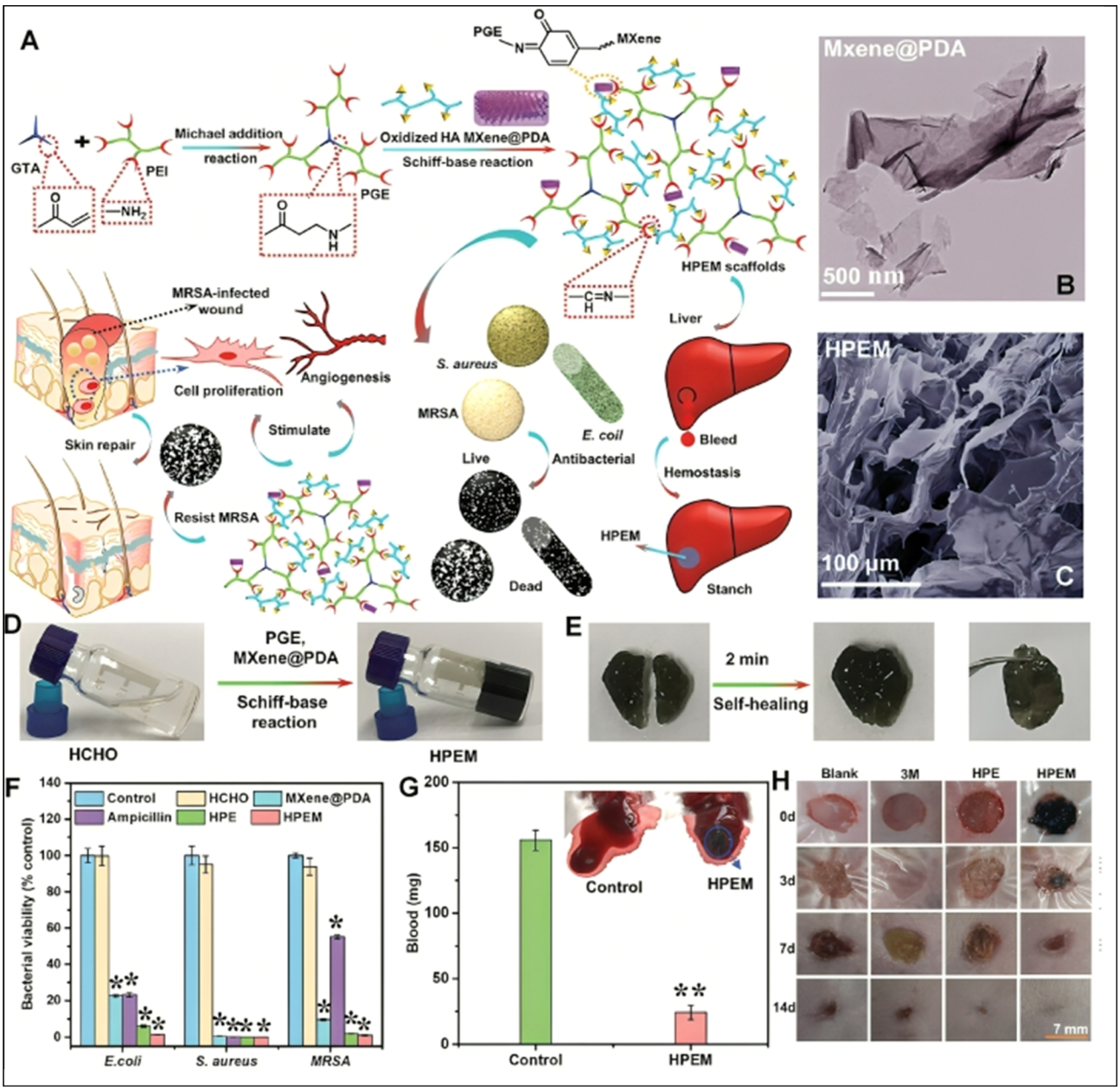

Fig. 11 (A) Schematic illustration of multifunctional HPEM scaffold fabrication for MRSA-infected wound healing. The scaffold comprises polydopamine-coated $Ti_3C_2T_x$ MXene (MXene@PDA), oxidized hyaluronic acid (HCHO), and poly(glycerol-ethyleneimine) (PGE). (B) TEM image of MXene@PDA nanosheets. (C) SEM image of porous HPEM scaffold. (D and E) Photographs showing the scaffold's formation and self-healing capability *via* Schiff-base chemistry. (F) Bacterial viability assay against *E. coli*, *S. aureus*, and *MRSA*, indicating >99% antibacterial efficacy. (G) Hemostatic evaluation: blood loss and liver injury closure after 60 seconds of treatment ($p < 0.05$, $p < 0.01$, "n" = 3). (H) Photographic progression of MRSA-infected wound healing in mice treated with HPEM scaffolds over 14 days, showing 96.31% closure, this figure has been adapted from ref. 178 with permission from American Chemical Society, copyright 2021.

capability reduces systemic toxicity and minimizes drug wastage.

Furthermore, MXenes' pH-responsiveness synergizes with photothermal triggering. At acidic tumor sites, the weakened interaction between DOX and MXene surface terminations facilitates drug release, while NIR irradiation provides an external stimulus to accelerate the process. Such dual stimuli-responsiveness makes MXene-based nanocarriers highly efficient for precision cancer therapy.

The biomedical application of MXenes mandates careful evaluation of their cytotoxicity and biocompatibility. Studies have shown that pristine MXenes exhibit low toxicity; however, surface modification with biocompatible polymers, such as PEG, chitosan, or polyvinyl alcohol (PVA), can further reduce the immune response and improve circulation time *in vivo*. Functionalized MXenes typically exhibit minimal hemolysis and good cellular viability in various cell lines, rendering them suitable for systemic administration.

Long-term safety and biodegradation remain active areas of research. Since MXenes are relatively new, understanding their *in vivo* metabolism and potential accumulation is critical before clinical translation. Initial studies indicate that MXenes can degrade under physiological conditions, with functionalization and nanosheet size influencing biodistribution and clearance pathways.[181]

Electrochemical biosensors based on MXenes are among the most widely explored applications. The high conductivity and surface area of MXenes enable amplification of electrochemical signals, which is critical for the detection of low-abundance biomolecules. For instance, Zhang *et al.*[182] developed a dual-mode electrochemical immunosensor that was constructed using Ti_3C_2 MXene-anchored CuAu-LDH two-dimensional hydroxide heterojunctions for sensitive biomarker detection. Layered double hydroxides (LDHs) possess large surface areas, high chemical stability, tunable metal compositions, and interchangeable anions; however, their insulating nature limits catalytic performance. To overcome this, Ti_3C_2 MXenes were introduced, providing two-dimensional layers with high specific surface area and excellent electrical conductivity. The abundant surface functional groups of Ti_3C_2 MXenes facilitate metal ion anchoring and LDH nucleation, while their conductivity enhances electron transfer between Cu^{2+} and Cu^{+}. The resulting immunosensor exhibited strong square-wave voltammetry (SWV) signals and high electrocatalytic activity for H_2O_2 redox reactions, thereby improving the sensitivity of amperometric (*i–t*) detection. The CEA immunosensor demonstrated a wide linear range (0.0001–80 ng mL^{-1}) and ultralow detection limits (SWV: 33.6 fg mL; *i–t*: 45.4 fg mL^{-1}, S/N = 3), confirming its excellent analytical capability and potential for highly sensitive biomarker detection.

Nucleic acid detection is another critical application area. MXene-based sensors have been successfully used to detect DNA and microRNA (miRNA) with high sensitivity. The large surface area and flexible functionalization of MXenes facilitate the immobilization of single-stranded DNA (ssDNA) probes that hybridize selectively with complementary target sequences. For example, Dehnoei *et al.*[183] fabricated a novel and efficient method for detecting miRNA-191 using $Ti_3C_2(OH)_2$ MXene nanosheets. MicroRNAs serve as important biomarkers for various cancers and other medical conditions, emphasizing the need for reliable detection strategies. An enzyme-free, simple, rapid, and label-free fluorescence probe was developed by combining ssDNA-modified silver nanoclusters (ssDNA-AgNCs) with $Ti_3C_2(OH)_2$ MXene nanosheets to create a turn-on detection platform. The unique properties of MXenes, including high sensitivity, stability, and reproducibility in biological fluids, enhance assay performance. In this system, ssDNA-AgNCs interact with the MXene surface *via* π–π stacking, leading to adsorption and fluorescence quenching. Upon the introduction of the target miRNA-191, a probe/target complex forms, releasing the ssDNA-AgNCs and restoring their fluorescence, which is then used to quantify miRNA-191. The platform exhibited excellent analytical performance, with a linear detection range of 0.1–100 nM and a limit of detection of ~65 pM. The developed bioassay is advantageous due to its simplicity, cost-effectiveness, rapid response, and high stability and specificity. Notably, this work represents the first application of a $Ti_3C_2(OH)_2$ MXene-based optical biosensor for miRNA detection, and the assay demonstrated satisfactory performance in real sample analysis.

In addition to electrochemical biosensors, MXenes have been employed in optical biosensing. Their strong absorption in the near-infrared (NIR) region and plasmonic-like behavior facilitate the development of surface-enhanced Raman scattering (SERS) sensors and fluorescence-based biosensors. Zhu *et al.*[184] reported developed an effective and selective fluorescent turn-on nanosensor for glucose detection by combining Ti_3C_2 nanosheets with red-emitting carbon dots (RCDs). The fluorescence of RCDs was efficiently quenched (>96%) by Ti_3C_2 nanosheets through the inner-filter effect (IFE). In the presence of H_2O_2, the quenched fluorescence was markedly restored, as Ti_3C_2 nanosheets were oxidized into $Ti(OH)_4$ by H_2O_2. Leveraging H_2O_2 generated from glucose oxidation catalyzed by glucose oxidase, the nanosensor was further applied for glucose monitoring. Under optimal conditions, a linear correlation between the restored fluorescence intensity and glucose concentration was achieved over the range of 0.1–20 mM, with a detection limit of 50 μM (S/N = 3). The nanosensor exhibited excellent selectivity for glucose and demonstrated reliable performance in biological fluids, providing a promising platform for glucose sensing in clinical diagnostics.

Wearable biosensing devices represent an exciting frontier for MXenes, thanks to their flexibility, mechanical robustness, and ease of integration with flexible substrates. Beyond biomolecule detection, MXenes also exhibit intrinsic antibacterial properties, thereby improving biosensor longevity and reliability by reducing biofouling. The sharp edges of MXene nanosheets and their oxidative potential disrupt bacterial membranes, generating reactive oxygen species that provide antimicrobial effects without the need for antibiotics or additional coatings. This feature is particularly beneficial for implantable biosensors or devices operating in biological fluids where contamination can degrade performance.

Fig. 12 illustrates two innovative applications of MXene-based electrochemical biosensors that leverage the material's exceptional surface area, conductivity, and functional versatility for biomedical diagnostics. In Fig. 12A, a sandwich-type electrochemiluminescence (ECL) biosensor is constructed for the detection of exosomes, specifically targeting MCF-7-derived exosomes, which are important biomarkers for breast cancer. The biosensor architecture involves a glassy carbon electrode (GCE) modified with a poly(*N*-isopropylacrylamide)-Au nanoparticle (PNIPAM-Au NP) composite layer. This provides carboxylic acid functional groups for immobilizing aptamer 1 (Apt1), which selectively binds to exosomes. Subsequently, a $Ti_3C_2T_x$ MXene-aptamer 2 (Apt2) nanocomposite is introduced to complete the sandwich structure. MXene's broad 2D surface and high charge mobility facilitate enhanced aptamer loading and strong ECL signal generation, significantly improving sensitivity in exosome quantification.[185]

In Fig. 12B, a different strategy is employed: a MXene-chitosan nanocomposite is used to modify a GCE to stabilize

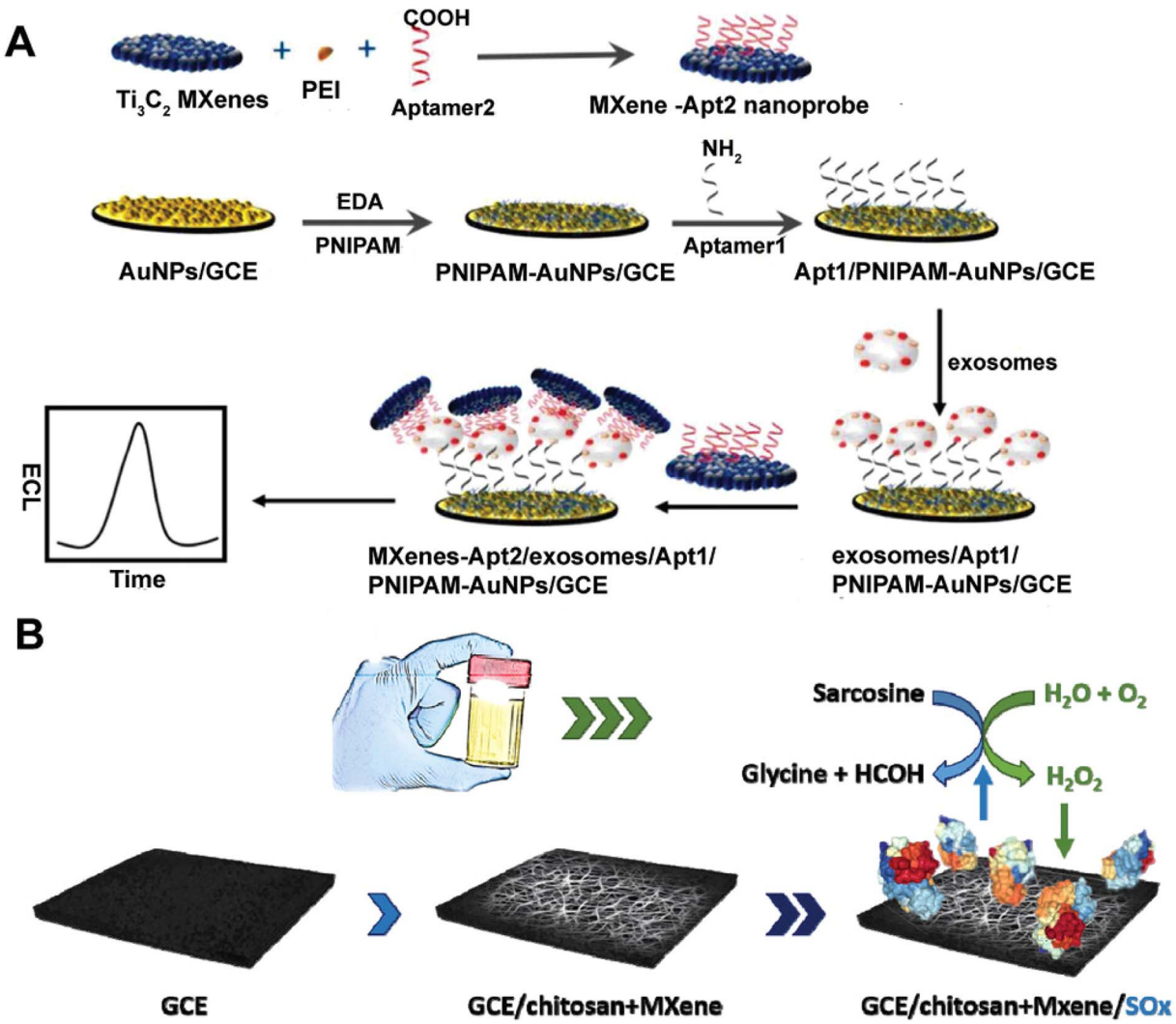

Fig. 12 (A) Schematic diagram of the MXene-based electrochemiluminescence biosensor for exosome detection. Glassy carbon electrode (GCE) was modified with PNIPAM-Au NPs to introduce carboxylic groups for immobilizing aptamer 1 (Apt1). Exosomes are captured on the surface, followed by incubation with $Ti_3C_2T_x$ MXene-aptamer 2 (Apt2) for signal amplification in a sandwich-type configuration, this figure has been adapted from ref. 187 with permission from Elsevier, copyright 2019. (B) Schematic of a sarcosine biosensor based on a $Ti_3C_2T_x$ MXene-chitosan nanocomposite-modified GCE, enabling the stabilization of sarcosine oxidase (SO_x) and electrochemical detection of sarcosine in urine *via* hydrogen peroxide reduction, this figure has been adapted from ref. 188 with permission from American Chemical Society, copyright 2000.

sarcosine oxidase (SO_x) in a biosensor for detecting sarcosine, a prostate cancer biomarker. Chitosan offers film-forming and biocompatible properties, while MXene provides excellent electron-transfer kinetics and catalytic activity. The biosensor exhibits a detection limit of 18 nM, a wide linear range (starting at 7.8 μM), and a fast response time of just 2 seconds. The detection is based on electrochemical reduction of H_2O_2, a byproduct of sarcosine oxidation. Furthermore, this platform demonstrates a high recovery rate of 102.6% in real urine samples, confirming its clinical potential.[186] These results underscore MXene's versatility in biosensor development and its role in advancing sensitive, rapid, and reliable diagnostic tools for both cancer biomarkers and exosomes.

The exceptional electrical conductivity and large specific surface area of MXenes have positioned them as highly promising materials for electrochemical biosensing. The unique 2D structure of MXene nanosheets enables efficient immobilization of biomolecules and rapid electron transfer, both of which are crucial for sensitive and selective detection of various biological analytes. Consequently, MXene-based biosensors have been successfully developed for detecting critical biomolecules, including glucose, DNA, proteins, and cells, with significant improvements in sensitivity, selectivity, and response time compared to traditional materials.

Glucose monitoring is paramount in clinical diagnostics, particularly for managing diabetes, which affects millions globally. MXenes have been extensively explored for the construction of glucose biosensors due to their high conductivity, biocompatibility, and ability to support enzyme immobilization. One of the pioneering works by Rakhi *et al.*[189] utilized

as a platform for sensitive enzymatic glucose detection, a biosensor based on an Au/MXene nanocomposite was developed. This biosensor exploits the unique electrocatalytic properties and synergistic effects between Au nanoparticles and MXene sheets. An amperometric glucose biosensor was fabricated by immobilizing glucose oxidase (GO_x) onto a Nafion-solubilized Au/MXene nanocomposite coated on a glassy carbon electrode (GCE). The biomediated Au nanoparticles significantly facilitate electron transfer between the electroactive center of GO_x and the electrode. The resulting GO_x/Au/MXene/Nafion/GCE electrode displayed a linear amperometric response over a glucose concentration range of 0.1–18 mM, with high sensitivity (4.2 μA mM^{-1} cm^{-2}) and a detection limit of 5.9 μM (S/N = 3). Moreover, the biosensor exhibited excellent stability, reproducibility, and repeatability, highlighting the potential of the Au/MXene nanocomposite as an efficient electrochemical transducer for biosensor applications.

The sensing mechanism relies on the enzymatic oxidation of glucose by GO_x:

1. Glucose + O_2 → GO_x → Gluconic acid + H_2O_2
2. H_2O_2 → O_2 + $2H^+$ + $2e^-$ (at the MXene-modified electrode)

The electrons produced during this reaction are efficiently transferred to the electrode owing to MXenes' excellent conductivity, thereby significantly enhancing the current signal. Meanwhile, the large surface area of the nanosheets enables a high loading of GO_x enzymes, thereby improving the sensor's sensitivity and response time. The synergy between enzyme activity and MXene conductivity establishes a robust platform for highly sensitive glucose detection, with potential applications in wearable devices and point-of-care diagnostics. Nucleic acid detection plays a vital role in genetic analysis, disease diagnosis, and personalized medicine. MXene nanosheets have emerged as powerful components in DNA biosensors due to their excellent capacity for probe immobilization and signal transduction.

A $Ti_3C_2T_x$ MXene-based biosensor was developed by using a photocatalytic atom transfer radical polymerization (photo-ATRP) amplification strategy for the detection of target miRNA-21 (tRNA). $Ti_3C_2T_x$ MXene nanosheets were synthesized by Nguyen *et al.*[190] from Ti_3AlC_2 MAX phase *via* selective aluminum etching and subsequently functionalized with 3-aminopropyl triethoxysilane (APTES) through silylation to enable covalent attachment of hairpin DNA designed for tRNA recognition. Upon binding with tRNA, the hairpin DNA released an azide (N_3) group, triggering a click reaction to attach a photo-ATRP initiator. Through ATRP photopolymerization, facilitated by an organic photoredox catalyst under light, a large amount of ferrocenyl methyl methacrylate (FMMA) monomer was immobilized on the electrode, resulting in amplified electrochemical signals. Electrochemical performance, evaluated *via* square wave voltammetry (SWV), showed exceptional sensitivity, with a linear detection range of 0.01 fM to 10 pM and a detection limit of 2.81 aM. The results demonstrate that this MXene-based biosensor, combined with the photo-ATRP amplification strategy, offers high reproducibility, stability, and sensitivity, highlighting its potential for applications in biomolecular diagnostics and experimental medical research.

MXenes enhance the biosensor's performance by providing a conductive and biocompatible surface that facilitates rapid electron transfer and maintains the bioactivity of immobilized probes. The 2D morphology of MXene sheets maximizes surface exposure and increases probe density, thereby improving hybridization efficiency. Furthermore, the abundant surface functional groups on MXenes enable covalent or non-covalent attachment of DNA probes without compromising their hybridization capability. This combination of features enables MXene-based DNA biosensors to achieve ultra-low detection limits and high selectivity, making them suitable for applications in early disease diagnosis and the monitoring of genetic mutations. Proteins serve as critical biomarkers for a wide range of diseases, including cardiovascular disorders, cancers, and infectious diseases. The sensitive detection of proteins such as cardiac troponin I (cTnI), prostate-specific antigen (PSA), and cytokines is crucial for timely diagnosis and effective therapeutic intervention.[191,192]

MXene-based protein biosensors have been developed by functionalizing MXene nanosheets with specific antibodies to capture target proteins. The high surface area and conductive nature of MXenes provide an ideal interface for antibody immobilization and signal amplification.

In a notable study, Li *et al.*[193] found that a convenient, rapid, and accurate detection of cardiac troponin I (cTnI) is essential for the early diagnosis of acute myocardial infarction (AMI). In this work, a paper-based electrochemical immunosensor was developed for label-free detection of cTnI, with the working electrode modified using Ti_3C_2 MXene nanosheets. To immobilize the bioreceptor (anti-cTnI) on the MXene-modified electrode, the nanosheets were functionalized with aminosilane and anchored onto the electrode surface *via* Nafion. The large surface area of MXene facilitates antibody immobilization, while its excellent electrical conductivity enhances electron transfer between the electroactive species and the electrode. Consequently, the paper-based immunosensor exhibited a wide detection range of 5–100 ng mL^{-1} and a low detection limit of 0.58 ng mL^{-1}, along with outstanding selectivity and good repeatability. This MXene-modified paper-based immunosensor enables fast, sensitive, and cost-effective detection of cTnI, offering strong potential for real-time clinical monitoring of AMI.

MXene's high conductivity facilitates enhanced electron transport, resulting in amplified sensor signals and rapid detection. MXene-based protein sensors also benefit from facile surface functionalization strategies that preserve antibody activity and improve sensor biocompatibility. The abundant surface terminations enable covalent bonding *via* well-established chemistries (*e.g.*, EDC/NHS coupling), ensuring robust antibody attachment and minimizing leaching during operation.[194]

MXene-polymer nanocomposites, as shown in Table 2, demonstrate remarkable versatility in biomedical applications, as highlighted in the comparative table. For antimicrobial purposes, $Ti_3C_2T_x$-chitosan composites effectively inhibit bacterial growth (62–95%), but they face durability challenges in physiological environments. In photothermal therapy (PTT),

Table 2 Biomedical applications of MXene

Application	MXene type	Polymer/composite	Key findings	Advantages	Limitations	Ref.
Antimicrobial agent	$Ti_3C_2T_x$	Chitosan (CS)	Growth inhibition: 62% (*S. aureus*), 95% (*E. coli*)	Biocompatible, biodegradable, high antibacterial activity	Limited durability in physiological environments	195
	Ti_3C_2	PVDF	Growth inhibition: 67% (*B. Subtilis*), 73% (*E. coli*)	High hydrophilicity, reduced membrane pores	Requires aging for optimal performance	196
Photothermal therapy (PTT)	Ti_3C_2	Soybean phospholipid (SP)	η: 30.6%, α: 25 Lg^{-1} cm^{-1} at 808 nm	High photothermal conversion efficiency, biocompatible	Potential oxidative instability	197
	Ti_3C_2	PLGA	η: 30.6%, α: 25 Lg^{-1} cm^{-1}, phase-changeable	Controlled drug release, enhanced stability	Complex synthesis process	179
	Mo_2C	PVA	η: 43.3% (1064 nm), 24.5% (808 nm); α: 12.3–18.0 Lg^{-1} cm^{-1}	Broad-spectrum NIR absorption, pH-dependent biodegradability	Requires high laser power density	198
Drug delivery	Ti_3C_2-SP	Doxorubicin (Dox)	Drug loading: 211.8%; pH/NIR-responsive release	High drug capacity, synergistic PTT/chemotherapy	Limited targeting specificity	199
	Ti_3C_2	Hyaluronic acid (HA)	Drug loading: 84.2%; enzyme/pH/NIR-responsive	Active tumor targeting, biocompatible	Degradation in physiological conditions	176
Bioimaging	Ta_4C_3-SP	MnO_x/Ti_3C_2-SP	Contrast-enhanced CT/MRI, η: 34.9% at 808 nm	Multimodal imaging, high atomic number (Ta)	High cost of Ta-based MXenes	200
	Nb_2C	PVP	η: 46.65% (1064 nm), 36.5% (808 nm); enzyme-triggered biodegradation	Radioprotective, ROS scavenging	Limited long-term toxicity data	197
Bone regeneration	$Ti_3C_2T_x$-OTES	PLA	UTS: 72 MPa; promotes osteogenic differentiation	Mechanical strength, biocompatibility	Requires surface modification for optimal performance	201
	Ti_3C_2	Polycaprolactone (PCL)	Enhanced pre-osteoblast adhesion and proliferation	High wettability, bioactivity	Limited *in vivo* validation	202
Biosensing	$Ti_3C_2T_x$	Glucose oxidase (GO_x)/Au	Glucose detection limit: 5.9 μM; sensitivity: 4.2 μA mM^{-1} cm^{-2}	High selectivity, real-time monitoring	Enzyme stability issues	189
	Ti_3C_2	Cellulose hydrogel	Water content: 98%; controlled drug release	Biodegradable, 3D network for sustained release	Slow degradation kinetics	203

Ti_3C_2-soybean phospholipid and Mo_2C-PVA systems exhibit high photothermal conversion efficiency (η = 30.6–43.3%) and NIR absorption, though oxidative instability remains a concern. Drug delivery platforms, such as Ti_3C_2-hyaluronic acid, enable pH/NIR-responsive release with a high drug-loading capacity (84–212%), yet targeting specificity and degradation kinetics require improvement. For bioimaging, Ta_4C_3-SP composites offer multimodal CT/MRI contrast but are costly, while Nb_2C-PVP serves as a radioprotective agent with enzyme-triggered biodegradation. Bone regeneration benefits from $Ti_3C_2T_x$-PLA's mechanical strength (UTS = 72 MPa) and osteogenic properties, though surface modifications are required. Biosensors utilizing $Ti_3C_2T_x$-glucose oxidase achieve sensitive detection (with a 5.9 μM limit), but struggle with enzyme stability. Overall, MXene composites excel in functionality but require optimization for clinical translation, addressing limitations such as toxicity, scalability, and long-term performance.

10. Recent advances in MXene materials

MXenes have remained one of the most active 2D material families in recent years because their metallic conductivity, tunable surface terminations, and layered structure make them unusually adaptable for energy storage and related functions. Recent reviews emphasize that progress is now coming less from pristine MXene alone and more from composite design, interfacial engineering, and surface functionalization, which together improve rate capability, cycling stability, and capacitance in supercapacitors and batteries.[204]

Recent advances in three-dimensional (3D) carbon- and MXene-based architectures highlight their critical role in enhancing electrochemical energy storage performance across hybrid capacitor and battery systems. For instance, the development of N and O co-doped hierarchical porous carbon (3DNOHC) with an ultrahigh specific surface area (~3477.69 m^2 g^{-1}) demonstrates how heteroatom doping and tailored porosity significantly improve ion adsorption/desorption kinetics and overall electrochemical behavior in aqueous zinc-ion hybrid capacitors, achieving high energy density and exceptional cycling stability.[205] Complementarily, the integration of MXene with carbon nanotubes in a 3D MXene-CNT composite effectively mitigates restacking issues while enhancing electronic conductivity and ion transport, resulting in remarkable reversible capacity and high energy/power densities in lithium-ion hybrid capacitors.[206] Furthermore, the construction of crumpled 3D MXene frameworks provides a robust host for lithium metal anodes, where the interconnected porous structure and abundant nucleation sites suppress dendrite growth and enable stable long-term cycling performance.[207] Collectively, these studies underscore the importance of rational 3D structural engineering, heteroatom doping, and hybrid composite design in achieving high-performance electrochemical systems for next-generation energy storage applications. A particularly strong recent supercapacitor report showed that nearly full-oxygen functionalization of Ti3C2Oy created a very high density of Ti–O/═O redox-active sites, delivering 1082 F g^{-1} and 3182 F cm^{-3} with excellent stability across a wide temperature range.[208] In parallel, MXene-based films and hybrids are being pushed beyond energy storage into EMI shielding and biomedical platforms, which reinforces the case that MXenes are no longer a niche electrode material but a broader multifunctional nanoplatform.[209]

Niobium and chromium nitrides stand out as the most mature members of this set for supercapacitors, while manganese and lanthanum nitride remain much earlier-stage and less directly evidenced. Recent work shows that Nb_4N_5 is attractive because of its high-valence states, metallic conductivity, and environmental friendliness, and porous single-crystal Nb_4N_5 reached 12.9 F cm^{-2} at 6 mA cm^{-2} with strong cycling stability, while hierarchical Nb@NbN core–shell nanocolumns delivered 53.3 mF cm^{-2} at 1 mA cm^{-2} and 93.5% retention after 20 000 cycles.[210] Chromium nitride is similarly promising in thin-film form: nanoporous CrN reached 53.92 mF cm^{-2} and 650 F cm^{-3} in acid electrolyte, CrN microspheres gave 213.2 F g^{-1} with 96% retention after 5000 cycles, and doping or compositing improved performance further, including Au-incorporated CrN and V-doped CrN.[211] By contrast, manganese nitride MnN thin films that showed a dominantly capacitive response and 16 mF cm^{-2} at 10 mV s^{-1}, so its practical case is still preliminary.[212] The closest recent evidence was a lanthanum-containing nitride/oxynitride composite, $Co_4N@La_2O_2CN_2$, which achieved 613.4 F g^{-1} and 87.9% retention after 10 000 cycles, suggesting lanthanum chemistry may be useful as a stabilizing matrix rather than as a standalone nitride electrode at present.[213,214]

11. Challenges in MXene technology and future aspect

MXene nanosheets, exemplified by $Ti_3C_2T_x$, exhibit remarkable electrical, mechanical, and chemical properties but suffer from severe oxidation instability under ambient and aqueous conditions, fundamentally limiting their practical applications. Oxidation initiates through the adsorption of oxygen and water molecules at surface terminations, forming reactive intermediates such as titanium oxides (TiO_{2-x}) and hydroxides that progressively degrade the 2D layered structure, resulting in conductivity loss and morphological collapse. This process follows complex pathways involving nucleophilic attack by water under electrochemical potentials, accelerated by environmental factors such as elevated temperatures (>60 °C), high humidity (>50% RH), and alkaline pH (>8), where hydroxide ions catalyze metal dissolution. In contrast, mildly acidic conditions (pH 4–6) offer temporary stabilization by protonating terminations and reducing ROS formation. Surface chemistry plays a pivotal role: fluorine-terminated (–F) MXenes demonstrate superior resistance due to lower oxygen affinity compared to –OH or –O groups, though the latter enhance hydrophilicity at the expense of stability. In aqueous dispersions, H_2 gas evolution from termination hydrolysis further

disrupts interlayer spacing, compromising the integrity of water-intensive applications such as supercapacitors and electrocatalysis. These degradation kinetics, often monitored *via* UV-Vis spectroscopy (loss of characteristic peaks at ~800 nm) or XPS (Ti(IV)/Ti(III) ratio shifts), underscore the need for immediate intervention, as shelf-life can drop from months to days without protection[215]

The literature reports a wide range of oxidation behaviors for $Ti_3C_2T_x$ MXenes, with some studies demonstrating stability over several weeks, while others document rapid oxidation within hours under nominally ambient conditions. These observations do not represent a genuine scientific contradiction; rather, they arise from the combined influence of several interdependent parameters that are often not systematically reported or controlled across studies.

First, the synthesis route and associated defect density exert a primary influence on oxidation kinetics. MXenes produced *via* concentrated HF etching typically exhibit a higher density of surface vacancies, edge defects, and structural disorder than those synthesized using milder fluoride-assisted routes (*e.g.*, LiF/HCl). Such defects serve as preferential nucleation sites for TiO_2 formation and substantially accelerate the onset of oxidation. Consequently, HF-etched $Ti_3C_2T_x$ with high defect densities may undergo significant degradation within hours. In contrast, low-defect MXenes prepared by MILD methods can maintain structural integrity for weeks under otherwise comparable environmental conditions.

Second, surface-termination chemistry plays a nuanced, sometimes counterintuitive role. Fluorine-terminated surfaces generally exhibit greater resistance to oxidative attack, as the Ti–F bond shows a lower affinity for oxygen incorporation. In contrast, –OH-rich surfaces, which are more prevalent in MILD-etched MXenes, are inherently more susceptible to moisture-assisted oxidation. As a result, although MILD-prepared MXenes are often considered structurally superior due to reduced defect density, their higher –OH content can partially offset this advantage. The overall oxidative stability therefore, reflects a balance between defect-mediated oxidation and termination-controlled chemical reactivity.

Third, environmental conditions critically modulate oxidation behavior. Elevated temperature (typically above 60 °C), high relative humidity (exceeding ~50%), and alkaline environments (pH > 8) each independently accelerate oxidation through distinct thermodynamic and kinetic pathways. Studies reporting extended stability commonly employ dehydrated samples, inert storage atmospheres (*e.g.*, Ar or N_2), or mildly acidic conditions (pH 4–6). In contrast, reports of rapid degradation frequently involve exposure to open air under ambient humidity, emphasizing the importance of environmental control in stability assessments.

Finally, the physical form of the MXene material significantly affects its oxidation rate. Colloidal dispersions exhibit substantially higher surface-area-to-volume ratios than compact freestanding films, rendering them more vulnerable to oxidative degradation under identical conditions. This distinction helps explain why colloidal $Ti_3C_2T_x$ suspensions are often reported to degrade within 24–72 hours, whereas dense films can remain stable for extended periods.

Taken together, these four interrelated factors, synthesis route and defect density, termination chemistry, environmental conditions, and physical form, constitute a coherent mechanistic framework that fully reconciles the seemingly contradictory stability data reported in the literature. For meaningful cross-study comparison and rational material design, it is therefore essential that future studies explicitly report synthesis methodology, termination composition, sample morphology, and storage or testing conditions alongside stability metrics.

Researchers have developed multifaceted chemical and physical strategies to combat MXene oxidation, significantly extending operational lifetimes from hours to over a year in controlled settings. Chemical approaches include antioxidant addition, such as sodium ascorbate or hydroquinone (0.1–1 wt%), which scavenge reactive oxygen species (ROS) by donating electrons and forming stable complexes with Ti^{4+} precursors, achieving up to 90% stability improvement in aqueous colloids over 30 days. Covalent passivation *via* silane coupling agents or polymer brushes (*e.g.*, PEG, PDA) creates hydrophobic barriers, reducing water ingress and O_2 diffusion by 70–80%, while preserving conductivity (>10 000 S m^{-1}). Ionic intercalation with Li^+, Na^+, or TMA^+ ions expands the interlayer spacing and modifies the electronic band structure, slowing oxidation kinetics by 5–10× through vacancy suppression. Physical methods encompass encapsulation in inert matrices like graphene oxide or PVDF, forming core–shell structures that block 95% of oxidative exposure, and dehydration *via* freeze-drying for powder storage under Ar/N_2 atmospheres (<1 ppm O_2). Compositional engineering introduces multi-transition-metal MXenes (*e.g.*, TiVNbC), leveraging synergistic lattice strain and higher formation energies to achieve 2–3× enhanced intrinsic resistance. Despite these advances, challenges persist in scalability, antioxidant leaching in dynamic environments, coating uniformity at industrial scales, and cost-effectiveness necessitating hybrid approaches for real-world deployment[134,216–218]

Building on the specific challenges identified in this review, we offer a differentiated projection of MXene research trajectories organized by realistic timeframe and technical readiness. In the near term (2–5 years), advances are most imminent in three domains: (i) scalable EMI shielding fabrication, where continuous roll-to-roll deposition of MXene/polymer films now achieves shielding effectiveness exceeding 50 dB at thicknesses below 100 μm, and industrially relevant coating uniformity is within reach; (ii) fluoride-free MXene synthesis *via* alkali-assisted and molten-salt routes, which are approaching yield parity with HF etching while substantially reducing hazardous byproducts; and (iii) point-of-care electrochemical biosensors, for which MXene-based platforms have demonstrated clinically relevant detection limits for cardiac troponin, glucose, and miRNA, with wearable integration presenting the primary remaining engineering hurdle. In the medium term (5–10 years), the most consequential advance will likely be solving MXene oxidation at the device level. The paradox noted earlier that MILD-synthesized MXenes combine low defect density with

high –OH surface content that paradoxically accelerates humidity-driven oxidation points to termination engineering as the critical lever: selectively replacing –OH with –F or –O groups through post-synthetic plasma or thermal treatment is the most tractable pathway. Solid-state MXene supercapacitor architectures and MXene-enhanced lithium-sulfur batteries are at an intermediate stage of development, with rate capability approaching theoretical limits but cycle life under real operating conditions remaining unresolved. In drug delivery, systematic *in vivo* pharmacokinetic and biodistribution characterization across organ systems is a prerequisite for regulatory engagement and must be prioritized. In the long term, theranostic MXene platforms integrating drug delivery, photothermal therapy, and imaging represent a scientifically compelling but clinically distant goal, contingent on resolving immunogenicity and scalable surface functionalization. Spintronic and quantum information applications of MXene remain at a fundamental research stage and are unlikely to reach applied maturity within a decade.[219]

12. Conclusion

MXene nanosheets have emerged as one of the most versatile and promising families of two-dimensional materials, with exceptional properties including metallic conductivity, hydrophilicity, tunable surface chemistry, mechanical robustness, and high surface area. This review has comprehensively examined the synthesis, structure–property relationships, and advanced applications of MXenes across three key domains: energy storage, EMI shielding, and biomedicine. In energy storage, MXenes exhibit notable pseudocapacitive behavior and rapid ion intercalation, enabling high-performance supercapacitors and batteries with excellent rate capability and cycling stability. Their layered structure and functionalized surfaces facilitate efficient charge storage, positioning them as leading candidates for next-generation flexible and wearable energy devices. For EMI shielding, MXenes offer remarkable attenuation through synergistic reflection, absorption, and multiple internal reflections. Their high electrical conductivity and lightweight, flexible nature make them superior to traditional metal-based shields, particularly for applications in 5 G communications, aerospace, and wearable electronics. In biomedicine, MXenes demonstrate significant potential in drug delivery, biosensing, and photothermal therapy. Their biocompatibility, large surface area, and ease of functionalization allow for targeted therapeutic delivery, sensitive biomarker detection, and multifunctional theranostic platforms, paving the way for advanced nanomedicine. Despite these promising advances, challenges remain in environmental stability, scalable synthesis, oxidation resistance, and long-term biocompatibility. Future research should focus on developing greener, safer synthesis routes, enhancing MXene stability through surface engineering, and advancing hybrid and composite architectures to unlock their full potential. With continued interdisciplinary innovation and optimization, MXenes are poised to play a transformative role in sustainable energy, advanced electronics, and precision medicine, driving forward the next generation of functional materials and technologies.

Author contributions

All authors contributes equally.

Conflicts of interest

The authors declare that they have no conflicts of interest.

Abbreviations

2D	Two-dimensional
3D	Three-dimensional
Ag	Silver
AgNWs	Silver nanowires
Al	Aluminum
Al_2O_3	Aluminum oxide
$AlCl_3$	Aluminum chloride
ALD	Atomic layer deposition
ANF	Aramid nanofibers
As	Arsenic
Au	Gold
AuNPs	Gold nanoparticles
BSA	Bovine serum albumin
BC	Bacterial cellulose
BNNS	Boron nitride nanosheets
C	Carbon
CCM	Carbonized cellulose microspheres
CD31	Cluster of differentiation 31
CEA	Carcinoembryonic antigen
cTnI	Cardiac troponin I
Cl–	Chlorine group
CNF	Cellulose nanofiber
CNT	Carbon nanotubes
Cu	Copper
$CuCl_2$	Copper chloride
CT	Computed tomography
DMSO	Dimethyl sulfoxide
DNA	Deoxyribonucleic acid
DOX	Doxorubicin
DOS	Density of states
DPV	Differential pulse voltammetry
DFT	Density functional theory
ECL	Electrochemiluminescence
EDLC	Electric double-layer capacitance
EIS	Electrochemical impedance spectroscopy
EMI	Electromagnetic interference
EMI-TFSI	1-Ethyl-3-methylimidazolium bis(trifluoromethylsulfonyl)imide
EPR	Enhanced permeability and retention
Fe_3O_4	Iron oxide
$FeCl_3$	Iron chloride
FeF_3	Iron fluoride
FET	Field-effect transistor
F–	Fluorine group
Ga	Gallium

GCE	Glassy carbon electrode
Ge	Germanium
GO	Graphene oxide
GO_x	Glucose oxidase
HCl	Hydrochloric acid
HCHO	Oxidized hyaluronic acid
HF	Hydrofluoric acid
HPEM	Hyaluronic acid-poly(glycerol-ethyleneimine)-MXene
In	Indium
IoT	Internet of things
KCl	Potassium chloride
KF	Potassium fluoride
KCl	Potassium chloride
LSPR	Localized surface plasmon resonance
LbL	Layer-by-layer
LIBs	Lithium-ion batteries
LiF	Lithium fluoride
MAX	Mn+1AXn phases
MRI	Magnetic resonance imaging
MILD	Minimally intensive layer delamination
miRNA	MicroRNA
Mo	Molybdenum
MoS_2	Molybdenum disulfide
MRSA	Methicillin-resistant *Staphylococcus aureus*
MXene	Transition metal carbides, nitrides, carbonitrides
N	Nitrogen
NaCl	Sodium chloride
NaF	Sodium fluoride
NaOH	Sodium hydroxide
NH_4HF_2	Ammonium hydrogen fluoride
NIR	Near-infrared
NMR	Nuclear magnetic resonance
O–	Oxygen group
ORR	Oxygen reduction reaction
OTES	Octyltriethoxysilane
OH–	Hydroxyl group
α-SMA	Alpha-smooth muscle actin
P	Phosphorus
PANI	Polyaniline
PCL	Polycaprolactone
PDDA-BP	Poly(diallyldimethylammonium chloride)-biphenyl
PDMS	Polydimethylsiloxane
PEG	Polyethylene Glycol
PEI	Polyethyleneimine
PET	Polyethylene terephthalate
PIBs	Potassium-ion batteries
PLA	Polylactic acid
PLGA	Poly(lactic-*co*-glycolic acid)
PNIPAM	Poly(N-isopropylacrylamide)
PPy	Polypyrrole
PSA	Prostate-specific antigen
Pt	Platinum
PU	Polyurethane
PVDF	Polyvinylidene fluoride
PVA	Polyvinyl alcohol
PVP	Polyvinylpyrrolidone
rGO	Reduced graphene oxide
ROS	Reactive oxygen species
S	Sulfur
SE_A	Shielding effectiveness (absorption)
SE	Shielding effectiveness
SE_R	Shielding effectiveness (reflection)
SEM	Scanning electron microscopy
SE_M	Shielding effectiveness (multiple reflections)
(EMI)	
SERS	Surface-enhanced raman spectroscopy
SIBs	Sodium-ion batteries
Si	Silicon
SiO_2	Silicon dioxide
Sn	Tin
SO_x	Sarcosine oxidase
ssDNA	Single-stranded DNA
STM	Scanning tunneling microscopy
SWNT	Single-walled carbon nanotubes
Ta	Tantalum
TBAOH	Tetrabutylammonium hydroxide
TEM	Transmission electron microscopy
Ti	Titanium
TiO_2	Titanium dioxide
TMA-OH	Tetramethylammonium hydroxide
T_x	Surface terminations
UV	Ultraviolet
UTS	Ultimate tensile strength
V	Vanadium
XPS	X-ray photoelectron spectroscopy
XRD	X-ray diffraction
$ZnCl_2$	Zinc chloride

Data availability

No primary research results, software or code have been included and no new data were generated or analysed as part of this review.

Acknowledgements

This work was supported and funded by the Deanship of Scientific Research at Imam Mohammad Ibn Saud Islamic University (IMSIU) (grant number IMSIU-DDRSP2602).

References

1 B. Anasori, M. Naguib and E. Guest, *MRS Bull.*, 2023, **48**, 238–244.
2 B. Anasori and Y. Gogotsi, in *2D Metal Carbides and Nitrides (MXenes): Structure, Properties and Applications*, eds. B. Anasori and Y. Gogotsi, Springer International Publishing, Cham, 2019, pp. 3–12, DOI: 10.1007/978-3-030-19026-2_1.
3 M. Alhabeb, K. Maleski, B. Anasori, P. Lelyukh, L. Clark, S. Sin and Y. Gogotsi, *Chem. Mater.*, 2017, **29**, 7633–7644.
4 M. Khazaei, A. Ranjbar, M. Arai, T. Sasaki and S. Yunoki, *J. Mater. Chem. C*, 2017, **5**, 2488–2503.
5 M. W. Barsoum, *Prog. Solid State Chem.*, 2000, **28**, 201–281.

6 B. Anasori and Y. Gogotsi, *Graphene 2D Mater.*, 2022, **7**, 75–79.
7 Z. Ling, C. E. Ren, M.-Q. Zhao, J. Yang, J. M. Giammarco, J. Qiu, M. W. Barsoum and Y. Gogotsi, *Proc. Natl. Acad. Sci.*, 2014, **111**, 16676–16681.
8 M. Naguib, M. Kurtoglu, V. Presser, J. Lu, J. Niu, M. Heon, L. Hultman, Y. Gogotsi and M. W. Barsoum, in *MXenes*, Jenny Stanford Publishing, 2023, pp. 15–29.
9 G. Ljubek, M. Kralj and M. Kraljić Roković, *Mater. Sci. Technol.*, 2023, **39**, 1645–1649.
10 K. Gong, L. Yin and K. Zhou, in *MXene Reinforced Polymer Composites*, 2024, pp. 39–70, DOI: 10.1002/9781119901280.ch2.
11 M. Naguib, M. Kurtoglu, V. Presser, J. Lu, J. Niu, M. Heon, L. Hultman, Y. Gogotsi and M. W. Barsoum, *Adv. Mater.*, 2011, **23**, 4207.
12 B. Anasori, M. R. Lukatskaya and Y. Gogotsi, in *MXenes*, Jenny Stanford Publishing, 2023, pp. 677–722.
13 M. Naguib, V. N. Mochalin, M. W. Barsoum and Y. Gogotsi, *Adv. Mater.*, 2014, **26**, 992–1005.
14 M. A. Hope, A. C. Forse, K. J. Griffith, M. R. Lukatskaya, M. Ghidiu, Y. Gogotsi and C. P. Grey, *PCCP*, 2016, **18**, 5099–5102.
15 M. Jiang, D. Wang, Y. H. Kim, C. Duan, D. V. Talapin and C. Zhou, *Angew. Chem.*, 2024, **136**, e202409480.
16 R. Kulkarni, L. P. Lingamdinne, J. R. Koduru, R. R. Karri, Y.-Y. Chang, S. K. Kailasa and N. M. Mubarak, *ACS Mater. Lett.*, 2024, **6**, 2660–2686.
17 Z. Bo, Y. Chen, Q. Yu, J. Yan, K. Cen and Z. Liu, *J. Phys. Chem. C*, 2024, **128**, 2352–2361.
18 L. Liu, E. Raymundo-Piñero, S. Sunny, P. L. Taberna and P. Simon, *Angew. Chem.*, 2024, **136**, e202319238.
19 X. Wang, Z. Wang and J. Qiu, *Angew. Chem.*, 2021, **133**, 26791–26795.
20 A. Zarkov, *Materials*, 2024, **17**, 462.
21 A. Valladares-Barrera, A. D. Alcantar-Mendoza, A. García-Murillo, L. M. Palacios-Lazcano and F. J. Carrillo-Romo, *J. Sol-Gel Sci. Technol.*, 2025, **113**, 627–646.
22 A. E. Danks, S. R. Hall and Z. Schnepp, *Mater. Horiz.*, 2016, **3**, 91–112.
23 C. E. Shuck, K. Ventura-Martinez, A. Goad, S. Uzun, M. Shekhirev and Y. Gogotsi, *ACS Chem. Health Saf.*, 2021, **28**, 326–338.
24 M. Ghidiu, M. Naguib, C. Shi, O. Mashtalir, L. M. Pan, B. Zhang, J. Yang, Y. Gogotsi, S. J. L. Billinge and M. W. Barsoum, *Chem. Commun.*, 2014, **50**, 9517–9520.
25 S.-Y. Pang, Y.-T. Wong, S. Yuan, Y. Liu, M.-K. Tsang, Z. Yang, H. Huang, W.-T. Wong and J. Hao, *J. Am. Chem. Soc.*, 2019, **141**, 9610–9616.
26 O. Mashtalir, M. Naguib, V. N. Mochalin, Y. Dall'Agnese, M. Heon, M. W. Barsoum and Y. Gogotsi, *Nat. Commun.*, 2013, **4**, 1716.
27 A. Lipatov, M. Alhabeb, M. R. Lukatskaya, A. Boson, Y. Gogotsi and A. Sinitskii, *Adv. Electron. Mater.*, 2016, **2**, 1600255.
28 P. Sarkar, K. Chatterjee, P. Pal and K. Das, *Mater. Sci. Semicond. Process.*, 2025, **185**, 108881.
29 A. Gentile, S. Marchionna, M. Balordi, G. Pagot, C. Ferrara, V. Di Noto and R. Ruffo, *ChemElectroChem*, 2022, **9**, e202200891.
30 S. Yang, P. Zhang, F. Wang, A. G. Ricciardulli, M. R. Lohe, P. W. M. Blom and X. Feng, *Angew. Chem., Int. Ed.*, 2018, **57**, 15491–15495.
31 J. Halim, S. Kota, M. R. Lukatskaya, M. Naguib, M.-Q. Zhao, E. J. Moon, J. Pitock, J. Nanda, S. J. May, Y. Gogotsi and M. W. Barsoum, *Adv. Funct. Mater.*, 2016, **26**, 3118–3127.
32 Y. Li, H. Shao, Z. Lin, J. Lu, L. Liu, B. Duployer, P. O. Å. Persson, P. Eklund, L. Hultman, M. Li, K. Chen, X.-H. Zha, S. Du, P. Rozier, Z. Chai, E. Raymundo-Piñero, P.-L. Taberna, P. Simon and Q. Huang, *Nat. Mater.*, 2020, **19**, 894–899.
33 B. Soundiraraju and B. K. George, *ACS Nano*, 2017, **11**, 8892–8900.
34 J. Zhang, N. Kong, S. Uzun, A. Levitt, S. Seyedin, P. A. Lynch, S. Qin, M. Han, W. Yang and J. Liu, in *MXenes*, Jenny Stanford Publishing, 2023, pp. 519–538.
35 P. Huang and W.-Q. Han, *Nano-Micro Lett.*, 2023, **15**, 68.
36 M. Mim, K. Habib, S. N. Farabi, S. A. Ali, M. A. Zaed, M. Younas and S. Rahman, *ACS Omega*, 2024, **9**, 32350–32393.
37 A. Lipatov, H. Lu, M. Alhabeb, B. Anasori, A. Gruverman, Y. Gogotsi and A. Sinitskii, *Sci. Adv.*, 2018, **4**, eaat0491.
38 M. Kurtoglu, M. Naguib, Y. Gogotsi and M. W. Barsoum, *MRS Commun.*, 2012, **2**, 133–137.
39 A. Thakur, N. Chandran Bs, K. Davidson, A. Bedford, H. Fang, Y. Im, V. Kanduri, B. C. Wyatt, S. K. Nemani and V. Poliukhova, *Small Methods*, 2023, **7**, 2300030.
40 M. Naguib, R. R. Unocic, B. L. Armstrong and J. Nanda, *DTr*, 2015, **44**, 9353–9358.
41 K. Maleski, V. N. Mochalin and Y. Gogotsi, *Chem. Mater.*, 2017, **29**, 1632–1640.
42 M. Seredych, C. E. Shuck, D. Pinto, M. Alhabeb, E. Precetti, G. Deysher, B. Anasori, N. Kurra and Y. Gogotsi, *Chem. Mater.*, 2019, **31**, 3324–3332.
43 V. Kamysbayev, A. S. Filatov, H. Hu, X. Rui, F. Lagunas, D. Wang, R. F. Klie and D. V. Talapin, *Science*, 2020, **369**, 979–983.
44 V. Natu, M. Sokol, L. Verger and M. W. Barsoum, *J. Phys. Chem. C*, 2018, **122**, 27745–27753.
45 M. Malaki, A. Maleki and R. S. Varma, *J. Mater. Chem. A*, 2019, **7**, 10843–10857.
46 T. Zhang, L. Pan, H. Tang, F. Du, Y. Guo, T. Qiu and J. Yang, *J. Alloys Compd.*, 2017, **695**, 818–826.
47 C. E. Shuck, A. Sarycheva, M. Anayee, A. Levitt, Y. Zhu, S. Uzun, V. Balitskiy, V. Zahorodna, O. Gogotsi and Y. Gogotsi, in *MXenes*, Jenny Stanford Publishing, 2023, pp. 539–560.
48 A. Levitt, J. Zhang, G. Dion, Y. Gogotsi and J. M. Razal, *Adv. Funct. Mater.*, 2020, **30**, 2000739.
49 M. Anayee, N. Kurra, M. Alhabeb, M. Seredych, M. N. Hedhili, A.-H. Emwas, H. N. Alshareef, B. Anasori and Y. Gogotsi, *Chem. Commun.*, 2020, **56**, 6090–6093.
50 A. S. Levitt, M. Alhabeb, C. B. Hatter, A. Sarycheva, G. Dion and Y. Gogotsi, *J. Mater. Chem. A*, 2019, **7**, 269–277.

51 M. Naguib, O. Mashtalir, J. Carle, V. Presser, J. Lu, L. Hultman, Y. Gogotsi and M. W. Barsoum, *ACS Nano*, 2012, **6**, 1322–1331.
52 D. Pinto, B. Anasori, H. Avireddy, C. E. Shuck, K. Hantanasirisakul, G. Deysher, J. R. Morante, W. Porzio, H. N. Alshareef and Y. Gogotsi, *J. Mater. Chem. A*, 2020, **8**, 8957–8968.
53 C. Lu, L. Yang, B. Yan, L. Sun, P. Zhang, W. Zhang and Z. Sun, *Adv. Funct. Mater.*, 2020, **30**, 2000852.
54 I. Ihsanullah, *Chem. Eng. J.*, 2020, **388**, 124340.
55 M. Seredych, K. Maleski, T. S. Mathis and Y. Gogotsi, *Colloids Surf. Physicochem. Eng. Aspects*, 2022, **641**, 128580.
56 J. Peng, X. Chen, W.-J. Ong, X. Zhao and N. Li, *Chem*, 2019, **5**, 18–50.
57 I. Persson, A. el Ghazaly, Q. Tao, J. Halim, S. Kota, V. Darakchieva, J. Palisaitis, M. W. Barsoum, J. Rosen and P. O. Å. Persson, *Small*, 2018, **14**, 1703676.
58 A. Sarycheva, A. Polemi, Y. Liu, K. Dandekar, B. Anasori and Y. Gogotsi, *Sci. Adv.*, 2018, **4**, eaau0920.
59 A. D. Dillon, M. J. Ghidiu, A. L. Krick, J. Griggs, S. J. May, Y. Gogotsi, M. W. Barsoum and A. T. Fafarman, *Adv. Funct. Mater.*, 2016, **26**, 4162–4168.
60 K. Huang, Z. Li, J. Lin, G. Han and P. Huang, *Chem. Soc. Rev.*, 2018, **47**, 5109–5124.
61 Y. Dall'Agnese, P. Rozier, P.-L. Taberna, Y. Gogotsi and P. Simon, *J. Power Sources*, 2016, **306**, 510–515.
62 K. Hantanasirisakul, M.-Q. Zhao, P. Urbankowski, J. Halim, B. Anasori, S. Kota, C. E. Ren, M. W. Barsoum and Y. Gogotsi, *Adv. Electron. Mater.*, 2016, **2**, 1600050.
63 M. Naguib, J. Halim, J. Lu, K. M. Cook, L. Hultman, Y. Gogotsi and M. W. Barsoum, *J. Am. Chem. Soc.*, 2013, **135**, 15966–15969.
64 M. Benchakar, L. Loupias, C. Garnero, T. Bilyk, C. Morais, C. Canaff, N. Guignard, S. Morisset, H. Pazniak, S. Hurand, P. Chartier, J. Pacaud, V. Mauchamp, M. W. Barsoum, A. Habrioux and S. Célérier, *Appl. Surf. Sci.*, 2020, **530**, 147209.
65 C. E. Shuck, M. Han, K. Maleski, K. Hantanasirisakul, S. J. Kim, J. Choi, W. E. B. Reil and Y. Gogotsi, *ACS Appl. Nano Mater.*, 2019, **2**, 3368–3376.
66 L. Guo, W.-Y. Jiang, M. Shen, C. Xu, C.-X. Ding, S.-F. Zhao, T.-T. Yuan, C.-Y. Wang, X.-Q. Zhang and J.-Q. Wang, *Electrochim. Acta*, 2022, **401**, 139476.
67 F. Shahzad, M. Alhabeb, C. B. Hatter, B. Anasori, S. Man Hong, C. M. Koo and Y. Gogotsi, *Science*, 2016, **353**, 1137–1140.
68 M. Mozafari and M. Soroush, *Mater. Adv.*, 2021, **2**, 7277–7307.
69 A. Khosla, Sonu, H. T. A. Awan, K. Singh, Gaurav, R. Walvekar, Z. Zhao, A. Kaushik, M. Khalid and V. Chaudhary, *Advanced Science*, 2022, **9**, 2203527.
70 S. Jung, U. Zafar, L. S. K. Achary and C. M. Koo, *EcoMat*, 2023, **5**, e12395.
71 M. Tang, J. Li, Y. Wang, W. Han, S. Xu, M. Lu, W. Zhang and H. Li, *Symmetry*, 2022, **14**, 2232.
72 F. Brette, D. Kourati, M. Paris, L. Loupias, S. Célérier, T. Cabioc'h, M. Deschamps, F. Boucher and V. Mauchamp, *J. Am. Chem. Soc.*, 2023, **145**, 4003–4014.
73 R. Ibragimova, P. Erhart, P. Rinke and H.-P. Komsa, *J. Phys. Chem. Lett.*, 2021, **12**, 2377–2384.
74 T. Su, X. Ma, J. Tong, H. Ji, Z. Qin and Z. Wu, *J. Mater. Chem. A*, 2022, **10**, 10265–10296.
75 J. Björk and J. Rosen, *Chem. Mater.*, 2021, **33**, 9108–9118.
76 D. Meng, M. Xu, S. Li, M. Ganesan, X. Ruan, S. K. Ravi and X. Cui, *Small*, 2024, **20**, 2304483.
77 Y.-Z. Zhang, J. K. El-Demellawi, Q. Jiang, G. Ge, H. Liang, K. Lee, X. Dong and H. N. Alshareef, *Chem. Soc. Rev.*, 2020, **49**, 7229–7251.
78 G. Ma, H. Shao, J. Xu, Y. Liu, Q. Huang, P.-L. Taberna, P. Simon and Z. Lin, *Nat. Commun.*, 2021, **12**, 5085.
79 X. Hui, X. Ge, R. Zhao, Z. Li and L. Yin, *Adv. Funct. Mater.*, 2020, **30**, 2005190.
80 Y. Wu, H. Hu, C. Yuan, J. Song and M. Wu, *Nano Energy*, 2020, **74**, 104812.
81 Ü. Ö. Akkuş, E. Balcı and S. Berber, *Superlattices Microstruct.*, 2020, **140**, 106433.
82 L. Chen, Y. Cao, X. Zhang, X. Guo, P. Song, K. Chen and J. Lin, *JMatS*, 2020, **55**, 16533–16543.
83 W. Shao, M. Tebyetekerwa, I. Marriam, W. Li, Y. Wu, S. Peng, S. Ramakrishna, S. Yang and M. Zhu, *J. Power Sources*, 2018, **396**, 683–690.
84 S. Seyedin, E. R. S. Yanza and J. M. Razal, *J. Mater. Chem. A*, 2017, **5**, 24076–24082.
85 Z. Guo, Y. Li, Z. Lu and W. Liu, *J. Phys.: Conf. Ser.*, 2021, **1790**, 012066.
86 M. Boota, B. Anasori, C. Voigt, M.-Q. Zhao, M. W. Barsoum and Y. Gogotsi, *Adv. Mater.*, 2016, **28**, 1517–1522.
87 A. J. Y. Wong, K. R. G. Lim and Z. W. Seh, *J. Mater. Res.*, 2022, **37**, 3988–3997.
88 L. Yu, L. Lu, X. Zhou and L. Xu, *Adv. Mater. Interfaces*, 2023, **10**, 2201818.
89 Z. U. D. Babar, V. Iannotti, G. Rosati, A. Zaheer, R. Velotta, B. Della Ventura, R. Álvarez-Diduk and A. Merkoçi, *Chem. Soc. Rev.*, 2025, **54**, 3387–3440.
90 S. Wang, Y. Liu, Y. Liu and W. Hu, *Chem. Eng. J.*, 2023, **452**, 139512.
91 S. Kumar, *Small*, 2024, **20**, 2308225.
92 H. Zhang, L. Wang, Q. Chen, P. Li, A. Zhou, X. Cao and Q. Hu, *Mater. Des.*, 2016, **92**, 682–689.
93 M. Mehrpooya, M. Hadavand and M. R. Ganjali, *Mater. Chem. Phys.*, 2025, **332**, 130076.
94 A. VahidMohammadi, J. Rosen and Y. Gogotsi, *Science*, 2021, **372**, eabf1581.
95 A. Nayak, A. Priyadarshini and S. P. Mantry, *MXenes*, 2024, 206–225.
96 P. Kumar, R. Rana, A. Kumar, P. Rawat and J. S. Rhyee, in *MXenes*, 2024, pp. 23–44, DOI: 10.1002/9781119874027.ch2.
97 S. Lee, E. H. Kim, S. Yu, H. Kim, C. Park, S. W. Lee, H. Han, W. Jin, K. Lee, C. E. Lee, J. Jang, C. M. Koo and C. Park, *ACS Nano*, 2021, **15**, 8940–8952.
98 L. Zhou, Y. Zhang, Z. Zhuo, A. J. Neukirch and S. Tretiak, *J. Phys. Chem. Lett.*, 2018, **9**, 6915–6920.
99 G. Li, B. C. Wyatt, F. Song, C. Yu, Z. Wu, X. Xie, B. Anasori and N. Zhang, *Adv. Funct. Mater.*, 2021, **31**, 2105043.

100 Z. Zhuang, H. Chen and C. Li, *ACS Nano*, 2023, **17**, 10628–10636.
101 L. Chen, X. Shi, N. Yu, X. Zhang, X. Du and J. Lin, *Materials*, 2018, **11**, 1701.
102 E. Aydin, J. K. El-Demellawi, E. Yarali, F. Aljamaan, S. Sansoni, A. u. Rehman, G. Harrison, J. Kang, A. El Labban, M. De Bastiani, A. Razzaq, E. Van Kerschaver, T. G. Allen, O. F. Mohammed, T. Anthopoulos, H. N. Alshareef and S. De Wolf, *ACS Nano*, 2022, **16**, 2419–2428.
103 S. Uzun, M. Han, C. J. Strobel, K. Hantanasirisakul, A. Goad, G. Dion and Y. Gogotsi, *Carbon*, 2021, **174**, 382–389.
104 T. Hu, H. Zhang, J. Wang, Z. Li, M. Hu, J. Tan, P. Hou, F. Li and X. Wang, *Sci. Rep.*, 2015, **5**, 16329.
105 O. de Leuze, F. M. Fernandes, S. Arib, L. Caputo, A. P. Fontes, V.-H. Nguyen, H. Pazniak, B. Nysten, J.-C. Charlier, S. Hermans and B. Hackens, *Commun. Mater.*, 2025, **6**, 186.
106 R. Osama, L. Rajan, J. Urbančič, A. S. Nia, S. Khosravi, C. Grazioli, M. Dell'Angela, R. Costantini, E. Pavlica, G. De Ninno and B. Ressel, *Phys. Status Solidi RRL*, 2025, e202500372.
107 M. Mičušík, M. Šlouf, A. Stepura, Y. Soyka, E. Ovodok, M. Procházka and M. Omastová, *Appl. Surf. Sci.*, 2023, **610**, 155351.
108 F. M. Römer, U. Wiedwald, T. Strusch, J. Halim, E. Mayerberger, M. W. Barsoum and M. Farle, *RSC Adv.*, 2017, **7**, 13097–13103.
109 J. F. Pöhls and R. T. Weitz, *Adv. Funct. Mater.*, 2025, e13932.
110 Y. Gao, H.-I. Un, Y. Huang, H. Sirringhaus and I. E. Jacobs, *arXiv*, preprint arXiv:2602.02418, 2026, DOI: 10.48550/arXiv.2602.02418.
111 R. A. Veazey, A. S. Gandy, D. C. Sinclair and J. S. Dean, *J. Am. Ceram. Soc.*, 2019, **102**, 3609–3622.
112 G. R. Berdiyorov, *Europhys. Lett.*, 2015, **111**, 67002.
113 R. Khanal and S. Irle, *J. Chem. Phys.*, 2023, **158**, 194701.
114 B. Aïssa, A. Ali, K. A. Mahmoud, T. Haddad and M. Nedil, *Appl. Phys. Lett.*, 2016, **109**, 043109.
115 S. W. Koh, L. Rekhi, Arramel, M. D. Birowosuto, Q. T. Trinh, J. Ge, W. Yu, A. T. S. Wee, T. S. Choksi and H. Li, *ACS Appl. Mater. Interfaces*, 2024, **16**, 66826–66836.
116 L. Gao, W. Bao, A. V. Kuklin, S. Mei, H. Zhang and H. Ågren, *Adv. Mater.*, 2021, **33**, 2004129.
117 Z. Wang, H. Kim and H. N. Alshareef, *Adv. Mater.*, 2018, **30**, 1706656.
118 K. Nasrin, V. Sudharshan, K. Subramani and M. Sathish, *Adv. Funct. Mater.*, 2022, **32**, 2110267.
119 D. H. Ho, Y. Y. Choi, S. B. Jo, J.-M. Myoung and J. H. Cho, *Adv. Mater.*, 2021, **33**, 2005846.
120 Y. Z. Chu, M. Hoover, P. Ward and K. C. Lau, *iScience*, 2024, **27**, 108784.
121 M. Khazaei, M. Arai, T. Sasaki, C.-Y. Chung, N. S. Venkataramanan, M. Estili, Y. Sakka and Y. Kawazoe, *Adv. Funct. Mater.*, 2013, **23**, 2185–2192.
122 M. R. Lukatskaya, O. Mashtalir, C. E. Ren, Y. Dall'Agnese, P. Rozier, P. L. Taberna, M. Naguib, P. Simon, M. W. Barsoum and Y. Gogotsi, *Science*, 2013, **341**, 1502–1505.
123 V. N. Borysiuk, V. N. Mochalin and Y. Gogotsi, *Nanotechnology*, 2015, **26**, 265705.
124 A. Lipatov, H. Lu, M. Alhabeb, B. Anasori, A. Gruverman, Y. Gogotsi and A. Sinitskii, *Sci. Adv.*, 2018, **4**, eaat0491.
125 T. Habib, X. Zhao, S. A. Shah, Y. Chen, W. Sun, H. An, J. L. Lutkenhaus, M. Radovic and M. J. Green, *npj 2D Mater. Appl.*, 2019, **3**, 8.
126 K. M. R. Rifat, S. Sarker, R. Islam, S. Nasif, M. Z. Mahmud, D. Das, M. A. Taleb, M. N. Rahman and M. M. Hasan, 2025.
127 Y. Wang, X. Wang, X. Li, Y. Bai, H. Xiao, Y. Liu, R. Liu and G. Yuan, *Adv. Funct. Mater.*, 2019, **29**, 1900326.
128 S. Sarangapani, B. Tilak and C. P. Chen, *J. Electrochem. Soc.*, 1996, **143**, 3791–3799.
129 S. Fleischmann, J. B. Mitchell, R. Wang, C. Zhan, D.-e. Jiang, V. Presser and V. Augustyn, *Chem. Rev.*, 2020, **120**, 6738–6782.
130 R. Soni, V. Kashyap, D. Nagaraju and S. Kurungot, *ACS Appl. Mater. Interfaces*, 2018, **10**, 676–686.
131 H. Yoo, M. Min, S. Bak, Y. Yoon and H. Lee, *J. Mater. Chem. A*, 2014, **2**, 6663–6668.
132 S. Zhao, Z. Song, L. Qing, J. Zhou and C. Qiao, *J. Phys. Chem. C*, 2022, **126**, 9248–9256.
133 D. Wu, Y. Zhang, Z. Man, H. Zhang, X. Zhu, J. Ding, J. Xu, N. Bao and W. Lu, *Adv. Energy Mater.*, 2024, **14**, 2304404.
134 F. Cao, Y. Zhang, H. Wang, K. Khan, A. K. Tareen, W. Qian, H. Zhang and H. Ågren, *Adv. Mater.*, 2022, **34**, 2107554.
135 M. Ghidiu, M. R. Lukatskaya, M.-Q. Zhao, Y. Gogotsi and M. W. Barsoum, in *MXenes*, Jenny Stanford Publishing, 2023, pp. 379–399.
136 Y. Dall'Agnese, P.-L. Taberna, Y. Gogotsi and P. Simon, *J. Phys. Chem. Lett.*, 2015, **6**, 2305–2309.
137 Z. Lin, D. Barbara, P.-L. Taberna, K. L. Van Aken, B. Anasori, Y. Gogotsi and P. Simon, *J. Power Sources*, 2016, **326**, 575–579.
138 M.-Q. Zhao, C. E. Ren, Z. Ling, M. R. Lukatskaya, C. Zhang, K. L. Van Aken, M. W. Barsoum and Y. Gogotsi, *Adv. Mater.*, 2014, 27.
139 M. Boota, B. Anasori, C. Voigt, M.-Q. Zhao, M. W. Barsoum and Y. Gogotsi, *Adv. Mater.*, 2016, **28**, 1517–1522.
140 M. Naguib, J. Come, B. Dyatkin, V. Presser, P.-L. Taberna, P. Simon, M. W. Barsoum and Y. Gogotsi, *Electrochem. Commun.*, 2012, **16**, 61–64.
141 Y. Xie, M. Naguib, V. N. Mochalin, M. W. Barsoum, Y. Gogotsi, X. Yu, K.-W. Nam, X.-Q. Yang, A. I. Kolesnikov and P. R. C. Kent, *J. Am. Chem. Soc.*, 2014, **136**, 6385–6394.
142 J. Come, M. Naguib, P. Rozier, M. Barsoum, Y. Gogotsi, P.-L. Taberna, M. Morcrette and P. Simon, *J. Electrochem. Soc.*, 2012, **159**, A1368.
143 S. Kajiyama, L. Szabova, K. Sodeyama, H. Iinuma, R. Morita, K. Gotoh, Y. Tateyama, M. Okubo and A. Yamada, *ACS Nano*, 2016, **10**, 3334–3341.
144 N. Shabana, A. M. Arjun, K. Nubla, M. Ankitha and P. A. Rasheed, *Int. J. Hydrogen Energy*, 2023, **48**, 7698–7707.
145 A. J. Borah, V. Natu, A. Biswas and A. Srivastava, *Oxford Open Mater. Sci.*, 2025, **5**, itae017.

146 A. Iqbal, T. Hassan, S. M. Naqvi, Y. Gogotsi and C. M. Koo, *Nat. Rev. Electr. Eng.*, 2024, **1**, 180–198.
147 C. Ma, M. G. Ma, C. Si, X. X. Ji and P. Wan, *Adv. Funct. Mater.*, 2021, **31**, 2009524.
148 M. Han, X. Yin, K. Hantanasirisakul, X. Li, A. Iqbal, C. B. Hatter, B. Anasori, C. M. Koo, T. Torita, Y. Soda, L. Zhang, L. Cheng and Y. Gogotsi, *Adv. Opt. Mater.*, 2019, **7**, 1900267.
149 P. Sambyal, A. Iqbal, J. Hong, H. Kim, M.-K. Kim, S. M. Hong, M. Han, Y. Gogotsi and C. M. Koo, *ACS Appl. Mater. Interfaces*, 2019, **11**, 38046–38054.
150 Y. Liu, A. Thakur, B. Anasori, S. Mohammadi and Ka-band, EMI Shielding Effectiveness of Ti3C2Tx MXene, *Conference Published in: 2023 IEEE/MTT-S International Microwave Symposium - IMS 2023*, 2023, DOI: 10.1109/IMS37964.2023.10187928.
151 T. Yun, H. Kim, A. Iqbal, Y. S. Cho, G. S. Lee, M.-K. Kim, S. J. Kim, D. Kim, Y. Gogotsi, S. O. Kim and C. M. Koo, *Adv. Mater.*, 2020, **32**, 1906769.
152 A. S. M. Mannafi, K. Habib, T. Asrafi and S. A. Ali, *Results Eng.*, 2025, **27**, 106335.
153 Z. Kandemir, E. Torun, F. Paleari, C. Yelgel and C. Sevik, *Phys. Rev. Mater.*, 2022, **6**, 026001.
154 A. Esrafili, M. Ghambarian, M. Yousefi and S. Hosseini, *Nanotechnol. Rev.*, 2022, **11**, 2565–2574.
155 Y. Ning, X. Zeng, J. Huang, Z. Y. Shen, Y. Gao and R. Che, *Adv. Funct. Mater.*, 2025, **35**, 2414838.
156 X. Zhang, X. Wang, Z. Lei, L. Wang, M. Tian, S. Zhu, H. Xiao, X. Tang and L. Qu, *ACS Appl. Mater. Interfaces*, 2020, **12**, 14459–14467.
157 T. Li, L. Chen, X. Yang, X. Chen, Z. Zhang, T. Zhao, X. Li and J. Zhang, *J. Mater. Chem. C*, 2019, **7**, 1022–1027.
158 Q. W. Wang, H. B. Zhang, J. Liu, S. Zhao, X. Xie, L. Liu, R. Yang, N. Koratkar and Z. Z. Yu, *Adv. Funct. Mater.*, 2019, **29**, 1806819.
159 Y. Liu, Y. Wang, N. Wu, M. Han, W. Liu, J. Liu and Z. Zeng, *Nano-Micro Lett.*, 2023, **15**, 240.
160 Y. Wei, P. Zhang, R. A. Soomro, Q. Zhu and B. Xu, *Adv. Mater.*, 2021, **33**, 2103148.
161 I. Mohammed, J. Mohammed and A. Srivastava, *Phys. B*, 2023, **668**, 415240.
162 I. Ali, M. Faraz Ud Din and Z.-G. Gu, *Molecules*, 2022, **27**, 4925.
163 Y. Ma, L. Sun, H. Zhang, S. Wei, X. Li, J. Yin and B. Shi, *Colloids Surf., A*, 2025, **720**, 137091.
164 B. Zhou, Z. Zhang, Y. Li, G. Han, Y. Feng, B. Wang, D. Zhang, J. Ma and C. Liu, *ACS Appl. Mater. Interfaces*, 2020, **12**, 4895–4905.
165 Y. Han, K. Ruan and J. Gu, *Nano Res.*, 2022, **15**, 4747–4755.
166 A. Uddin, R. Khatoon, D. Estevez, M. Salem, A. Ali, S. Attique, J. Lu and F. X. Qin, *Mater. Today Commun.*, 2022, **31**, 103858.
167 A. M. Abubakar, K. Yan, J. Huang and K. Demirelli, *Polymer-Plastics Technology and Materials*, 2025, 1–32.
168 V. Kedambaimoole, K. Harsh, K. Rajanna, P. Sen, M. M. Nayak and S. Kumar, *Mater. Adv.*, 2022, **3**, 3784–3808.
169 K. Qian, Q. Zhou, H. Wu, J. Fang, M. Miao, Y. Yang, S. Cao, L. Shi and X. Feng, *Compos. Appl. Sci. Manuf.*, 2021, **141**, 106229.
170 L.-Q. Zhang, S.-G. Yang, L. Li, B. Yang, H.-D. Huang, D.-X. Yan, G.-J. Zhong, L. Xu and Z.-M. Li, *ACS Appl. Mater. Interfaces*, 2018, **10**, 40156–40167.
171 K. U. Rahman, E. P. Ferreira-Neto, G. U. Rahman, R. Parveen, A. S. Monteiro, G. Rahman, Q. Van Le, R. R. Domeneguetti, S. J. L. Ribeiro and S. Ullah, *J. Environ. Chem. Eng.*, 2021, **9**, 104708.
172 N. Wu, Z. Zeng, N. Kummer, D. Han, R. Zenobi and G. Nyström, *Small Methods*, 2021, **5**, 2100889.
173 W.-J. Zhang, S. Li, V. Vijayan, J. S. Lee, S. S. Park, X. Cui, I. Chung, J. Lee, S.-k. Ahn and J. R. Kim, *Nanomaterials*, 2022, **12**, 4392.
174 Y. Huang, Z. Long, J. Zou, L. Luo, X. Zhou, H. Liu, W. He, K. Shen and J. Wu, *IEEE Trans. Nanotechnol.*, 2022, **21**, 399–405.
175 H. Chen, Y. Wang, X. Chen, Z. Wang, Y. Wu, Q. Dai, W. Zhao, T. Wei, Q. Yang and B. Huang, *Molecules*, 2024, **29**, 2902.
176 G. Liu, J. Zou, Q. Tang, X. Yang, Y. Zhang, Q. Zhang, W. Huang, P. Chen, J. Shao and X. Dong, *ACS Appl. Mater. Interfaces*, 2017, **9**, 40077–40086.
177 H. Lv, Z. Bai, Y. Li, L. Zhao, Y. Bai and F. Feng, *Mater. Chem. Front.*, 2025, **9**, 3323–3331.
178 L. Zhou, H. Zheng, Z. Liu, S. Wang, Z. Liu, F. Chen, H. Zhang, J. Kong, F. Zhou and Q. Zhang, *ACS Nano*, 2021, **15**, 2468–2480.
179 H. Lin, X. Wang, L. Yu, Y. Chen and J. Shi, *Nano Lett.*, 2017, **17**, 384–391.
180 B. Lu, S. Hu, D. Wu, C. Wu, Z. Zhu, L. Hu and J. Zhang, *J. Mater. Chem. B*, 2022, 1226–1235.
181 P. Deng, Z. Ling, F. Fang, J. Ruan, C. Yang, R. Hu, J. Zhou and P. Xiong, *Int. J. Nanomed.*, 2025, 13317–13332.
182 M. Zhang, L. Mei, L. Zhang, X. Wang, X. Liao, X. Qiao and C. Hong, *Bioelectrochemistry*, 2021, **142**, 107943.
183 M. Dehnoei, M. Hosseini, E. Ahmadi-Sangachin and M. Mousavizadegan, *Microchem. J.*, 2024, **204**, 110964.
184 X. Zhu, X. Pang, Y. Zhang and S. Yao, *J. Mater. Chem. B*, 2019, **7**, 7729–7735.
185 P. K. Kalambate, N. S. Gadhari, X. Li, Z. Rao, S. T. Navale, Y. Shen, V. R. Patil and Y. Huang, *TrAC, Trends Anal. Chem.*, 2019, **120**, 115643.
186 S. Hroncekova, T. Bertok, M. Hires, E. Jane, L. Lorencova, A. Vikartovska, A. Tanvir, P. Kasak and J. Tkac, *Processes*, 2020, **8**, 580.
187 H. Zhang, Z. Wang, Q. Zhang, F. Wang and Y. Liu, *Biosens. Bioelectron.*, 2019, **124–125**, 184–190.
188 M. A. Wagner, P. Trickey, Z.-w. Chen, F. S. Mathews and M. S. Jorns, *Biochemistry*, 2000, **39**, 8813–8824.
189 R. B. Rakhi, P. Nayak, C. Xia and H. N. Alshareef, *Sci. Rep.*, 2016, **6**, 36422.
190 T. T. Nguyen, H. Wang, G. Sun, J. Kong and X. Zhang, *Microchim. Acta*, 2024, **191**, 472.
191 J. Sengupta and C. M. Hussain, *Biosensors*, 2025, **15**, 127.

192 L. Guo, Y. Zhao, Q. Huang, J. Huang, Y. Tao, J. Chen, H.-Y. Li and H. Liu, *Microsyst. Nanoeng.*, 2024, **10**, 65.
193 L. Wang, Y. Han, H. Wang, Y. Han, J. Liu, G. Lu and H. Yu, *J. Semicond.*, 2021, **42**, 092601.
194 R. Ramar, S. Kandasamy and H. Ju, *Environ. Sci.: Nano*, 2025, 4796–4842.
195 E. A. Mayerberger, R. M. Street, R. M. McDaniel, M. W. Barsoum and C. L. Schauer, *RSC Adv.*, 2018, **8**, 35386–35394.
196 K. Rasool, K. A. Mahmoud, D. J. Johnson, M. Helal, G. R. Berdiyorov and Y. Gogotsi, *Sci. Rep.*, 2017, **7**, 1598.
197 H. Lin, S. Gao, C. Dai, Y. Chen and J. Shi, *J. Am. Chem. Soc.*, 2017, **139**, 16235–16247.
198 W. Feng, R. Wang, Y. Zhou, L. Ding, X. Gao, B. Zhou, P. Hu and Y. Chen, *Adv. Funct. Mater.*, 2019, **29**, 1901942.
199 X. Han, J. Huang, H. Lin, Z. Wang, P. Li and Y. Chen, *Adv. Healthcare Mater.*, 2018, **7**, 1701394.
200 Z. Liu, H. Lin, M. Zhao, C. Dai, S. Zhang, W. Peng and Y. Chen, *Theranostics*, 2018, **8**, 1648–1664.
201 K. Chen, Y. Chen, Q. Deng, S.-H. Jeong, T.-S. Jang, S. Du, H.-E. Kim, Q. Huang and C.-M. Han, *Mater. Lett.*, 2018, **229**, 114–117.
202 G. P. Awasthi, B. Maharjan, S. Shrestha, D. P. Bhattarai, D. Yoon, C. H. Park and C. S. Kim, *Colloids Surf. Physicochem. Eng. Aspects*, 2020, **586**, 124282.
203 C. Xing, S. Chen, X. Liang, Q. Liu, M. Qu, Q. Zou, J. Li, H. Tan, L. Liu, D. Fan and H. Zhang, *ACS Appl. Mater. Interfaces*, 2018, **10**, 27631–27643.
204 E. A. Al-Harthi, M. K. M. Ali, M. Imran, A. I. Aljameel, A. Ansari, S. Ahmed, S. M. Shinde and M. Arif, *J. Mater. Sci.*, 2026, 1–34.
205 Y. Wang, Y. Zhu, H. Liu, H. Fan, P. Ma, X. Zhang, J. Yang, C. Lu, H. Xue and J. Chen, *J. Chem. Phys.*, 2026, **164**(4), 044707.
206 B. Yang, B. Liu, J. Chen, Y. Ding, Y. Sun, Y. Tang and X. Yan, *Chem. Eng. J.*, 2022, **429**, 132392.
207 B. Yang, B. Liu, Y. Zhu, Y. Ding, J. Yang, P. Ma, X. Zhang and J. Chen, *Scr. Mater.*, 2024, **242**, 115925.
208 J. Xu, R. S. Longchamps, X. Wang, B. Hu, X. Li, S. Wang, L. Li, Y. Gu, X. Cao and N. Yuan, *Adv. Funct. Mater.*, 2024, **34**, 2408892.
209 N. S. Rejinold and J.-H. Choy, *Int. J. Nanomed.*, 2026, 559240.
210 D. Yan, H. Jiang, Y. Liang, B. Zhou and S. Zang, *J. Energy Storage*, 2023, **69**, 107976.
211 J. Shi, B. Jiang, Z. Liu, C. Li, F. Yan, X. Liu, H. Li and D. Dong, *Ceram. Int.*, 2021, **47**, 18540–18549.
212 O. A. Akinwumi, K. O. Olumurewa, A. T. Famojuro and O. O. Akinwunmi, *ECS Meet. Abstr.*, 2025, 3590.
213 G. Wesley, E. Swetlech, C. Velasco, A. Williams, K. Larsen, S. Antony Jose and P. L. Menezes, *Processes*, 2026, **14**, 957.
214 B. Cao, B. Liu, Z. Xi, Y. Cheng, X. Xu, P. Jing, R. Cheng, S.-P. Feng and J. Zhang, *ACS Appl. Mater. Interfaces*, 2022, **14**, 47517–47528.
215 R. A. Soomro, P. Zhang, B. Fan, Y. Wei and B. Xu, *Nano-Micro Lett.*, 2023, **15**, 108.
216 S. Kumar, N. Kumari, T. Singh and Y. Seo, *J. Mater. Chem. C*, 2024, **12**, 8243–8281.
217 I. J. Echols, J. Yun, H. Cao, R. M. Thakur, A. Sarmah, Z. Tan, R. Littleton, M. Radovic, M. J. Green and J. L. Lutkenhaus, *Chem. Mater.*, 2022, **34**, 4884–4895.
218 A. Iqbal, J. Hong, T. Y. Ko and C. M. Koo, *Nano Converg.*, 2021, **8**, 9.
219 H. Lu, J. Wang, H. Li, W. Zhou, Q. Yuan and S. Liu, *Mater. Chem. Front.*, 2023, **7**, 4372–4399.